THE UNIVERSITY OF CHICAGO

# SODIUM CURRENT DIVERSITY AND SPIKE TIMING IN VESTIBULAR GANGLION NEURONS

A DISSERTATION SUBMITTED TO

THE FACULTY OF THE DIVISION OF THE BIOLOGICAL SCIENCES

AND THE PRITZKER SCHOOL OF MEDICINE

IN CANDIDACY FOR THE DEGREE OF

DOCTOR OF PHILOSOPHY

COMMITTEE ON NEUROBIOLOGY

BY

SELINA BAEZA-LOYA

CHICAGO, ILLINOIS

AUGUST 2022

**Table of Contents**

**List of Abbreviations**

4,9-ah-TTX – 4,9-anhydro-tetrodotoxin

AHP – afterhyperpolarization

AP(s) – action potential(s)

ATX-II – *Anemonia viridis* toxin 2

$Ca_V$ – voltage-gated calcium

CV – coefficient of variation

$g_H$ - hyperpolarization-activated cyclic-nucleotide-gated conductance

$g_{KH}$ – high-voltage-activated potassium conductance

$g_{KLV}$ – low-voltage-activated potassium conductance

$g_{leak}$ – linear leak conductance

$g_{Na}$ – voltage-gated sodium conductance

$g_{NaP}$ – persistent sodium conductance

$g_{NaR}$ – resurgent sodium conductance

$g_{NaT}$ – transient sodium conductance

HCN – hyperpolarization-activated cyclic nucleotide-gated

I-$K_V$ – voltage-gated potassium current

$I\text{-}K_H$ or $I_{KH}$ – high-voltage-activated potassium current

$I\text{-}K_{LV}$ or $I_{KLV}$ – low-voltage-activated potassium current

$I\text{-}Na_V$ or $I_{NaV}$ – voltage-gated sodium current

$I\text{-}Na_VP$ – voltage-gated persistent sodium current

$I\text{-}Na_VR$ – voltage-gated resurgent sodium current

$I\text{-}Na_VT$ – voltage-gated transient sodium current

ISI(s) – interspike interval(s)

$K_{LV}$ – low-voltage-activated potassium

MVN – medial vestibular nucleus

$Na_V$ $G_{max}$ – maximum $Na_V$ conductance density

$Na_V$ – voltage-gated sodium

P – postnatal day

PPP – phase plane plot

Pseudo-EPSCs – pseudo-excitatory postsynaptic currents

$R_{in}$ – input resistance

TTX – tetrodotoxin

$V_{AP}$ – spike height

VGN(s) – vestibular ganglion neuron(s)

$V_{rest}$ – resting membrane potential

**List of Figures**

**List of Tables**

**Acknowledgments**

To me, it seems like a miracle that I have come so far in my academic career. To have made so many right decisions and have had so many good opportunities seems too serendipitous to be true. What are the odds that a small girl from a tiny cattle town in the middle of the Arizona desert could accomplish something so momentous as a PhD in Neurobiology from the University of Chicago? That girl, who spent most of her childhood hiding from the world in the depths of a book, overcame the obstacles of language and socioeconomic status to become many firsts: first generation American, first to go to college, first to go to graduate school, first to be a doctor (of philosophy). She is Latina, bilingual, anxious and brave. And the only reason she made it this far is because of the people around her.

It takes a village to support a person through school. For me, it took a *rancho.* The feeling coursing through me is pure and unadulterated gratitude, to myself, to my family, my friends, my coworkers, to all the folks who supported me throughout the years:

First, my parents, Idalia Loya Garcia and Ubaldo Baeza Reyes, who made it very clear from the beginning that I was destined for great things. They supported all the extracurriculars, encouraged the love of reading and learning, and when the time came, let me go to pursue my dreams. They worked hard to understand the educational system with which they had no experience and held my hand the whole way through, even when I didn't know they were there. *Gracias ama y apa.*

My sister, Jennifer A Baeza Loya, my best friend, who always answers the phone. The ultimate wing-woman, the hype woman you wish you had, the one to shakes sense into me when I most need it. Thanks for always being there for me, especially when I need you the most.

Andrew G Eckart, my other half, who has a true love for learning and teaching. Thank you always inspiring me to be better scientist, thinker, orator, arguer, learner, explorer. Thanks for refusing to let me settle for anything less than the best.

The role models and teachers I've had over the years. Dr. Ruth Anne Eatock, of Chicago IL, who showed me how to be a scientist. Dr. Ramiro Salas, of Houston TX, my first PI, who gave me chance to learn and talked to me about science in Spanish. Ms. Theresa Chatman, of Houston TX, who was the first to tell me to get a PhD when I was a freshman at Rice University. I didn't even know what a PhD was when I got to college, and the four years I worked with Theresa at the Office of Graduate and Postdoctoral Studies were deeply influential. She showed me how powerful a PhD could be and what an impact I, as woman of color, could make with one. Mr. Chris Yetman, of Oro Valley AZ, my high school AP Calculus teacher, who helped me apply to college, taught me how to use a fax machine, and explained what the FAFSA is.

My friends, coworkers, and lab mates at Rice and at UChicago, who sympathize, commiserate, support, distract, help, and were along with me every step of the way.

And finally, to the sweet little town of Oracle, Arizona. *Mi rancho*. The place I call home. The place where my mom gets stopped at the post office by an old acquaintance to ask after me – "And Selina? How is she?" – even though I've been gone for ten years. When I visit, I run into old teachers and classmates from the Oracle Public School District, old neighbors who tell me my face hasn't changed at all. My family, aunts, uncles, and cousins, who always welcome me home no matter how far I wander.

**Abstract**

The vestibular inner ear transmits head-motion information to the brain via two populations of primary vestibular ganglion neurons (VGNs) which differ in the regularity of action potential (AP) timing (regular and irregular) and represent rate and temporal encoding, respectively (Jamali et al., 2016). Understanding the impact of diverse ionic currents on spike timing regularity is crucial to understanding how different sensory coding strategies arise. Although voltage-gated sodium ($Na_V$) currents drive the rising phase of APs, their contributions to AP waveform and spike timing regularity in VGNs are not fully understood. $Na_V$ currents through a given α subunit can have different modes: they can be transient (inactivating), persistent (noninactivating), and/or resurgent (following relief from inactivation block).

Here we consider how these $Na_V$ current modes influence AP firing in isolated VGNs, which respond to current injections with sustained and transient firing patterns. These correspond to regular and irregular spiking, respectively. Whole-cell recordings from mouse VGNs revealed that while all had large transient $Na_V$ currents that were blocked by 1 μM tetrodotoxin (TTX), some also had persistent current, and a subset had resurgent current.

A blocker of $Na_V1.6$ channels (4,9-anhydro-tetrodotoxin, 4,9-ah-TTX) partially blocked transient and eliminated persistent and resurgent currents, indicating that a substantial portion of each flow through $Na_V1.6$ channels. In current clamp, 4,9-ah-TTX decreased excitability: increasing current threshold for spiking and increasing time-to-peak in all VGNs, but hyperpolarized resting membrane potential and decreased AP rate in sustained (regular) VGNs and not transient (irregular) VGNs. A sodium channel agonist (*Anemonia viridis* toxin 2, ATX-II) had the opposite effect of increasing the amplitude of persistent and transient currents. This resulted in

increased excitability as measured by decreased current threshold for spiking and increased AP rate and spiking regularity.

We did not detect a clear relationship between $Na_V$ conductance and firing patterns due to unexpected variability in $Na_V$ conductance in VGN. We determined that sustained-A firing VGNs (which respond to current injections with tonic spike trains) have higher amplitude APs and faster rates of depolarization relative to transient VGNs (which fire a single spike at stimulus onset). AP amplitude and rate of depolarization each positively correlated with maximum $Na_V$ conductance. Using the action potential clamp technique, we observed that sustained VGNs have less $Na_V$ current during the depolarization phase of the AP, due to their increased excitability relative to transient VGNs and possible differences in underlying channel kinetics. $Na_V1.6$ currents make up the majority of that depolarizing current, the most of which flows before the peak depolarization.

However, it is difficult to experimentally distinguish the effects of these currents on spiking because we lack methods to isolate current modes. We therefore modified a computational conductance-based model of VGN (Hight and Kalluri, 2016; Ventura and Kalluri, 2019) by adjusting and adding expressions for transient, persistent, and resurgent $Na_V$ components (Wu et al., 2005; Venugopal et al., 2019) with properties based on our data. Adding persistent and resurgent current components had a negligible effect on firing by the model transient (irregular) VGN. For the model sustained (regular) VGN, adding persistent and resurgent currents decreased spike latency (delay relative to current step or pseudo-excitatory postsynaptic current onset), reduced refractory periods, and increased spike rate. Increasing transient sodium current had the effect of increasing spike height, rate of depolarization, and spike rate in all model VGNs. When examining the impact on regularity using pseudo-synaptic input, we observed that increasing

transient current increased spiking regularity independently of increased spike rate in all model VGNs, while persistent and resurgent currents did not enhance spiking regularity.

In summary, transient sodium current increases excitability and spike timing regularity by counterbalancing inexcitability driven by increased low voltage-activated potassium conductance (Ventura and Kalluri, 2019). Resurgent and persistent current facilitate excitability by increasing availability of $Na_V$ channels in regularly firing VGNs, but do not impact regularity.

## Chapter 1 – Introduction

### *The mammalian vestibular ear*

The peripheral vestibular organs sense head acceleration through space and tilt with respect to gravity. Signals carrying information about linear and rotational head motions are integrated into ocular, autonomic, and postural reflexes necessary for maintaining posture and orientation and a stable visual world. Mechanosensitive vestibular hair cells encode and convey head motion information. They are innervated by the terminals of primary vestibular afferents, hereby called vestibular ganglion neurons (VGNs). The cell bodies of VGNs reside outside the otic capsule in

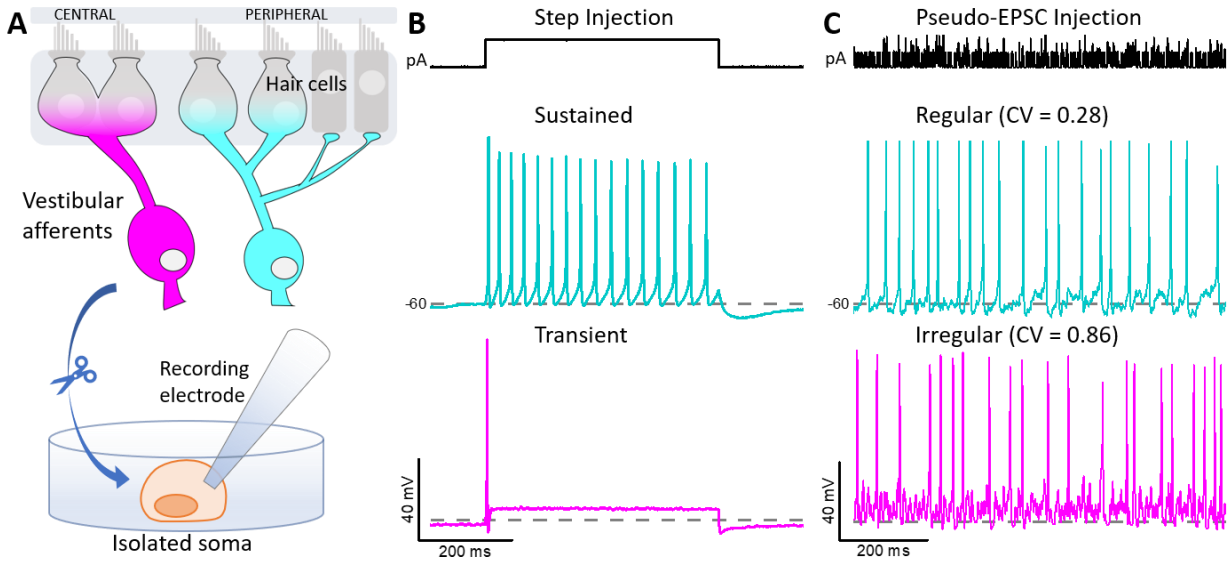


*Figure 1.1 Vestibular afferent neurons differ in their spiking activity.*

**A:** Top panel: Vestibular hair cells synapse onto primary vestibular afferents. The number of synaptic connections differs between zones (central vs. peripheral) of the sensory epithelia. Bottom panel: Vestibular ganglion neurons can be dissected and isolated to assess currents and spiking behaviors via electrophysiology. **B**: Isolated VGNs frequently do not fire spontaneously and must therefore be stimulated with injected current. VGNs can fire with either a sustained (middle panel) or transient pattern (bottom panel) in response to a current step. **C**: When stimulated with simulated synaptic input (pseudo-EPSCs), the same sustained VGN fires at regular intervals, whereas the transient VGN fire at irregular intervals, corresponding to vestibular afferent behavior seen in vivo.

the vestibular ganglion (also known as Scarpa's ganglion), which is comprised of superior and inferior compartments. VGNs are bipolar neurons that carry information from vestibular hairs to vestibular nuclei in the brainstem, cerebellum, and spinal cord.

VGNs can be categorized according to their spiking behaviors, which correlates strongly with morphology and ion channel physiology (Fig 1.1A and Table 1). In vitro, in the absence of synaptic input, VGNs exhibit a spectrum of different firing patterns evoked by current steps, ranging from sustained (tonic) to transient (phasic) patterns (Fig 1.1B). In vivo, VGNs can either have regular or irregular spike timing in response to synaptic input (Goldberg, 2000) (Fig 1.1C), which directly corresponds sustained and transient firing seen in vitro, respectively (Kalluri et al., 2010). Thus, VGNs are described as either regular/sustained VGNs and irregular/transient VGNs. Differences in spike timing, regular or irregular, are hypothesized to be a likely mechanism for rate and temporal encoding strategies (Jamali et al., 2016).

***Spike timing regularity is strongly correlated with sensory encoding strategy***

Regular and irregular VGNs differ in their in vivo response dynamics (i.e., responses in time and frequency domains), as shown by recordings from vestibular afferents in intact animals during head motion stimuli (see Goldberg 2000 for a review). To briefly summarize seventy years of work, irregular afferents are fast adapting and the gain (i.e., sensitivity) of their response increases with frequency, shown by larger responses to high-frequency head motions. Regular afferents are slower adapting and have lower sensitivity to fast head motions. Goldberg postulated that regular afferents could convey more information via their high discharge rate and low variation in firing rate. In contrast, irregular afferents have enhanced sensitivity and high intrinsic variability, both of which impact spike rate fluctuations independently of noisy input and

improving information transmission (Goldberg 2000). The recent application of information theory and statistics to vestibular afferent spike trains, discussed below, has supported this idea.

Jamali and colleagues (2016) showed how regular afferents use rate encoding and irregular afferents use precise spike timing. When examining changes in firing rate (i.e., the use of rate encoding), regular VGNs had higher mutual information metrics relative to irregular afferents. However, when examined within the context of temporal encoding (i.e., precise spike timing), irregular VGNs outperformed regular afferents. Irregular afferents displayed greater variance in their firing rate and were highly nonlinear in their responses. They showed distinctive spiking patterns to repeated trials of the same stimulus, with distinct and reproducible patterns of spikes. Then, using a leaky integrate-and-fire (LIF) computational model of vestibular afferents to examine encoding, they varied sensitivity (likelihood of spiking) and variability (stochasticity) parameters in a model neuron. Model neurons with high levels of sensitivity and low variability increased information transmission via firing rate, like regular afferents. Neurons with high variability showed more precise spike timing performance, like irregular afferents. These in vivo and computational data strongly suggest that systematic differences in intrinsic variability can serve distinct forms of sensory information. Thus, spike timing regularity underlays two parallel sensory encoding strategies used to convey different aspects of head acceleration. How do differences in spike timing regularity arise?

***Ion channels in vestibular afferent neurons***

In general, spike timing regularity strongly depends on expression of voltage-gated ion channels (Bean 2007). VGNs have been shown to have a vast repertoire of channels and evidence

*Table 1 – Properties of regular and irregular VGNs*

| ***Regular VGNs*** | ***Irregular VGNs*** |
|---|---|
| Large dendritic arbor, slow conduction, peripheral zones *(Goldberg 2000; Eatock et al., 2008; Eatock & Songer, 2011)* | Small dendritic arbor, faster conduction, central zones *(Goldberg 2000; Eatock et al., 2008; Eatock & Songer, 2011)* |
| Fewer low voltage-activated potassium channels *(Eatock et al., 2008; Eatock & Songer, 2011)* | More low voltage-activated potassium channels (KCNQ ($K_V7$) and $K_V1$) *(Eatock et al., 2008; Eatock & Songer, 2011)* |
| Slower adapting, lower gain to head motions *(Eatock & Songer, 2011)* | Faster adapting (high-pass filter), more gain *(Eatock et al., 2008; Eatock & Songer, 2011)* |
| Rate encoding *(Goldberg 2000; Sadeghi et al., 2007; Eatock & Songer, 2011)* | Temporal encoding *(Eatock & Songer, 2011; Jamali et al., 2016)* |
| More input encoded at lower (<0.01-several Hz) frequencies *(Sadeghi, et al., 2007; Eatock & Songer, 2011; Jamali et al., 2016)* | Greater encoding precision at higher (>5-10 Hz) frequencies *(Jamali et al., 2016)* |

suggests that ion channel complements differ according to the epithelial zone innervated (Songer & Eatock 2013; Meredith et al., 2015). Various voltage-gated calcium ($Ca_V$) channels (Desmadryl et al. 1997; Chambard et al., 1999), hyperpolarization- activated cyclic nucleotide–gated (HCN) channels (Chabbert et al., 2001b; Ventura and Kalluri, 2019), and calcium-gated and voltage-gated potassium ($K_V$) channels (Chabbert et al., 2001a; Limon et al., 2005; Iwasaki et al., 2008; Kalluri et al., 2010) have all been identified in VGNs.

Low voltage-activated potassium ($K_{LV}$) channels from the $K_V1$ and $K_V7$ families have been implicated in irregular spike timing through their tendency to reduce excitability. For example, Kalluri et al. (2010) showed that the large $K_{LV}$ current (I-$K_{LV}$) in transient neurons hyperpolarizes their resting membrane potential ($V_{rest}$) and decreases input resistance ($R_{in}$), which allows a large spike at stimulus onset but decreases the likelihood for a continued response as I-$K_{LV}$ hinders subsequent spiking. Kalluri and colleagues also blocked I-$K_{LV}$ with a combination of channel blockers (α-dendrotoxin and linopirdine) and demonstrated both an increase in regularity and a decrease in spiking threshold in transient VGNs. More recently, I-$K_{LV}$ has been shown to increase with development in both transient and sustained VGNs, likely driving changes in firing patterns

as VGNs become more phasic after the first month of development (Ventura and Kalluri, 2019). Thus, regularity likely decreases globally as VGNs mature.

Using available electrophysiological data, Hight and Kalluri (2016) developed a conductance-based model of VGN firing to assess the relationship between biophysical characterizations of ionic currents and spike timing. In short, for a transient (irregular) VGN to be produced, the model must have a high level of low voltage-activated potassium conductance ($g_{KLV}$) and moderate levels of voltage-gated sodium ($Na_V$) conductance ($g_{Na}$) as its parameters. In contrast, a fully sustained (regular) model VGN must necessarily be produced by low $g_{KLV}$ and high $g_{Na}$. This model not only reinforced the pivotal role of I-$K_{LV}$ in driving transient/irregular spiking, but also suggested that differences in $Na_V$ conductances may be necessary for spiking regularity. However, $Na_V$ currents and their role in VGN spike timing regularity had not been studied in detail.

***Sodium current diversity in vestibular ganglion neurons***

$Na_V$ currents (I-$Na_V$) are responsible for driving the rising phase of most neuronal action potentials and the availability of channels limits firing rates (Bean 2007; Carter and Bean, 2009). Their role in mediating spike timing differences has been overlooked in rodent VGNs because early reports described homogeneous currents of similar time course, voltage sensitivity, and tetrodotoxin (TTX) sensitivity; specifically, sodium currents in VGNs were all fast-inactivating and TTX-sensitive (Chabbert et al., 1997; Risner & Holt, 2006).

However, there are several mechanisms for I-$Na_V$ diversity that may be present in VGNs. Different $Na_V$ alpha subunits can carry current of different voltage dependencies and TTX sensitivities. Work from our lab showed, using RT-PCR, the expression of all $Na_V$ pore-forming

(α) subunits ($Na_V1.1$-1.9) and auxiliary (β) subunits ($Na_V\beta$1-4) in rat vestibular ganglia (Liu et al., 2016). Whole cell recordings from immature, acutely dissociated cell bodies revealed at least four different transient $Na_V$ currents in acutely excised VGN: 2 TTX-sensitive currents, 1 TTX-insensitive current, and 1 TTX-resistant current (Liu et al., 2016). Although $Na_VT$ currents are responsible for generating spikes, the relative impact of TTX-sensitive, -insensitive and -resistant currents is not well understood.

Another mechanism of I-$Na_V$ diversity results from the channel configuration that produces current flow: to produce a transient ($Na_VT$) current, most $Na_V$ channels strongly inactivate within milliseconds after depolarization by way of the inactivation gate. In some cases, a small fraction does not inactivate even in seconds, creating persistent sodium currents (I-$Na_VP$). $Na_VP$ currents have a more negative activation range than their transient counterparts and therefore contribute to repetitive firing by enhancing $Na_V$ channel availability near resting potential and so reducing refractory periods (Crill 1996; Raman & Bean, 1997).

In some cases, $Na_V$ channels opened by depolarization are rapidly blocked by an intracellular molecule, preventing inactivation; upon repolarization, the channels rapidly unblock and carry resurgent currents (I-$Na_VR$) until they deactivate (reviewed in Lewis & Raman, 2014). I-$Na_VP$ and I-$Na_VR$ through TTX-sensitive $Na_V1.6$ channels have been reported in the calyceal terminals that VGN make on type I hair cells (Meredith and Rennie, 2020) and in vestibular nucleus neurons (Gittis and du Lac. 2008, Gittis et al., 2010). They could contribute to spiking regularity by increasing $Na_V$ channel availability after each spike. Given these properties, we hypothesize that $Na_VP$ and $Na_VR$ currents enhance excitability and increase regularity in vestibular ganglion neurons.

In vivo, vestibular afferent neurons have background firing rates of 100 spikes/s in primates and can reach maximal spiking of 400 spikes per second (Goldberg and Fernandez 1971a, Goldberg 2000). The regularly firing neurons are known to have low current thresholds and highly regular spiking. Since several previous studies suggest that persistent and resurgent sodium currents contribute to regular and rapid firing (Lewis and Raman, 2014), we speculated whether these currents are a factor in spike regularity differences in VGNs.

The aim of the current study is to understand the role of diverse $Na_V$ currents modes, such as transient, persistent, and resurgent currents, in firing patterns, AP waveform, and spike timing regularity of mouse VGNs. We hypothesize that given their noninactivating properties, persistent and resurgent $Na_V$ currents will enhance spiking excitability and spiking regularity. We also hypothesize that transient $Na_V$ currents will be larger in more excitable VGNs (i.e., sustained firing), will drive differences in AP waveform between firing patterns, and will also enhance excitability and regularity.

As our results will show, many postnatal VGNs express $Na_VP$ current, and some express $Na_VR$ sodium current. Their block, and a partial block of $Na_VT$, reduced spiking excitability but not regularity. Their enhancement via increased both excitability and regularity. However, it is difficult to disentangle the effects of I-$Na_VT$, I-$Na_VP$ and I-$Na_VR$ in vitro due to the shared channel identity. We used computational modeling to probe how AP waveforms, neural firing patterns, and spiking regularity are affected by expression of these different $Na_V$ currents. Simulations suggest that $Na_VR$ and $Na_VP$ play roles in increasing excitability in sustained-firing VGNs by reducing refractory periods but have no effect on regularity. Increasing $Na_VT$ current, however, increases both excitability and regularity.

## Chapter 2 – Vestibular ganglion neurons have multiple $Na_V$ channels and current modes

### *Abstract*

Although voltage-gated sodium ($Na_V$) currents have long been overlooked in vestibular afferents, recent work has shown diverse presentations of voltage-gated channels and currents. Here we examine the voltage-dependence and kinetics of transient ($Na_VT$) currents in cultured mouse vestibular ganglion neurons (VGNs) in voltage clamp under restricted experimental conditions. Using special voltage protocols, persistent ($Na_VP$) and resurgent ($Na_VR$) currents are observed in a subset of VGNs. These were determined to be carried by $Na_V1.6$ channels by a specific blocker and have a negative voltage dependence relative to $Na_VT$ currents. $Na_VT$ and $Na_VP$ currents were enhanced by an $Na_V$ channel agonist. Depending on the expression on $Na_VR$ current, VGNs present with differences in $Na_V$ voltage-dependence. Double pulse stimulation experiments indicated that $Na_VP$ and $Na_VR$ currents may aid in relief from channel inactivation. In all, VGNs show diversity in their $Na_V$ currents, voltage-dependence, and kinetics that may impact firing behaviors.

### *Introduction*

Vestibular afferents are remarkable in that they are classified according to their spike timing regularity and are known as either regular or irregular. Differing in their firing rates, regular afferents can fire up to 400 Hz in vivo and irregular afferents fire at similar or lower rates (reviewed in Goldberg 2000). Voltage-gated sodium currents (I-$Na_V$) are responsible for the depolarizing phase of the action potential and channel availability is a limiting factor in firing rates (Bean 2007). While role of I-$Na_V$ in VGN spike timing regularity has historically overlooked due to reports of homogeneity in voltage dependence and tetrodotoxin (TTX) sensitivity (Chabbert et al., 1997;

Risner and Holt, 2006), more recent data has indicated greater diversity in I-$Na_V$ channels and current expression.

Diversity in I-$Na_V$ may arise from expression of different channel subunits and/or current flowing from different channel configurations. Evidence from acutely excised superior compartment of the vestibular ganglion revealed RNA expression of multiple $Na_V$ pore forming (α) subunits and all accessory (β) subunit (Liu et al., 2016). RT-PCR data from postnatal day (P) 1 and 21 showed expression of all known α and β subunits, except for the skeletal muscle subunit $Na_V1.4$. Recordings from acutely dissociated VGN showed expression of currents through TTX-insensitive $Na_V1.5$, TTX-resistant $Na_V1.8$, and various complements of TTX-sensitive channels ($Na_V1.1$, 1.2, 1.3, 1.6, 1.7) that express transient $Na_V$ currents (I-$Na_V$T) (Liu et al., 2016). $Na_V1.5$ current has also been described in gerbil afferent endings (Meredith and Rennie, 2018). Given this diversity in channel expression, we hypothesize that our isolated and cultured mouse VGN will express multiple $Na_V$T currents.

Recent work has also showed I-$Na_V$ diversity in vestibular afferent endings in the form of different current types, such as the persistent (I-$Na_V$P) and resurgent currents (I-$Na_V$R) (Meredith and Rennie, 2020). I-$Na_V$P typically activates at subthreshold membrane potentials when few other channels are activated and membrane resistance is high, effectively amplifying small depolarizing inputs (see Crill 1996 for a review). I-$Na_V$R is a type of current that results from a set of channels are the blocked from inactivation and are active during the repolarization phase of an action potential (see Lewis and Raman 2014 for a review). We hypothesize that $Na_V$R and $Na_V$P currents are expressed in isolated vestibular ganglion neurons, are carried through $Na_V1.6$ channels, and aid in increasing channel availability.

Here, we first characterize the voltage dependence and kinetics of activation and inactivation of I-$Na_V$T in isolated and cultured mouse VGN under restricted experimental conditions. We test for I-$Na_V$P and I-$Na_V$R currents and their channel identities using pharmacological agents. We then describe differences in voltage-dependence between cells with various I-$Na_V$ complements. Using a $Na_V$ channel agonist, we assess the impact of increased noninactivating $Na_V$ current on responses to voltage steps, ramps, and AP waveforms. Last, we test $Na_V$ current inactivation in VGNs with multiple $Na_V$ current components.

***Results***

*All VGNs had TTX-sensitive transient sodium current*

We recorded sodium currents in dissociated and cultured VGNs: with small or no neurites, these cells allow excellent space clamp. Voltage-clamp recordings were made at room temperature (~24°C) in "$Cs^+$-based" internal and external solutions that minimized $K^+$ and $Ca^{2+}$ currents. We also reduced $Na^+$ (by 50%) in the external solution to reduce the large $Na_V$ currents and thereby lower series resistance ($R_S$) voltage errors. Figure 2.1 shows exemplar transient $Na_V$ currents recorded from VGNs in response to a voltage step protocol. As previously reported (Chabbert et

*Table 2 – Passive and active electrophysiological properties of I-$Na_V$ in VGN.*

Mean ± SEM and sample size are presented.

| **Experiment (n = )** | **Age** days | **Cm** pF | **Rs** MΩ | **$R_{in}$** MΩ | **Act $V_{1/2}$** | **Act S** | **Inact $V_{1/2}$** | **Inact S** | **G density** nS/pF | **Gmax** nS |
|---|---|---|---|---|---|---|---|---|---|---|
| Reduced $[Na]^{ext}$ | 12.3 ±0.63 (85) | 17.8 ±0.74 (78) | 6.2 ±0.77 (78) | | -35.8 ±0.75 (75) | 5.7 ±0.19 (76) | -68.1 ±1.07 (73) | 8.4 ±0.52 (74) | 3.8 ±0.29 (74) | 63.8 ±5.7 (74) |
| Standard $[Na]^{ext}$ | 8.4 ±0.65 (61) | 15.9 ±0.76 (57) | 8.4 ±1.49 (57) | 627.8 ±95.5 (42) | -38.9 ±1.21 (29) | 3.2 ±0.28 (29) | -59.1 ±1.65 (23) | 4.4 ±0.79 (23) | 6.8 ±0.72 (29) | 112.9 ±10.2 (48) |
| *Liu et al., 2016 (rat VGN)* | *P1-11 (12)* | *15.2 ±0.4* | *4-14* | | *-36.5 ±1.6 (11)* | *5.7 ±0.4 (11)* | *-76.3 ±0.2 (12)* | *7.6 ±0.1 (12)* | *8.7* ±1.0 *(12)* | |

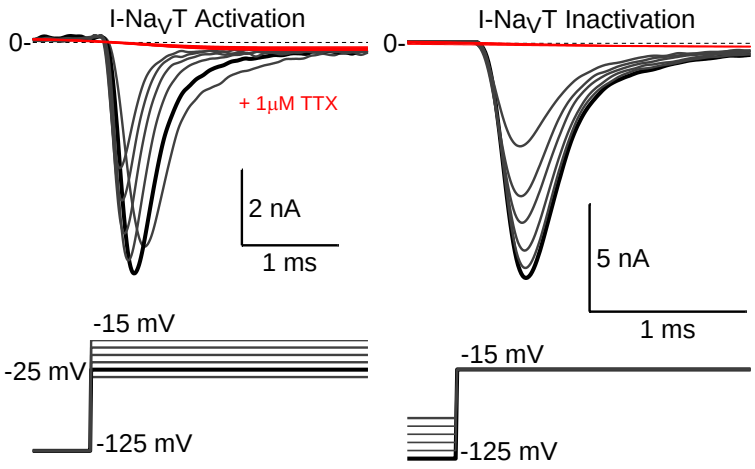


*Figure 2.1 VGNs express NaVT currents.*

Transient sodium currents are evoked by depolarizing steps in 5 mV increments from a prepulse of -125 mV. In all VGN, transient currents were completely blocked by 1 μM TTX.

al., 1997; Risner and Holt, 2006; Liu et al., 2016), depolarizing steps following a hyperpolarizing prepulse revealed fast-inactivating I-NaVT in all VGNs (Fig 2.1). A summary of I-NaVT properties can be found in Table 2; our mouse I-NaVT data are comparable to I-NaV data previously recorded in culture rat VGNs (Liu et al., 2016).

I-NaVT was completely blocked by 1 μM tetrodotoxin (TTX) (Fig 2.1) (n = 78). In recordings from rat VGNs made on the day of dissociation, rather than after culturing, Liu et al.

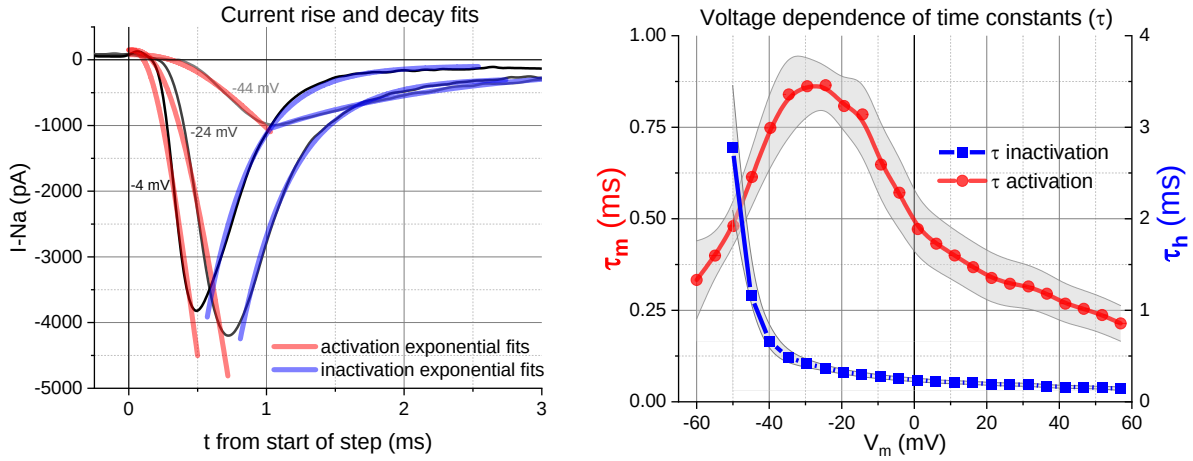


*Figure 2.2 Activation and inactivation time course kinetics of NaVT currents in mature VGNs.*

**A**: Example of exponential fits of current rise and decay at three different voltage steps. Current decay (inactivation) is fit with a single exponential function and current rise (activation) is fit with a cubed exponential. **B**: Voltage dependence of time course of activation and inactivation. Mean ± SEM is shown.

(2016) recorded multiple kinds of I-$Na_V$T with different TTX sensitivities: TTX-insensitive $Na_V$1.5 current ($IC_{50}$ ~300 nM TTX) and TTX-resistant $Na_V$1.8 current (no block at 5 μM TTX), in addition to TTX-sensitive current. As in other studies of overnight-cultured VGNs (Chabbert et al., 1997; Risner and Holt, 2006), we did not detect either TTX-insensitive or -resistant current, even when applying 300 nM TTX to block the larger TTX-sensitive current (n = 5, not shown). With time in culture, VGNs lose their myelin, allowing access to the cell body for recording neurons. We therefore took this approach to study VGNs at more mature stages where myelin coverage is increased, although the results of Liu et al. (2016) suggest that this method affects the expression of some forms of transient current.

To describe the kinetics of I-$Na_V$T, the voltage dependence of activation and inactivation time constants, $\tau_m$ and $\tau_h$, was determined by fitting the rising and falling phases of I-$Na_V$T elicited at different voltage steps, from the origin of the command pulse to the extrapolated current peak for activation and vice versa for inactivation (Fig 2.2A). An example of fits for a P24 VGN at three different voltage steps and the voltage dependence of $\tau_m$ and $\tau_h$ from −60 to +60 mV is shown in Figure 2.2A.

As for the studies done by Costa (1996), the maximum of the bell-shaped curve for $\tau_m$ falls close to the mean half-maximal activation voltage ($V_{1/2}$) value of the activation curves (Fig 2.2B).

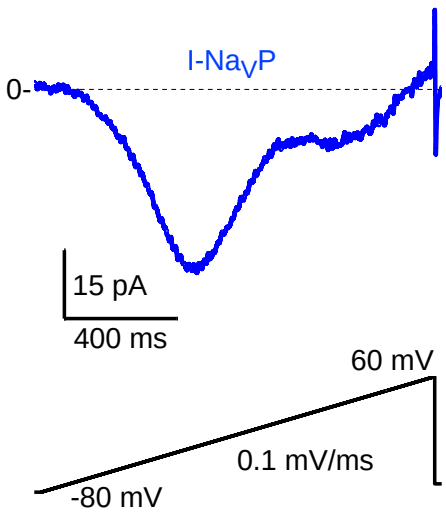


*Figure 2.3 $Na_V$P current in an exemplar VGN.*

Persistent current components were evoked using a slow 0.1 mV/ms voltage ramp from -80 mV to 60 mV and were determined by subtracting control current from that in 1 μ M TTX.

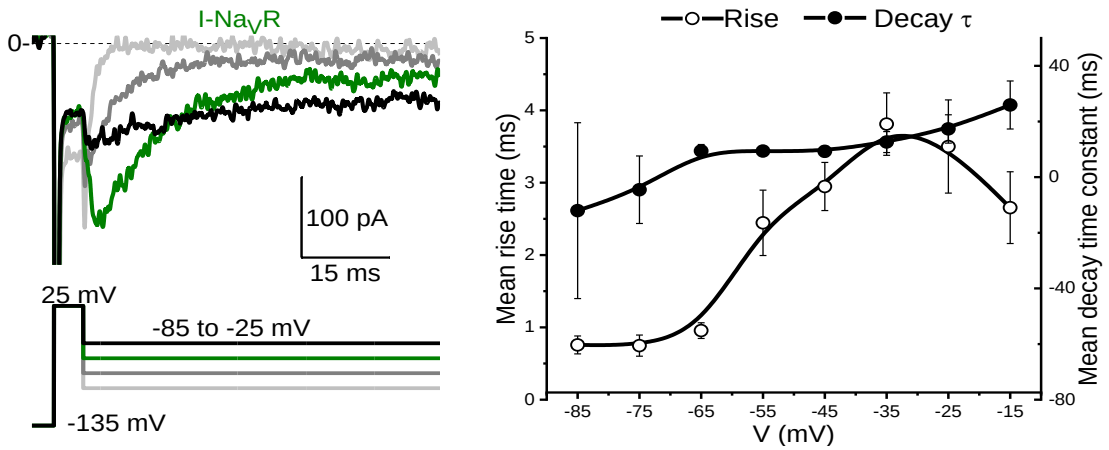


*Figure 2.4 VGNs express $Na_VR$ currents.*

**A:** Resurgent sodium current was evoked by repolarizing steps to -25 to -80 mV after an initial depolarization to 25 mV and determined from a control subtraction after 1 μM TTX. **B**: Rise time (time to peak) and decay time constants for the resurgent sodium currents (n = 6).

*Some VGNs had persistent current, and some had resurgent current*

In this study, we were interested in characterizing the non-inactivating components of sodium current for their potential to influence spiking excitability. To eliminate the inactivating current, we applied a slow voltage ramp from −80 to +60 mV at 0.1 mV/s (Raman and Bean, 1997). To eliminate contributions from leak or other channels, we subtracted the ramp current in 1 μM TTX from the control ramp current. This method often revealed a small inward current activating in the middle of the voltage ramp (Fig 2.3) − a persistent $Na_V$ current ($I\text{-}Na_VP$).

Resurgent current is revealed by delivering a depolarizing step to open $Na_V$ channels, then repolarizing steps to various voltage levels, as illustrated by an example in Figure 2.4. It is thought that a blocking particle enters the channel at the activating voltage, preventing inactivation, and unblocks upon repolarization, yielding resurgent current (I-$Na_V$R), which then inactivates (Lewis and Raman, 2014). We observed I-$Na_V$R in 6 of 78 VGNs (7.6%). Of those 6, 2 were VGNs that had only I-$Na_V$T and I-$Na_V$R; given the small sample size, we pooled the data from these 6 neurons in the following analyses. VGN resurgent currents exhibited typical rise and decay kinetics (Raman and Bean, 1997; Lewis and Raman, 2014), and peak at proximately the same voltage as the total current (Fig 2.4B, Fig 2.5).

Relative to I-$Na_V$T, I-$Na_V$R and I-$Na_V$P reached maximal amplitude at repolarizations to –45 mV and depolarization to −25 mV, respectively (Fig 2.5). Although peak I-$Na_V$R was ~3% and peak I-$Na_V$P was ~1% of peak I-$Na_V$, at subthreshold voltages these small currents make up a significant proportion of the depolarizing $Na_V$ current; for example, at −70 mV, I-$Na_V$R and I-$Na_V$P are 114% (~80 pA) and 15% (~10 pA) of I-$Na_V$T (~70 pA), respectively.

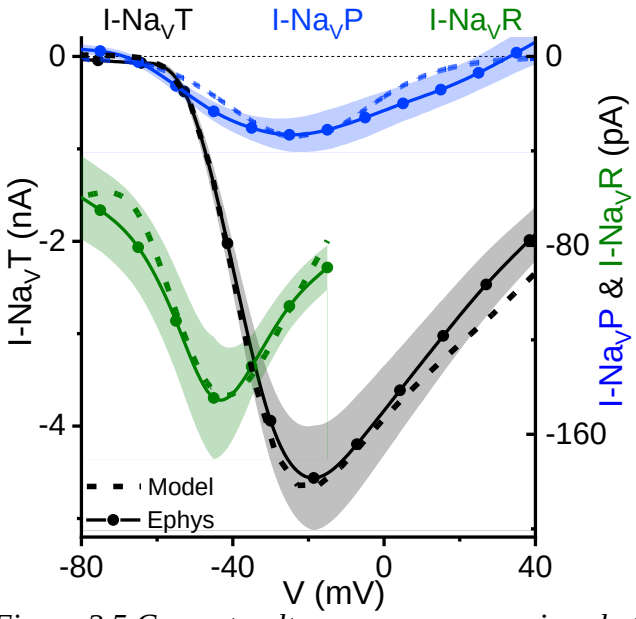


*Figure 2.5 Current-voltage curves comparison between the three current components.*

Persistent and resurgent currents are more negatively activating relative to transient current. Dotted lines indicated IV curves generated by HH model (see Chapter 5 Methods)

*Table 3 – Electrophysiological properties of different I-Na$_V$ combinations*

| I-Na$_V$ (n = ) | Act V$_{1/2}$ | Act S mV | Inact V$_{1/2}$ | Inact S | G density nA/pF | Age Days |
|---|---|---|---|---|---|---|
| I-Na$_V$T | -35.6 ± 1.0 (10) | 6.6 ± 0.3 | -70.1 ± 2.1 | 12.3 ± 1.3 | 2.9 ± 0.3 (31) | 13.7 ± 0.9 (38) |
| I-Na$_V$T+P | -37.7 ± 1.6 (12) | 7.1 ± 0.4 | -66.4 ± 2.3 | 12.8 ± 0.8 | 3.6 ± 0.4 (34) | 11.6 ± 1.0 (34) |
| I-Na$_V$T+P+R | -48.6 ± 5.7 (6) | 6.0 ± 0.4 | -67.5 ± 6.3 | 11.5 ±1.0 | 5.9 ± 0.9 (6) | 17.5 ± 1.3 (6) |

*VGNs with different sodium current components show different voltage dependencies*

To measure how the presence of the persistent and resurgent current components influenced the voltage dependence of the total I-Na$_V$ we fitted activation (G-V) curves with the Boltzmann functions (Eq 1and Eq 2) and compared the fit parameters (Fig 2.6B), which are summarized in Table 3. Activation parameters differed depending on the complement of sodium current components. VGNs with all three components, I-Na$_V$T + P + R, had a significantly more negative average half-maximal activation voltage relative to cells with both I-Na$_V$T + P (p = 0.02)

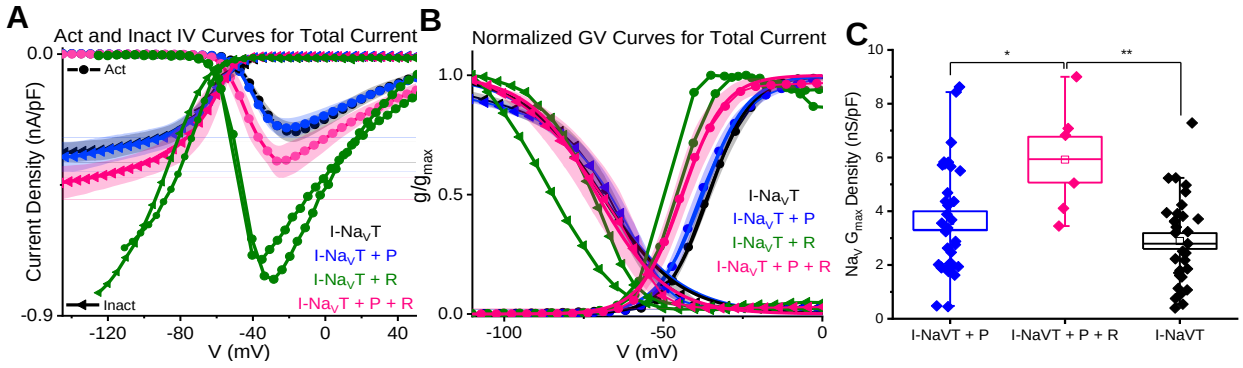


*Figure 2.6 VGNs with Na$_V$T, Na$_V$P, and Na$_V$R current components differ in their voltage dependence and kinetics.*

**A**: Current-voltage curves of cells with different current components. **B**: Activation voltage dependence differed in cells with difference combinations of I-Na$_V$ currents. **C:** VGNs with I-Na$_V$T+P+R (pooled I-Na$_V$T+P+R and I-Na$_V$T+R) had larger conductance densities relative to I-Na$_V$T+P (*p = 0.02) and I-Na$_V$T (**p = 0.002). Box indicates SEM and median, open squares indicate the mean, and whiskers mark 5-95 confidence intervals.

or just I-$Na_V$T ($p = 0.008$, one-way ANOVA, Tukey's HSD, Appendix Table 7). Activation voltage dependence of cells with I-$Na_V$T were not different than those with I-$Na_V$T + P ($p = 0.8$). The half-maximal inactivation and inactivation slope were not different between the groups (one-way ANOVA, $p = 0.7$, Appendix Table 8). Additionally, VGNs with I-$Na_V$T + P + R had larger maximum sodium conductance density relative to I-$Na_V$T ($p = 0.002$) and I-$Na_V$T+P ($p = 0.02$) (Fig 2.6C) (Table 3 and Appendix Table 9). This suggests that these cells increased $Na_V$ channel density, increasing the number of channels conceivably available for depolarizing. This, and shifting voltage range into subthreshold voltage may increase excitability and decrease spike threshold and AP latency.

*$Na_V$1.6 channels carried a significant portion of transient, persistent, and resurgent current components in cultured VGNs.*

In neurons with resurgent currents, such as cerebellar Purkinje cells, $Na_V$1.6 channels can carry all three current components (Raman and Bean, 1997). Purkinje neurons in $Na_V$1.6 null mice have reduced $Na_V$T and $Na_V$P current, and almost no $Na_V$R current (Raman and Bean, 1997; Khaliq al., 2003; Grieco and Raman, 2004). Here we test for $Na_V$1.6 contributions to the $Na_V$T, $Na_V$P, and $Na_V$R current components using the highly selective blocker 4,9-anhydro-tetrodotoxin (4,9-ah-TTX) (Rosker et al., 2007).

100 nM of 4,9-ah-TTX blocked the majority of I-Na$_V$T in VGNs (Fig. 2.7A, B). The 4,9-ah-TTX-sensitive ("blocked") current had $V_{1/2}$ values that were not significantly different from control values for activation (one-way ANOVA, Tukey's HSD, p = 0.99) and inactivation (p =

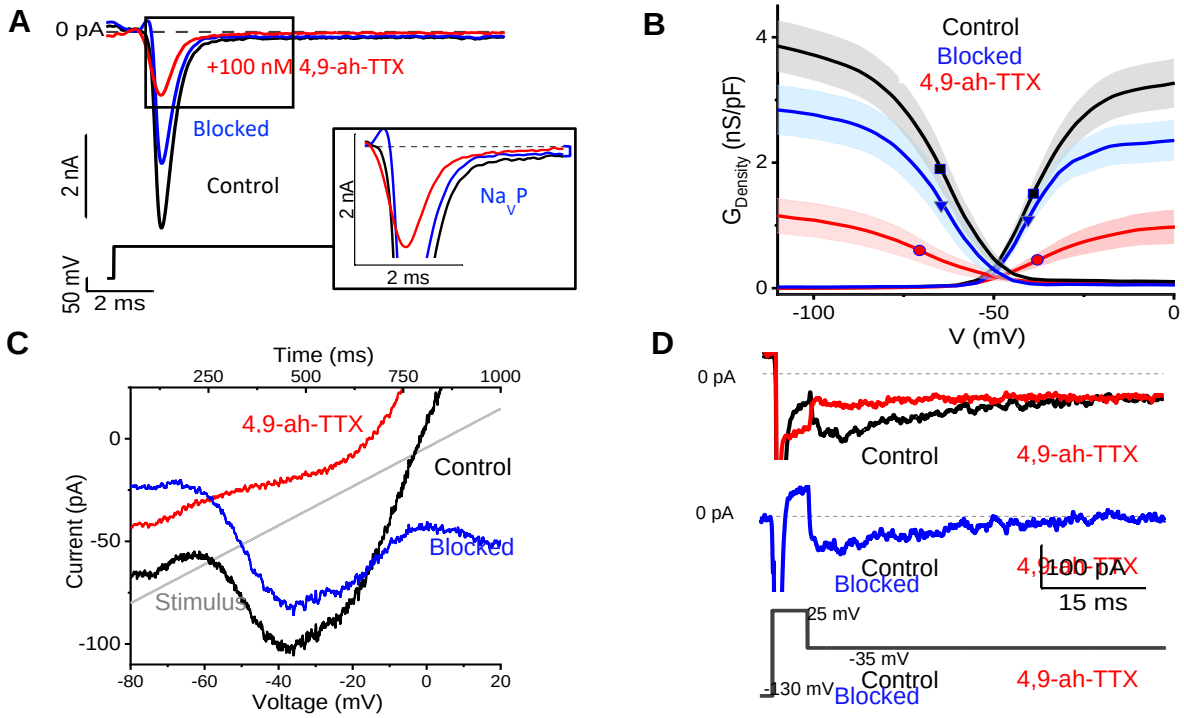


*Figure 2.7 Na$_V$T, Na$_V$P, and Na$_V$R currents are sensitive to 100 nM of Na$_V$1.6 channel blocker 4,9-ah-TTX.*

**A**: Transient current is partially blocked. Inset shows persistent current at end of step is blocked. **B**: Boltzmann fits of conductance curves for transient currents seen in A. Residual current (not sensitive to 4,9-ah-TTX) has more negative voltage dependence relative to sensitive and control transient currents. Symbols indicate corresponding $V_{1/2}$ for activation and inactivation on each curve. **C & D**: When tested, persistent current and resurgent currents are also blocked.

*Table 4 – Properties of 4,9-ah-TTX sensitive and non-sensitive currents.*

| **4,9-ah-TTX** (n = 13) | **Act V1/2** | **Act S** mV | **Inact V1/2** | **Inact S** | **G density** nS/pF |
|---|---|---|---|---|---|
| Control | -38.7 ± 1.6 | 5.7 ± 0.6 | -71.1 ± 3.7 | 10.8 ± 2.3 | 3.1 ± 0.3 |
| Blocked | -38.4 ± 1.8 | 5.4 ± 0.8 | -70.4 ± 3.6 | 10.0 ± 2.2 | 0.3 ± 0.1 |
| Residual | -44.6 ± 3.6 | 12.6 ± 3.9 | -85 ± 3.9 | 21.4 ± 11.2 | 2.7 ± 0.6 |

0.93) (Table 4 and Appendix Tables 10 and 11). This is not surprising, given that the blocked current makes up the majority of the total current. However, the remaining ("residual") current not blocked by 4,9-ah-TTX had a more negative voltage range of inactivation ($p = 0.04$) relative to the control inactivation (Fig 2.7B and Appendix Table 10). $V_{1/2}$ of activation value was not significantly different, ($p = 0.25$) (Table 4 and Appendix Table 10). This suggests at least two types of $Na_VT$ currents.

Persistent and resurgent currents were also blocked by 100 nM 4,9-ah-TTX. Block of I-$Na_VP$ eliminated the non-inactivating current in voltage steps (Fig 2.7A inset) and in the slow voltage ramp (Fig 2.7C) ($n = 11$). Resurgent current was also blocked (Fig 2.7D) ($n = 1$). This all suggests that $Na_V1.6$ carries the majority of I-$Na_V$ in cultured VGNs, including a significant portion of I-$Na_VT$, most of I-$Na_VP$, and possibly I-$Na_VR$.

*Transient and persistent currents were enhanced by $Na_V$ channel agonist ATX-II*

The sea anemone toxin *Anemonia viridis toxin 2* (ATX-II) interacts with the gating of $Na_V$ channels, slowing down or preventing inactivation of $Na_V$ currents. As a result, ATX-II has been

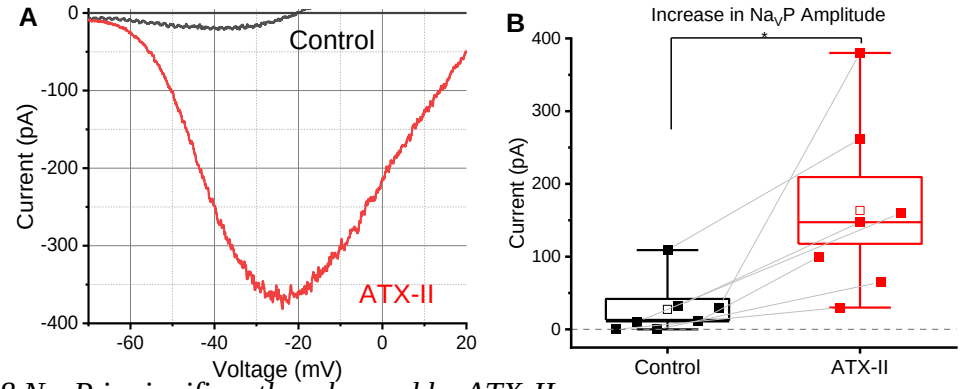


*Figure 2.8 $Na_VP$ is significantly enhanced by ATX-II.*

**A**: Voltage-current relationship of persistent current in a P7 VGN, before (grey) and after (red) the application of 100 nM ATX-II. **B**: Box plots of $Na_VP$ current amplitudes before (Control) and after (ATX-II) application of ATX-II. Box indicates SEM and median, open squares indicate the mean, and whiskers mark 5-95 confidence intervals.

shown to enhance $Na_VP$ currents in vestibular afferent calyces (Meredith and Rennie, 2020), and increase $Na_VR$ and $Na_VP$ currents in spiral ganglion neurons (Browne et al., 2017) and dorsal root ganglion (Klinger et al., 2012). We tested the impact of ATX-II on I-$Na_VT$, I-$Na_VP$ and I-$Na_VR$ in our VGN cell bodies.

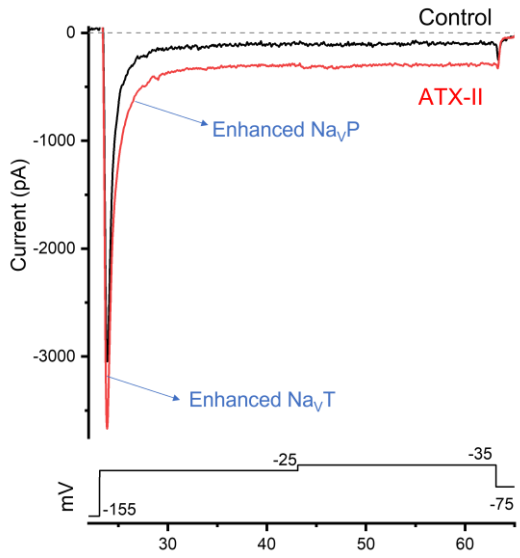


*Figure 2.9 $Na_VT$ amplitude is sometimes increased by ATX-II.*

An example of enhanced $Na_VT$ and $Na_VP$ current after application of 100 nM ATX-II (red trace) (top panel) has elicited by depolarizing voltage steps (bottom panel)

Application of 100 nM ATX-II during voltage clamp showed an increase in maximum amplitude of I-$Na_VT$ in some VGN (Fig 2.8). This was seen in 3 out of 7 VGN tested. In all VGN, the inactivation of I-$Na_VT$ was slowed, resulting in an increased amplitude of I-$Na_VP$ at the end of the depolarizing step during step protocols and especially during slow voltage ramp protocols (Fig 2.9A). On average, I-$Na_VP$ was increased from 27.4 ± 13.4 pA to 163.5 ± 41. pA (n = 7, paired t-test; p = 0.01; Hedges' g = 0.93) (Fig 2.9B and Appendix Table 12). The voltage dependence of I-$Na_VT$ and I-$Na_VP$ was not altered by ATX-II (Appendix Table 12).

*Resurgent currents are affected by VGN culturing*

I-$Na_VP$ was detected in 62 of 100 (62%) VGNs across all ages whereas I-$Na_VR$ was only detected in 6 of 81 VGNs tested, all older than P10 (Fig 2.8A). Expression of I-$Na_VR$ may be not as limited as this data suggests. In gerbil vestibular afferent endings (Meredith and Rennie, 2020), I-$Na_VR$ was detected in immature cells (P6) and increased in size with maturation, coinciding with

increased expression of $Na_V1.6$. We speculated whether the culturing process was influencing expression of I-$Na_V$R in mouse VGNs. In a small sample of uncultured (acute) VGNs (n = 14), we observed I-$Na_V$P in 10 VGNs, and I-$Na_V$R in 4 (Fig 2.8B). Current density and voltage-dependence of I-$Na_V$R both cultured and acute VGNs were comparable to records from Meredith and Rennie, 2020. Due to the increased myelination and attachment of glial cells to mature VGN cell bodies, we were unable to record acutely from VGNs older than P14.

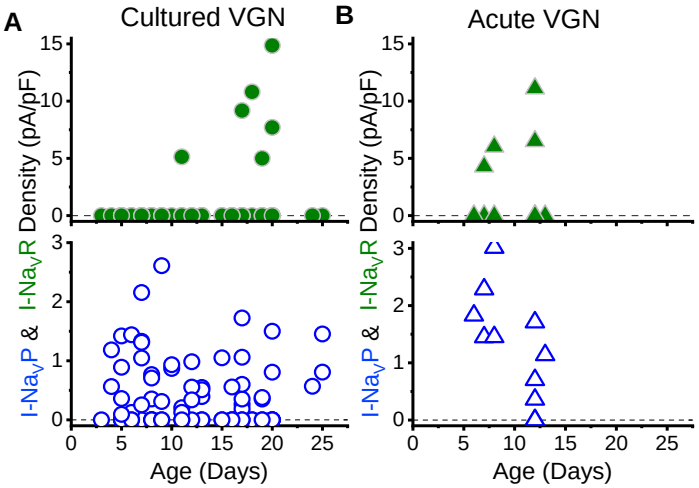


*Figure 2.10 Expression of $Na_V$P and $Na_V$R currents may be affected by culturing.*

**A:** In cultured VGN: out of 81 VGN tested, 6 had I-$Na_V$R, all mice older than P10. Out of 100 VGN tested (P3-25, average age P13), 62 had I-$Na_V$P. **B:** In acute (uncultured VGN): Out of 14, 4 had I-$Na_V$R and 10 had I-$Na_V$P.

*$Na_V$P and $Na_V$R currents were correlated with faster recovery from inactivation*

Since I-$Na_V$P and I-$Na_V$R are slow to or do not inactivate, we hypothesized that these current components would promote $Na_V$ channel availability and recovery from depolarization, which are important for rapid AP firing. To assess this, time courses of recovery of I-$Na_V$ were compared following a 5-ms step to 0 mV to drive channels into an inactivated state (Fig 2.9A). Recovery from inactivation was assessed by measuring the current availability 2 ms to 50 ms after the initial depolarizing step (Fig 2.9A).

Figure 2.9B shows how the peak I-$Na_V$ recovered faster for cells with I-$Na_V$T + P (and I-$Na_V$R, in one case) (blue curve) than for cells with I-$Na_V$T alone. The recoveries in both cases

followed and are fit with a double exponential time course function, with time constants of 1.9 and 14.7 ms (I-$Na_V$T + P condition) and 3.0 ms and 28.5 ms (I-$Na_V$T alone). The difference in recovery as a function of time was significant until 14 ms after the first step, after which >90% of the current had recovered in both cases. These data suggest that persistent currents reduce recovery time and enhance $Na_V$ channel availability during periods of high firing activity, which are physiological.

We speculate that due to their negatively shifted activation ranges and non-inactivating properties, I-$Na_V$P and I-$Na_V$R would impact VGN excitability (spike threshold and firing rates) for small stimuli. In the next chapter, we examine the relationship between I-$Na_V$ and spiking behaviors in current clamp.

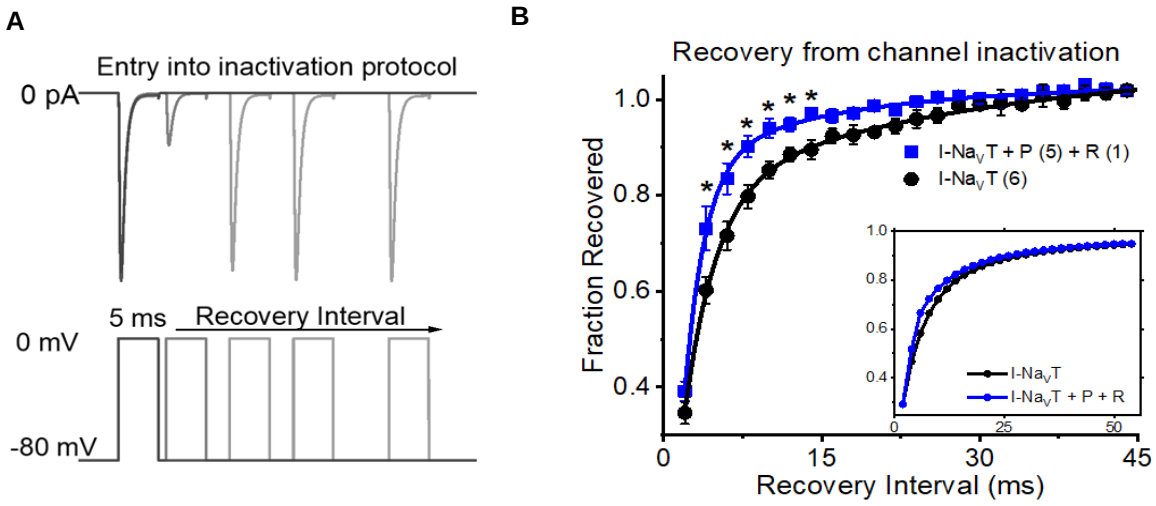


*Figure 2.11 $Na_V$P currents correlate with faster recovery from inactivation.*

**A:** $Na_V$ currents are evoked by two pulses per sweep, with interval incremented 2 ms per sweep. Not all steps shown. **B:** VGN with I-$Na_V$T and I-$Na_V$P (and one with I-$Na_V$R) have faster $Na_V$ current recovery relative to VGN with just I-$Na_V$T (*, $p < 0.05$). Curves are fit with double exponential functions. **Inset:** Results of HH model (Chapter 5) stimulated with same voltage protocol.

***Discussion***

We observed $Na_VT$, $Na_VP$, and $Na_VR$ sodium currents in mouse ganglion neurons, from neonatal ages into maturity. Using an $Na_V1.6$-specific blocker, we found that a significant component of I-$Na_VT$, and most of I-$Na_VP$ and I-$Na_VR$, are carried through $Na_V1.6$ channels. We observed evidence of at least two kinds of $Na_VT$ current with different voltage dependence of activation. We only observed a few examples of I-$Na_VR$ in cultured VGNs. Dissociation may select for a subpopulation of VGNs. Additionally, the culturing process may influence $Na_V$ channel expression and the resulting firing characteristics; for example, Liu et al. (2016) saw $Na_V1.5$ and $Na_V1.8$ currents in acutely dissociated, but not cultured, rat VGNs. VGNs are usually studied in culture, where the overnight culture process reduces myeline and satellite cell coverage of the cell bodies that tend to increase with age (e.g., Chabbert et al., 1997; Risner and Holt, 2006; Kalluri et al., 2010).

Liu et al. (2016) described at least 4 different kinds of I-$Na_VT$ in acutely dissociated rat VGNs. Depending on the expression of TTX-insensitive ($Na_V1.5$) or TTX-resistant ($Na_V1.8$) currents, VGNs expressed TTX-sensitive currents of different voltage-dependencies, indicating that sodium channels are expressed in specific complements (Liu et al., 2016). We also observed that, depending on the expression of I-$Na_VR$, the voltage dependence of the total current varied (Fig 2.6). We noted that blocking the $Na_V1.6$ revealed a smaller non-$Na_V1.6$, TTX-sensitive component that was more negative in activation and inactivation relative to $Na_V1.6$ (Fig 2.7). This residual current may be carried by a subset of $Na_V1.1$, 1.2, 1.3, and/or 1.7 channels.

$Na_V1.6$ channels have been detected in vestibular calyx afferent endings (Lysakowski et al., 2011; Meredith and Rennie, 2018; Meredith and Rennie, 2020). There is also evidence that

suggests developmental upregulation of $Na_V1.6$ currents in sensory neurons with age (Hong et al., 2018; Meredith and Rennie, 2020), with the onset of resurgent $Na_V1.6$ currents after the second postnatal week. In gerbil cristae, I-$Na_V$R and I-$Na_V$P are also upregulated with development; they are detected with greater frequency in mature peripheral zone afferents and are hypothesized to play a role in maintaining regularity in this VGN subpopulation as $K_{LV}$ currents increase (Meredith and Rennie, 2020). Our sample of acutely dissociated VGNs was too limited to determine any developmental onset of $Na_V$R or $Na_V$P currents.

We observed that in mouse VGNs, the presence of I-$Na_V$P and I-$Na_V$R correlated with faster recovery from inactivation. I-$Na_V$R has been described in more than 20 types of neurons that show spontaneous, repetitive, or bursting behaviors (reviewed in Lewis and Raman, 2014). In inner-ear systems, persistent and resurgent sodium currents have been described in auditory (spiral) ganglion neurons (Browne et al, 2017), avian nucleus magnocellularis neurons (Hong et al., 2018), the calyx of Held (Leao et al., 2005) and its postsynaptic target, neurons of the medial nucleus of trapezoid body (Kim et al., 2010), as well as vestibular afferent calyx terminals (Meredith and Rennie, 2020) and medial vestibular nuclei neurons (Gittis and du Lac, 2008), which all show high spontaneous and evoked firing rates.

However, our experimental conditions for revealing I-$Na_V$P and I-$Na_V$R are not conducive to spiking. The elimination of potassium, calcium, etc., ions from the intracellular and extracellular solutions prevents the cell from firing as normal. Therefore, we examined spiking in a different set of experiments.

***Methods***

***Cell preparation:*** Whole-cell currents and voltages were recorded from the cell bodies of VGNs isolated from CD1 mice on P3 to P25. Animals were handled in accordance with the *National Institutes of Health Guide for the Care and Use of Laboratory Animals*, and all procedures were approved by the animal care committee at the University of Chicago. Mice were anesthetized via isoflurane inhalation and decapitated, and temporal bones were dissected in chilled Liebovitz-15 (L-15) medium supplemented with 10 mM HEPES at pH 7.4 with NaOH, ~320 mmol/kg. Chemicals were purchased from ThermoFisher (Waltham, MA) or MilliporeSigma (Burlington, MA).

The otic capsule was exposed, and the superior part of the vestibular ganglion, which innervates the utricle, lateral, and anterior semicircular canals and part of the saccule was dissected out bilaterally. The tissue was placed in L-15 supplemented with 0.12 % collagenase and 0.12% trypsin for 15-20 minutes at 37°C. The ganglion was then dissociated by gentle trituration into bicarbonate-buffered medium and cells were allowed to settle in glass-bottomed culture dishes (MatTek, Ashland, MA) precoated with poly-D-lysine. In most experiments, recordings were made after cells were incubated 10-20 hours in Minimal Essential Medium with Glutamax (MEM, Invitrogen, Carlsbad, CA) supplemented with 10 mM HEPES, 5% fetal bovine serum (FBS), and 1% penicillin in 5% $CO_2$-95% air at 37°C. Overnight incubation removed myelin and satellite cell coverage from cell bodies. Age of cells does not include time in culture: e.g., data from a P17 VGN indicates the pup was 17 days old when tissue was harvested. The number of surviving cells decreased with age. In several "acute" experiments, recordings were made on the same day as dissociation.

***Recording solutions:*** During experiments, cells were bathed in one of two external solutions: in voltage clamp experiments, "Cs+ external" solution contained (in mM): 75 NaCl, 5.4 CsCl, 2.5 $MgCl_2$, 75 TEACl, 5 HEPES, 10 D-Glucose, titrated with CsOH to a pH of 7.4, about ~310 mmol/kg. We minimized K+ currents by substituting $Cs^+$ for $K^+$ and 70 mM tetraethylammonium (TEA, a K channel blocker) for equivalent $Na^+$. Reducing external $Na^+$ reduced total $Na_V$ current amplitude and series resistance voltage errors that interfered with voltage clamp. To minimize $Ca^{2+}$ current, only trace $Ca^{2+}$ was present and $Ca_V$ channels were blocked by $Mg^{2+}$. The internal pipette solution for these voltage clamp experiments contained: 148 CsCl, 0.8 CaCl, 3.5 Na2 creatine phosphate, 3.5 Mg-ATP, 0.1 Li-GTP, 5 EGTA, 5 HEPES, 0.1 Na-cAMP, titrated to a pH of 7.4 with CsOH, ~300 mmol/kg.

***Whole cell recordings:*** Cells were visualized at 600X on an inverted microscope equipped with Nomarski optics (IMT-2; Olympus, Lake Success, NY). We chose round cells with diameters >5 µm (range 8-25 µm). Mean membrane capacitance was 18.3 ± 0.54 (n = 181), similar to mouse VGN data we previously reported in Liu et al. (2016). Neurons were identified by the presence of $Na_V$ currents upon break in.

Signals were delivered, recorded, and amplified with either an Axopatch 200A amplifier, Digidata 1440A digitizer, and pClamp 10 software or a Multiclamp 700B amplifier, Digidata 1440A digitizer, and pClamp 11 software (Axon Instruments, Molecular Devices, Sunnyvale, CA), with low-pass Bessel filtering set at 10 kHz and sampling interval set at 5 µs. Electrodes were pulled from soda glass (King Precision Glass, Claremont, CA) to resistances of 3-4 MΩ in our solutions and wrapped with parafilm to reduce pipette capacitance. All membrane voltages were

corrected offline for a liquid junction potential of 5.2 mV (Cs+ solution), calculated with JPCalc software (Barry 1994) in pClamp 11.

The series resistance ($R_S$) ranged between 3 and 10 MΩ and was compensated by 73 ± 0.66%. Only recordings in which the cell had formed a gigaohm seal and maintained stable membrane potential were used. The holding potential ($V_H$) in voltage-clamp mode was −64 mV (standard solution) and −65 mV (Cs+ solution). Recordings were made at room temperature (23-25°C) because fast $Na_V$ currents are difficult to voltage clamp and characterize at body temperature.

***Pharmacology:*** On the day of experiments, we thawed stock solutions of the $Na_V$ channel blocker TTX (2 mM in distilled water), 4,9-ah-TTX (500 μM in methanol), or $Na_V$ channel agonist ATX-II (100 μM in distilled water) and added aliquots to 5 mL of external solution to concentrations of 1 μM, 100 nM, and 100 nM respectively. ATX-II-containing solution included 1 mg/ml of albumin. The toxin-containing solutions were applied via local perfusion (Perfusion Fast-Step, Warner Instruments, Holliston, MA) delivered with a Bee Hive Controller (BASI, West Lafayette, IN). Control and drug solutions flowed through adjacent delivery tubes and a stepper mechanism selected the tube directed at the patched cell. This system allows for no dead volume. Perfusion of control solution before the drug solution provided additional control for flow effects.

***Analysis***: Analysis was performed in MATLAB (The MathWorks, Natick, MA) and Clampfit (Axon Instruments, Molecular Devices). Figures and statistical analysis were done in Origin Pro 2018 (OriginLab, Northampton, MA). Mean ± SEM are presented. For comparisons between 2 groups, we estimated statistical significance with Student's t-test when variances were equal, with Welch's t-test when variances were not equal, and paired t-tests between two measures

of the same sets of cells. We used an alpha level of 0.05 for all statistical tests. Hedges' g with a bias correction for small sample sizes was used to indicate effect size, the degree of difference between means. In some cases, one-way ANOVAs were applied following a post hoc Tukey's HSD analysis.

The voltage dependence of activation and inactivation was only analyzed if $R_S$ voltage error was < 10 mV at peak current. Activation and inactivation curves of conductance ($g$) vs. voltage ($V$) were generated by plotting peak current ($I$) against step voltage, then dividing the peak current by the driving force ($V - E_{rev}$) to obtain $g$. The resulting curves were generally well fit by the Boltzmann function:

$$g(V) = \frac{g_{max}}{1 + exp^{\frac{V_{act} - V}{s}}} \qquad \textit{Eq 1}$$

where $g_{max}$ is the maximum conductance, $V_{act}$ is the voltage of half-maximal activation, and $s$ is the slope factor. Inactivation curves were generated by plotting the peak current produced by a test pulse (to -30 or -10) against the iterated prepulse voltage and fit by another Boltzmann function:

$$g(V) = \frac{g_{max}}{1 + exp^{\frac{V - V_{inact}}{s}}} \qquad \textit{Eq 2}$$

with $V_{inact}$ equaling voltage of half-maximal inactivation.

The membrane time constant ($\tau_m$) was obtained by fitting the voltage response to a small current step with an exponential function. The time constant of activation ($\tau_m$) was assessed by fitting the rising phase of a sodium current with the equation:

$$I(t) = I_f - I_{peak}\,(1 - e^{-t/\tau_m})^3 \qquad \textit{Eq 3}$$

whereas the time constant of inactivation ($\tau_h$) was assessed by fitting the decaying phase of a sodium current with:

$$I(t) = I_f + I_{peak}\,(e^{-x/\tau_h}) \qquad \textit{Eq 4}$$

## Chapter 3 – $Na_V$ currents influenced VGN spiking excitability and regularity


### *Abstract*

Differences in vestibular ganglion neuron firing patterns likely depend on the expression of different ion channels. Sustained VGNs, as opposed to transient VGNs, are more excitable, have lower current thresholds, and have fewer low voltage-activated potassium channels. Here we examine the relationship between maximum $Na_V$ conductance density and action potential waveform and spiking properties. Larger $Na_V$ conductances correlated with larger spike amplitudes and greater rates of depolarization, but there were no clear differences in net $Na_V$ conductance between firing patterns. Block of $Na_V1.6$ currents decreased spiking excitability in all VGNs and made resting membrane potential more negative in sustained VGNs. Enhancement of non-inactivating current increased spiking excitability and regularity. However, these manipulations were not selective enough to clarify the impact of $Na_VP$ and $Na_VR$ currents on excitability and regularity.


### *Introduction*

Regular and irregular vestibular afferents have several key differences in their spiking properties. Goldberg and colleagues observed differences in response dynamics during *in vivo* stimulation with head motions; irregular afferents proved to be faster adapting and had greater sensitivity (see Goldberg 2000 for a review). These differences do not directly translate to *in vitro* studies of vestibular ganglion, where neurons seldom spike spontaneously. In this preparation, VGNs are categorized according to the firing pattern evoked by depolarizing current injections. Thus, they are labeled as either transient or sustained.

Transient VGNs have low spiking excitability, as shown by higher current thresholds and fewer spikes. Their APs tend to have a smaller afterhyperpolarization (AHP), and they express more low voltage-activated potassium ($K_{LV}$) channels (Iwasaki et al., 2008; Kalluri et al., 2010). Kalluri et al. (2010) showed, in isolated rat VGNs, that the large $K_{LV}$ current (I-$K_{LV}$) in transient neurons hyperpolarizes their resting membrane potential ($V_{rest}$), decreases input resistance ($R_{in}$), and reduces the AHP. Blocking I-$K_{LV}$ with α-dendrotoxin and linopirdine increased regularity and decreased spike threshold in transient VGNs. More recently, I-$K_{LV}$ has been shown to increase with development, likely driving changes in firing patterns as VGNs become more transient-like and irregular in firing after the first month of development (Ventura and Kalluri, 2019).

Sustained VGN, in contrast, have low current thresholds and a deep AHP, consistent with fewer $K_{LV}$ channels and a less negative resting potential. As previously stated, the role of $Na_V$ currents in spike timing regularity has been long overlooked due to previous reports of homogeneity in voltage dependence and TTX sensitivity in cultured VGN somata (Chabbert et al., 1997; Risner and Holt, 2006). We hypothesize that a large I-$Na_V$ may be necessary for producing the high and sustained firing observed in sustained VGNs. Additionally, I-$Na_V$ may be essential for maintaining sustained firing patterns in the wake of developmentally upregulated I-$K_{LV}$. Recent work (Rennie and Meredith, 2020) showed more I-$Na_V$ current diversity in the form of $Na_VP$ and $Na_VR$ currents, which were observed with greater frequency in mature peripheral afferent endings of regular/sustained VGN. While their impact on VGN firing is yet unknown, I-$Na_VP$ and I-$Na_VR$ are known to enhance high frequency, highly regular firing in other types of sensory neurons (see Lewis and Raman 2014 for a review). Given the voltage-dependence and kinetic properties of

$Na_VP$ and $Na_VR$ currents, we hypothesize that these are more prominent in regular (sustained) VGNs.

While we are unable to record clear examples of I-$Na_VP$ and I-$Na_VR$ under the experimental conditions needed to assess firing patterns in VGNs, we were able to capture I-$Na_VT$ in most neurons and calculate maximum $Na_V$ conductance density ($Na_V$ $G_{Max}$). We observed the relationships between $Na_V$ $G_{Max}$ and various features of the action potential and the firing pattern evoked by either current steps or by recorded trains of EPSCs. With the $Na_V1.6$ selective blocker, we could also test the influence of $Na_V1.6$ currents on spiking in response to current injections and pseudo-EPSC injections.

***Results***

*$Na_V$ conductance correlates with action potential waveform features*

We sought to determine the role that $Na_V$ currents have in different VGN firing patterns. To study spiking behaviors, we recorded from 62 VGNs in current clamp mode in standard solutions (normal potassium, sodium, and calcium concentrations internally and externally) and no channel blockers. In these conditions, I-$Na_V$ can escape voltage clamp as it is very large and fast; nevertheless, we were able to record some information about the current for correlations with the spike waveform and firing pattern. We found correlations between properties of action potential waveforms, firing patterns and maximum sodium conductance, suggesting $Na_V$ currents may influence firing patterns in different ways.

We classified the 62 neurons into four groups based on firing patterns evoked by depolarizing current steps, following the scheme of Ventura and Kalluri (2019) for rat VGNs (Fig 3.1A and Appendix Table 13). Transient neurons fired a single spike at the onset of the current

step independent of its size. Sustained-firing neurons displayed varying degrees of accommodation, ranging from cells that fired long trains of spikes throughout the depolarizing step (sustained-A) to cells that fire shorter trains of spikes (sustained-B), sometimes followed by voltage oscillations (sustained-C). Transient VGNs had a significantly lower current threshold for spiking relative to sustained-A and sustained-B VGNs (Appendix Table 14); there was no significant difference in $V_{rest}$ or $R_{in}$ between firing patterns (Appendix Table 15 and 16), although sustained VGNs on average had higher input resistance relative to transient VGNs (654 ± 143 MΩ vs. 330 ±74 MΩ, p = 0.07, power = 0.43).

We assessed the AP waveform of each firing pattern (Fig 3.1C and Appendix Table 17). Sustained-A APs were significantly taller than transient APs (One-way ANOVA, p = 0.004) (Fig 3.1C and Appendix Table 18). Transient APs also had slower peak rates of depolarization (peak dV/dt) relative to sustained-A and sustained-B APs (p = 0.01, p = 0.03) (Fig 3.1 and Appendix Table 19). Time-to-peak and voltage threshold was not significantly different between firing patterns (Fig 3.1C and D, and Appendix Table 20 and 21).

Additionally, the depth of the afterhyperpolarization ($\Delta V_{AHP}$) was also significantly different between firing pattern groups (Fig 3.1G and Appendix Table 22); sustained-A neurons had a much deeper AHP relative to all other groups. Differences in AHP have previously been attributed to differences in low voltage-activated potassium conductances, which influence resting membrane potential, current threshold, and membrane recovery time (Hight and Kalluri, 2016; Kalluri et al., 2010; Iwasaki et al., 2008), all factors in shaping the AHP. The AHP preserves sodium channel availability by relieving inactivation, shortening the refractory period, and allowing sustained and regular firing at high rates (Gittis et al., 2010).

In these neurons, we recorded I-$Na_V$ in voltage clamp mode. Often, we were not able to clamp the rapid current, or the current was too large and saturated the amplifier (>20 nA). In the cases where we could get a good recording (n = 56), we fit the activation curves with Boltzmann

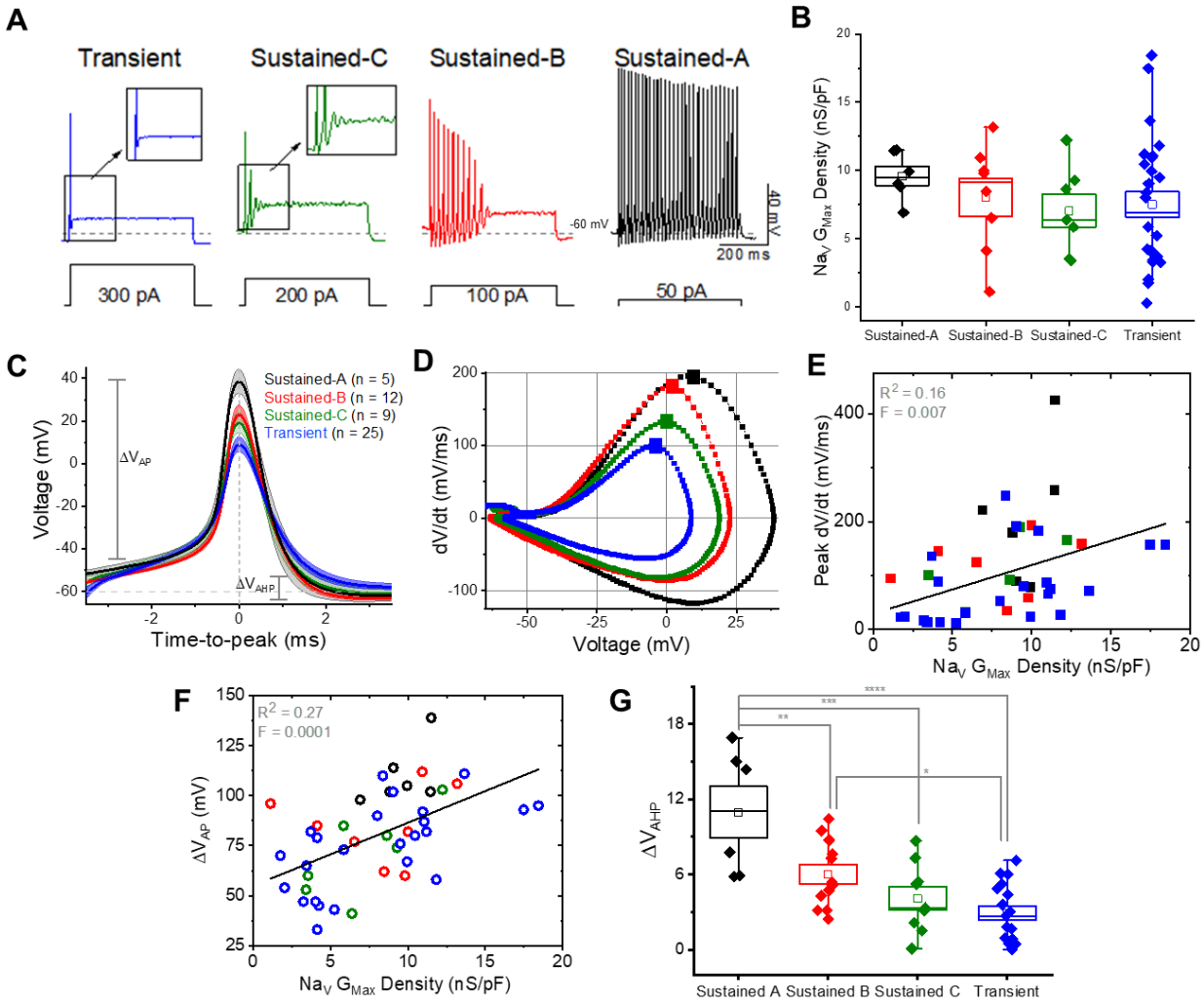


*Figure 3.1 Maximum $Na_V$ conductance density correlates with features of VGN AP waveform.*

**A**: Exemplar firing patterns seen in VGN as evoked by a single long (500 ms) current step of different amplitudes reflecting different current thresholds. **B**: Variation in maximum $Na_V$ conductance with firing pattern is not significant; from Boltzmann fits of activation curves, not shown. Box indicates SEM and median, open squares indicate the mean, and whiskers mark 5-95 confidence intervals. **C**: Average spikes aligned to peak with features such as spike height ($V_{AP}$) and afterhyperpolarization ($V_{AHP}$). **D**: Phase plane plots of APs from C. Squares denote peak dV/dt values. **E & F**: $Na_V$ $G_{Max}$ positively correlated with peak dV/dt and $V_{AP}$. **G:** $V_{AHP}$ varied with firing pattern (****, p = 0.00007; ***, p = 0.0005; **, p = 0.009; *, p = 0.04).

functions to measure maximum $Na_V$ conductance ($Na_V$ $G_{Max}$) (Fig 3.1B). Total $Na_V$ $G_{Max}$ was not significantly different between VGNs of different firing patterns (One-way ANOVA, $p = 0.68$, Appendix Table 23).

$Na_V$ $G_{Max}$ did correlate with some depolarization features of the action potential waveform (Fig 3.1C, D): action potential height ($\Delta V_{AP}$) (Fig 3.1C) and peak dV/dt as shown in the phase plane plot (Fig 3.1D) both positively correlated with $Na_V$ $G_{Max}$ (Fig 3.1E, F). This makes sense because $Na_V$ currents depolarize the cell membrane and drive the rising phase of the AP.

In summary, we measured the total sodium conductance in relation to different VGN firing patterns. $Na_V$ $G_{Max}$ positively correlated with features of the AP waveform such as spike amplitude, AHP, and peak rate of depolarization. Our hypothesis was that sustained-A VGNs would have the greatest amount and transient VGNs would have the smallest amount of $Na_V$ $G_{Max,}$ but instead observed that $Na_V$ $G_{Max}$ is not significantly different between firing patterns.

*Distribution of VGN firing patterns changes with development*

The distribution of firing patterns breaks down as shown vs. age in Figure 3.2: sustained-A (6 of 62, 10%), sustained-B (13, 21%), sustained-C (10, 16%), and transient (33; 53%) (Fig 3.2A). Previous studies have reported developmentally driven changes to the distribution of firing patterns in VGNs (Iwaski et al., 2008; Ventura et al, 2019). Ventura et al. (2019) reported that the proportion of rat VGNs with sustained firing patterns (pooling sustained-A, B, and C) decreases after the first postnatal week; by the third week, nearly 70% of VGNs had transient firing patterns and only 5% had sustained-A patterns. Indeed, in our data, we saw that sustained-A and sustained-C firing neurons were recorded in the first several postnatal days (P3-10), with just 1 outlying sustained-C neuron at P 19 (Fig 3.2A, B). After P10 (P11-25), a sensory developmental benchmark where neonatal mice begin to open their eyes and ears, almost all VGNs had either a sustained-B (38%) or a transient firing pattern (56%) (Fig 3.2B).

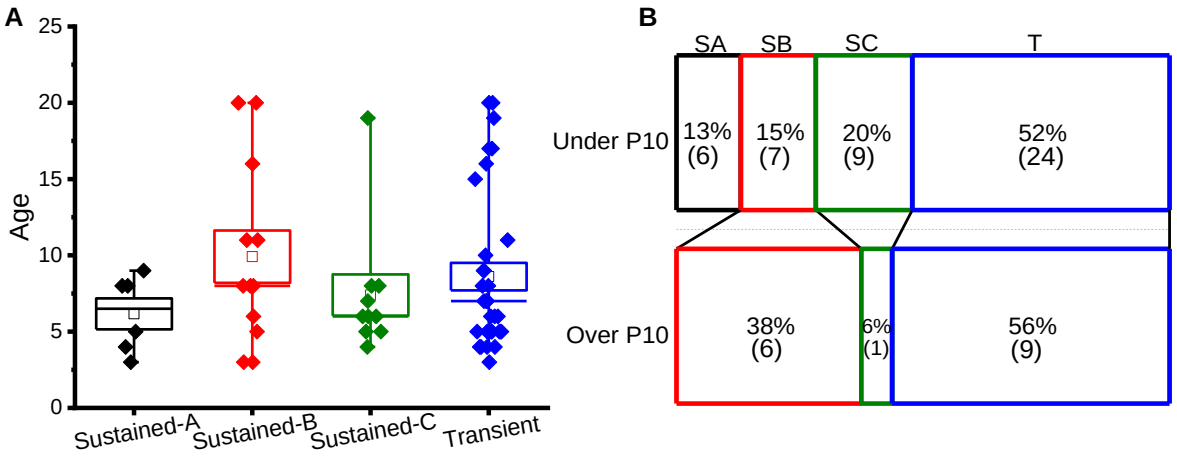


*Figure 3.2 VGN firing pattern distribution changes with development.*

**A:** Ages of VGN with each firing pattern. **B:** Distribution of firing patterns change over development. Most frequent patterns observed in mature are sustained-B and transient (Ventura et al., 2019) While this reflects upregulation of KLV (low voltage-activated K currents) (Kalluri et al., 2010), developmental changes in $Na_V$ currents may also be a factor.

These numbers are comparable to the data Ventura and Kalluri (2019) recorded in their mature rat VGNs. This shift coincides with developmental upregulation of low voltage-activated potassium currents ($I_{LKV}$) that drive irregularity in VGNs (Ventura et al., 2019; Hight and Kalluri, 2016; Kalluri et al., 2010; Iwasaki et al., 2008). We speculate that the developmental onset of $Na_VR$ current balances the acquisition of $K_{LV}$ currents and maintain the spectrum of regularity (Meredith and Rennie, 2020). There was no clear growth of $Na_V$ $G_{max}$ over the course of development and only a slight correlation of $Na_V$ $G_{max}$ with current threshold for spiking (not shown). We suspect that $K_{LV}$ conductances overpower the effects of $Na_V$ conductance such that no matter how much $Na_V$ conductance there is in transient VGNs, the large $K_{LV}$ conductances will still reduce excitability.

*Block of $Na_V1.6$ currents reduces excitability but regularity*

We applied 100 nM 4,9-ah-TTX to probe the role of $Na_V1.6$ currents in the generation of step-evoked firing patterns and pseudo-EPSC evoked AP trains in our dissociated VGNs. In voltage clamp experiments, we observed that 4,9-ah-TTX blocked a significant proportion of $Na_VT$, $Na_VP$, and $Na_VR$ currents (see Chapter 2: NaV1.6 channels carried a significant portion of transient, persistent, and resurgent current components in cultured VGNs.

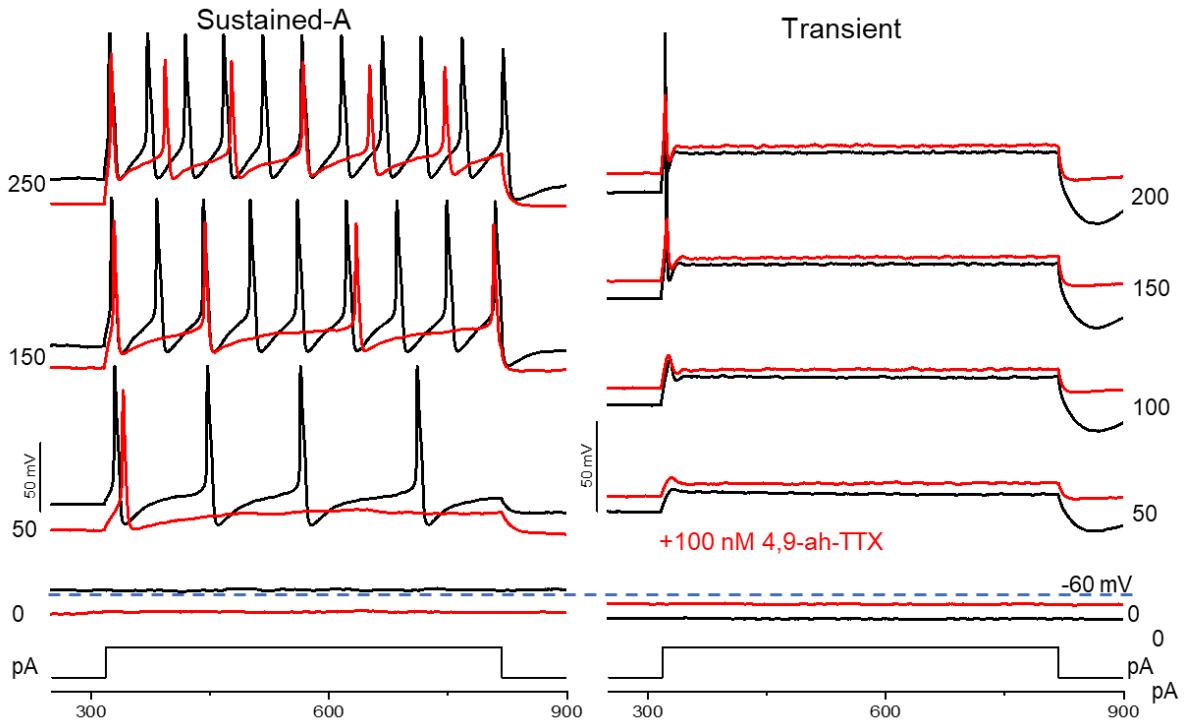


*Figure 3.3 $Na_V1.6$ block decreases VGN firing excitability.*

100 nm 4,9-ah-TTX (red) on reduced excitability relative to control (black) in firing. In sustained-A VGN, reduced number of APs at spiking threshold and throughout the family of current steps, until entered depolarization block at highest magnitude. In transient VGN, current threshold for spiking was increased, and spike amplitude was decreased.

Figure 3.3 shows that, for long current steps, block of $Na_V1.6$ currents altered firing in both sustained and transient type firing neurons. These representative examples illustrate how, in sustained-A VGNs, the $Na_V1.6$ blocker decreased firing at all current sizes. In the transient neuron, the blocker increased threshold current two-fold, decreased spike amplitude for all sizes of steps, and increased first-spike latency for small steps. In general, 4,9-ah-TTX increased long step threshold (paired t-test, n = 12, p = 0.03, Hedges' g = 0.63) from 95.8 ± 14.9 pA to 166.6 ± 25.6 pA. There was no difference in the % I-$Na_VT$ block between transient (n = 8) and sustained (n = 4) VGNs (50.1 ± 11.3% vs 52.0 ± 5.2%) (Welch's t-test, p = 0.94, power = 0.05), and VGNs tend to stay within their firing categories, whether sustained or transient.

Application of 4,9-ah-TTX hyperpolarized the resting membrane potential ($V_{rest}$) (Fig 3.4). $V_{rest}$ became more negative in sustained firing VGN, hyperpolarizing from -57.6 mV to -66.8 mV (paired t-test; p = 0.03, Hedges' g = 0.67) (Fig 3.4A), but did not change significantly in transient VGNs (-59.5 mV to -63.75 mV, p = 0.16, power = 0.27) (Appendix Table 24). These data suggest that 4,9-ah-TTX blocks depolarizing currents that are open at rest (such as I-$Na_V$P), for which there may be either a larger current or a greater depolarizing effect (reflecting higher input resistances) in sustained VGNs.

We aligned the first action potential of the firing patterns evoked by long current steps at the peak to assess changes to the AP waveform (Fig 3.5A and Appendix Table 25). After the application of 4,9-ah-TTX, we observed a decrease in spike height (n = 12, p = 0.01, Hedges' g = 0.49) (Fig 3.5B) and AHP (p = 0.006). There was no difference in spike width. We observed an increase in the time-to-peak: blocking of $Na_V1.6$ currents increased the delay in first spike latency (p = 0.05, Hedges' g = 0.42) (Fig 3.5D). Phase plane plots of the averaged APs further highlighted salient differences (Fig 3.5E), most notably the decrease in peak rate of depolarization (p = 0.03, Hedges' g = 0.41) (Fig 3.5F).

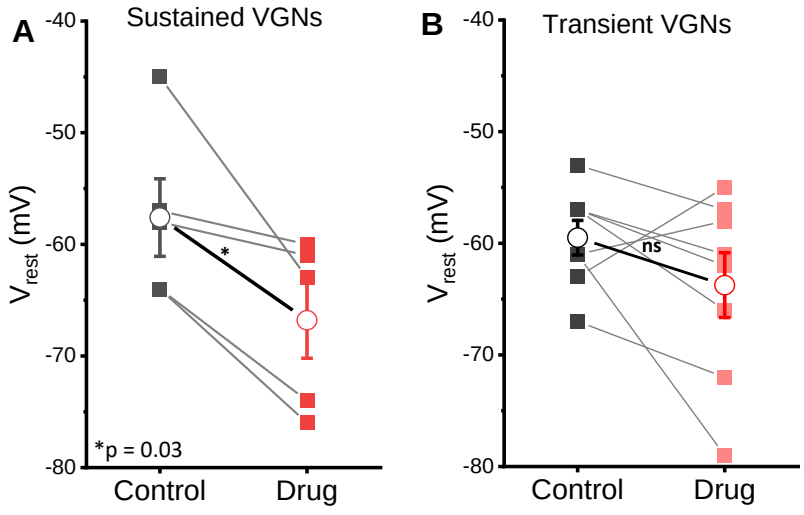


*Figure 3.4 Blocking $Na_V1.6$ currents hyperpolarizes $V_{rest}$ in sustained VGNs.*

Comparison of $V_{rest}$ of individual VGN before and after $Na_V1.6$ block. **A:** Sustained firing VGNs (n = 5) show a significant decrease in $V_{rest}$ relative to **B:** transient VGNs (n = 8).

We next tested whether $Na_V1.6$ current block changed spike timing regularity. We stimulated firing in VGNs with frozen trains of EPSCs to evoke spike trains (Kalluri et al., 2010) (n = 9) (Figure 3.6). We measured spike regularity using coefficient of variation (CV). Blocking $Na_V1.6$ current failed to significantly effect CV (paired t-test; p = 0.29, power = 0.17). In 5 out of the 14 VGNs tested, $Na_V1.6$ current block eliminated pseudo-EPSC induced spiking. In the remaining 9 VGNs, spiking was already irregular, and blocking $Na_V1.6$ currents did not further

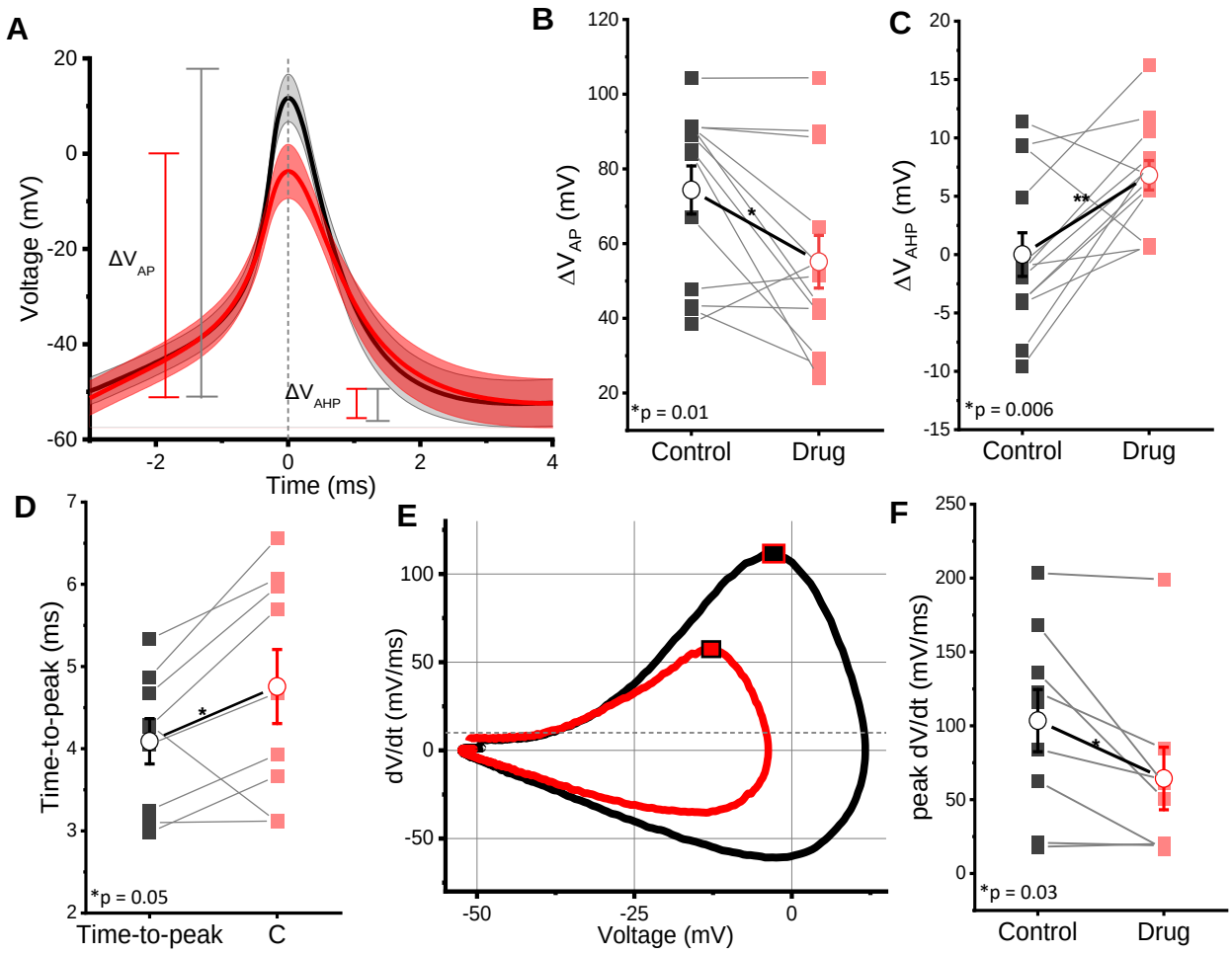


*Figure 3.5 Spike height, AHP, time-to-peak and peak dV/dt decreases with 4,9-ah-TTX.*

**A:** Application of 4,9-ah-TTX (red) changed the AP waveform relative to control APs (black). We observed **B**: decreases spike height and **C:** AHP, **D**: increases time-to-peak and **E&F**: decreases peak dV/dt (closed squares) on average in all VGNs (n = 13).

enhance irregularity. For the most regular VGN, the large increase in CV from 0.2 to 0.6, (Fig 7) suggests the possibility that $Na_V$ current block matters more to the sustained neurons, but this remains to be determined. In some cases, spiking was already irregular, and blocking $Na_V1.6$ currents did not further enhance irregularity.

In summary, these data indicate that blocking $Na_V1.6$ currents decreases excitability through hyperpolarizing resting membrane potential only in sustained VGNs and increasing current threshold for spiking and decreasing spike rate for all VGNs. There was also an impact on AP waveform and kinetics: 4,9-ah-TTX application decreased spike amplitude and AHP, but did not have a consistent effect in spike regularity. $Na_V1.6$ currents may therefore be key for decreasing spike latency relative to stimulus onset (as shown by decreased time-to-peak) and increasing the rate of depolarization.

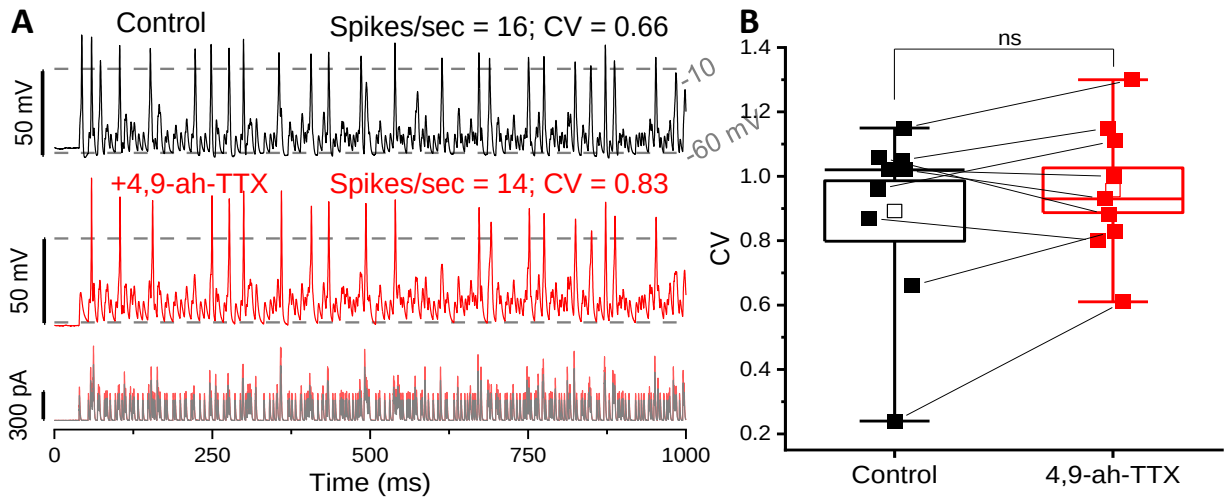


*Figure 3.6 4,9-ah-TTX did not impact spiking regularity.*

**A:** Example of spike trains evoked with pseudo-EPSC injection (bottom panel). Dashed lines indicate 0 mV and -60 mV. Application of 4,9-ah-TTX slightly increased CV, indicating decrease in regularity. **B:** On average, block of $Na_V1.6$ currents with 4,9-ah-TTX did not significantly increase CV; 0.89 ± 0.09 vs 0.96 ± 0.07. VGNs with low CV saw a large increase, but VGNs with high CVs (>0.8) experienced little to no additional increase. Box indicates SEM and median, open squares indicate the mean, and whiskers mark 5-95 confidence intervals.

*Enhancement of $Na_V$ currents with ATX-II increases excitability and regularity*

We next applied 100 nM of ATX-II, which reduced $Na_V$ channel inactivation, to test the impact of increased persistent and resurgent currents in VGN spiking in vitro. ATX-II interacts with the open $Na_V$ channel conformation, slowing down or preventing inactivation and thus increasing alternative $Na_V$ current components. In voltage clamp experiments, we noted that ATX-II increased $Na_VT$ and $Na_VP$ currents (see Chapter 2: Transient and persistent currents were enhanced by NaV channel agonist ATX-II).

Application of 100 nM ATX-II on VGN had no significant effect on AP waveform (Appendix Table 26): for example, there were no changes to resting membrane potential (n = 7; paired t-test; p = 0.07), spike height (p = 0.97), or spike width (p = 0.09).

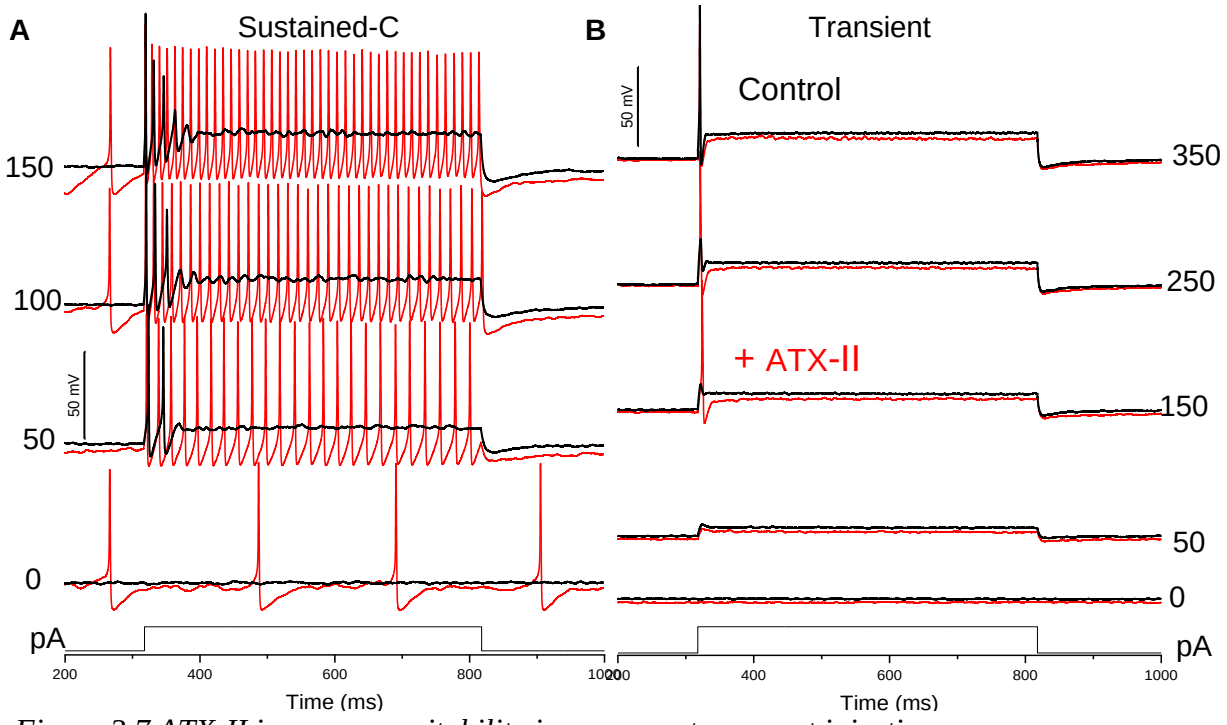


*Figure 3.7 ATX-II increases excitability in response to current injections.*

A: Sustained-C VGN becomes sustained-A like after ATX-II, which induces spontaneous spiking (0 pA). B: Transient VGN remains transient, although ATX-II reduces current threshold for spiking.

ATX-II induced spontaneous spiking in 6 out of 7 cells tested (Fig 3.7A). This means no current injection was needed for the VGN to spike. The cell that did not spike spontaneously (Fig 7.8B) was highly inexcitable in the control condition: it had high current threshold, a transient firing pattern, and irregular spike timing in response to EPSC trains. After ATX-II, current threshold and irregularity decreased (CV from 0.86 to 0.58), but the VGN still spiked transiently. It is possible that this cell had large $K_{LV}$ currents. We did not examine the currents present in the cells in this experiment.

For the 6 other VGNs, 2 were transient, 2 were sustained-C and 2 were sustained-A in the control condition. After ATX-II application, the current threshold for spiking was abolished due

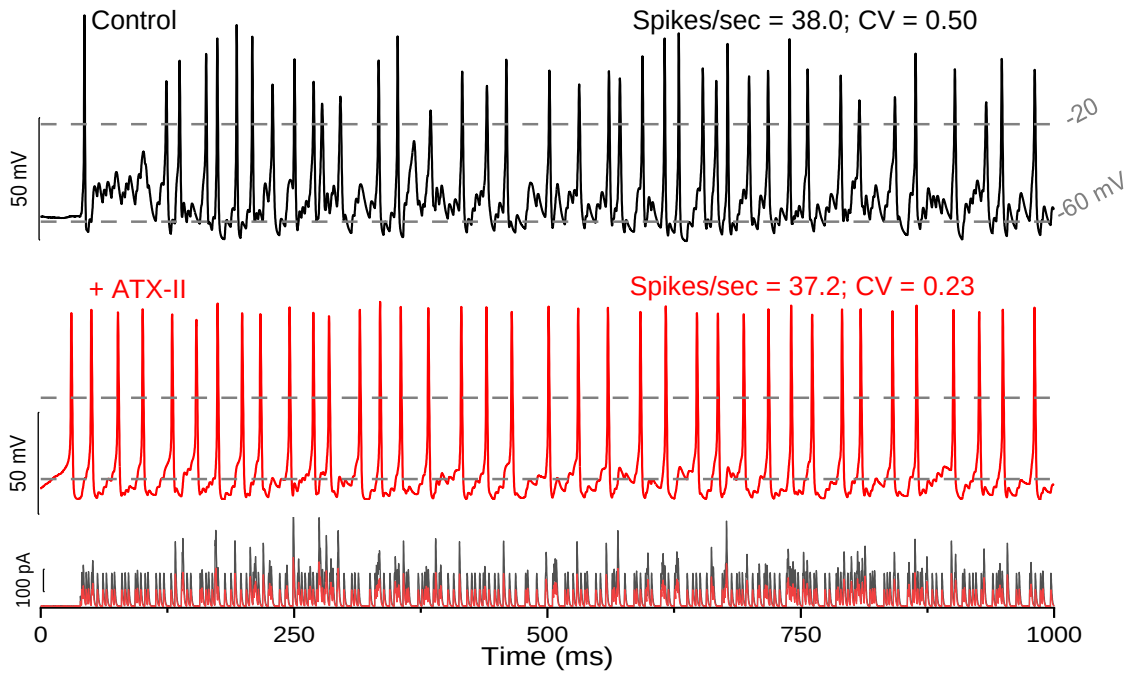


*Figure 3.8 ATX-II increases VGN spiking regularity and changes spiking behavior in sustained-C VGN.*

Top panel: Control spiking in response to EPSC injection (bottom panel, black trace). Middle panel: Spiking response after application of ATX-II increased regularity, even when controlled for changes in spike rate. EPSC injection amplitude was decreased (bottom panel, red trace).

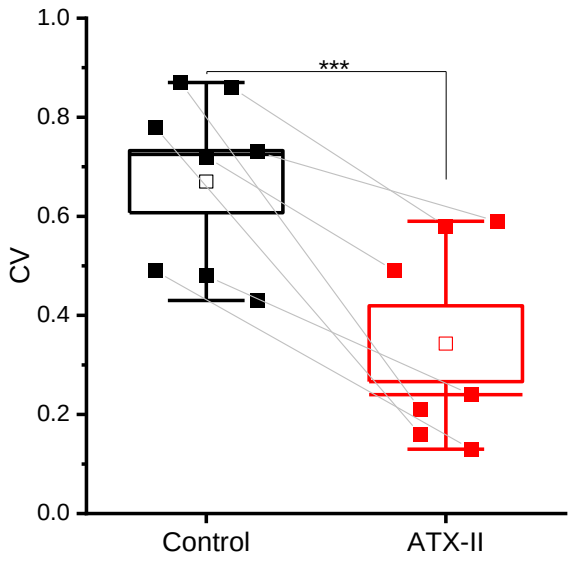


*Figure 3.9 ATX-II decreases CV in VGN spike trains.*

On average, application of ATX-II caused a decrease in CV in pseudo-EPSC evoked spike trains. Box indicates SEM, log line indicates median, open squares indicate the mean, and whiskers mark 5-95 confidence intervals.

to the spontaneous spiking (Fig 3.7A). However, long current injections showed changes to the sub-type of step evoked patterns: they all became sustained-A, with the exception being one transient VGN that became sustained-B-like (not shown).

We then tested the influence of ATX-II on spike regularity in response to pseudo-EPSC injections (Fig 3.8). The primary effects of ATX-II are to increase the number of spikes in response to a train of EPSCs of a given amplitude and duration, as well as increasing spike regularity (decreasing CV). However, CV is rate dependent, decreasing as spike rate increases. To control for this confounding factor, we titrated EPSC size to generate similar spike rates in experimental (ATX-II) and conditions.

On average, the EPSC-evoked spike rate for 8 VGNs tested was 35 spikes/second, both in the control and ATX-II conditions, which is comparable to recorded resting discharge of vestibular afferents in mouse *in vivo* (37 Hz for irregular, 55 for regular) (Lasker et al., 2008). In the control condition, CV averaged 0.63 ± 0.07. After ATX-II, every VGN showed an increase in regularity. CV decreased to 0.34 ± 0.08 (paired t-test; n = 8; p = 0.003, Hedges' g = 0.13) (Fig 3.9).

In summary, ATX-II has the impact of increasing excitability by lowering current thresholds and inducing spontaneous firing, as seen in step evoked firing patterns. EPSC injections

showed that ATX-II also increased spiking excitability in transient and sustained firing VGNs. This suggests that increased larger sodium currents increase excitability and regularity in VGN firing. However, we are unable to determine the impact of specific sodium current components (transient, persistent, resurgent) as ATX-II enhances all these components.

***Discussion***

Here, we examined the sodium conductance and the impact it has on firing patterns and AP waveform. These data indicate that while sustained-A VGNs may not necessarily have greater Na conductance relative to transient VGNs, maximum $Na_V$ conductance density correlates with features such as spike amplitude, AHP and peak rate of depolarization. Blocking $Na_V1.6$ decreased spiking excitability by increasing current threshold, decreasing spike amplitude and peak rate of depolarization, as well as hyperpolarizing resting membrane potential. Enhancing $Na_V$ currents with ATX-II increased spiking excitability and regularity. However, given the lack of specificity of these pharmacological agents for $Na_VT$, $Na_VR$, or $Na_VP$ current modes, we are unable to assess the roles of specific sodium current components on VGN firing.

Transient and sustained VGNs have constitutive differences in their excitability, driven in large part by different complements of ion channels. Kalluri et al. (2010) showed that transient VGN have high intrinsic irregularity. The transient neuron could fire a spike in response to a single, large pseudo-EPSC when spaced regularly at long equal intervals (<300 ms). However, as the intervals were systematically shortened (down to 10 ms; note that these were room temperature observations), transient VGNs became less likely to fire an AP for each EPSC, presumably due to the inhibitory influence of $I\text{-}K_{LV}$ and $Na_V$ channel inactivation lingering from the preceding spike. Therefore, even if the pseudo-EPSC input itself is regular, transient VGNs still fired irregularly.

This demonstrates that the variability present in isolated transient VGN does not stem entirely from variability in injected stimuli. This constitutive irregularity may be key for producing the high intrinsic variability associated with precise spike timing seen in irregular VGN in vivo.

While transient VGN have high intrinsic variability, sustained VGNs have high sensitivity (tendency to fire). In the same experimental series, Kalluri et al. (2010) showed that sustained VGNs increased in spike rate as pseudo-EPSC intervals decreased (i.e., a greater ratio of APs per number of pseudo-EPSCs) and could keep up with short intervals of 10 ms. In other experiments, blocking I-$K_{LV}$ made transient VGNs fire with greater regularity and reduced spiking threshold; not only did reducing I-$K_{LV}$ reduce the size of EPSCs needed to elicit firing, this block also increased the number of APs per pseudo-EPSC at smaller intervals. Thus, high I-$K_{LV}$ in mature transient VGNs seems to correspond with increased variability, while low or moderate I-$K_{LV}$ in mature sustained VGN corresponds with increased sensitivity.

The precise impact of I-Na current components on spike timing regularity is still unknown. However, given the results from this current study and the known kinetics of different $Na_V$ currents (Raman and Lewis, 2014; Liu et al., 2016), we theorize that having larger sodium currents in general would increase $Na_V$ channel availability to facilitate tonically high-rate firing of regular afferents. Additionally, having I-$Na_V$ currents active below or at spike threshold (e.g., persistent Na current) would increase sensitivity and probability of firing. For example, the expression of non-inactivating persistent and resurgent currents close to the spike initiation zone may enhance spiking excitability (Meredith and Rennie, 2020). In the next chapter, we assess the roles of $Na_V$ currents during the AP waveform.

***Methods***

***Cell preparation, whole cell recording, and pharmacology:*** Cells were prepared, recorded, and treated pharmacologically as described in Chapter 2.

***Recording solutions:*** During current clamp experiments, cells were bathed in a physiological external solution ("standard solution") containing (in mM): 144 NaCl, 0.7 $NaH_2PO_4$, 5.1 KCl, 1.3 $CaCl_2$, 0.9 $MgCl_2$, 10 HEPES, 5.6 D-Glucose, titrated with NaOH to a pH of 7.4, ~310 mmol/kg. The internal pipette solution for current clamp experiments contained 135 KCl, 0.5 MgCl, 3 Mg-ATP, 5 HEPES, 5 EGTA, 0.1 CaCl, 0.1 Na-cAMP, 0.1 Li-GTP, 5 Na2 creatine phosphate, pH 7.25 with KOH, ~285 mmol/kg. Membrane voltages were corrected offline for liquid junction potential of 4.7 mV.

***Analysis:*** Analyses of spikes were performed in MATLAB (The MathWorks, Natick, MA) and Clampfit (Axon Instruments, Molecular Devices). Figures and statistical analysis were done in Origin Pro 2018 (OriginLab, Northampton, MA) or MATLAB. Mean ± SEM are presented. For comparisons between 2 groups, we estimated statistical significance with Student's t-test when variances were equal, with Welch's t-test when variances were not equal, and paired t-tests between two measures of the same sets of cells. We used an alpha level of 0.05 for all statistical tests. Effect size, Hedges' g with bias correction for small sample sizes, was used to indicate the degree of difference between means. In some cases, one-way ANOVA were applied following a post hoc Tukey's HSD analysis.

Regularity of spike trains was calculated as coefficient of variation (CV) using standard deviation and mean interspike interval (ISI):

$$CV = \frac{\sigma(ISI)}{\mu(\mathrm{ISI})} \qquad Eq\ 5$$

## Chapter 4 – AP Clamp reveals $Na_V$ current kinetics impacts depolarization phase of AP waveform


### *Abstract*

Voltage-gated currents contribute to APs in ways that depend on their voltage dependence and kinetics. A technique to determine the impact of a particular current component on the AP waveform is the AP clamp method. Using this technique, we examined how $Na_V$ currents flow during VGN spiking. We observed that the rate of $Na_V$ current flow is related to the initial depolarization phase of the AP. In transient VGNs, more $Na_V$ current flowed by the peak rate of depolarization relative to sustained VGN. Using 4,9-ah-TTX to isolate $Na_V1.6$ currents, we demonstrated that $Na_V1.6$ currents make up most of the $Na_V$ current during an AP. Sustained VGNs had more $Na_V1.6$ current during an AP, which flowed mostly during the initial phase of depolarization. These data indicate that sustained VGNs have differences in AP waveforms and/or $Na_V$ current kinetics relative to transient VGNs that may enhance spike excitability.


### *Introduction*

Vestibular ganglion neurons are known to have many kinds of voltage-gated channels and currents. The impact of many of these currents on spike timing is still being investigated; the best studied are $K_{LV}$ currents (Iwasaki et al., 2008; Kalluri et al., 2010; Hight and Kalluri, 2016) and HCN currents (Ventura and Kalluri, 2019), which were investigated using a combination of electrophysiological and computational experiments.

However, to our knowledge, no published study has examined the impact of currents on action potential (AP) waveform in VGNs using the AP clamp technique. The AP clamp technique is used to examine the internal anatomy of an AP by dissecting the contributions of particular currents to the changes in voltage (Bean 2007; Carter and Bean, 2009). Using an AP as a voltage

stimulus, recorded only minutes earlier, currents can be evoked with the same time course and size they experience during a natural AP (Bean 2007; Carter and Bean, 2009).

In this section, we use AP clamp to demonstrate the flow of $Na_V$ currents during AP waveforms in VGNs. First, we show that the $Na_V$ current flow precedes the fast depolarization of the AP. Then, using 4,9-ah-TTX, we show how $Na_V1.6$ currents make up most of the current during APs. We conclude that sustained VGNs have differences in the underlying channel kinetics

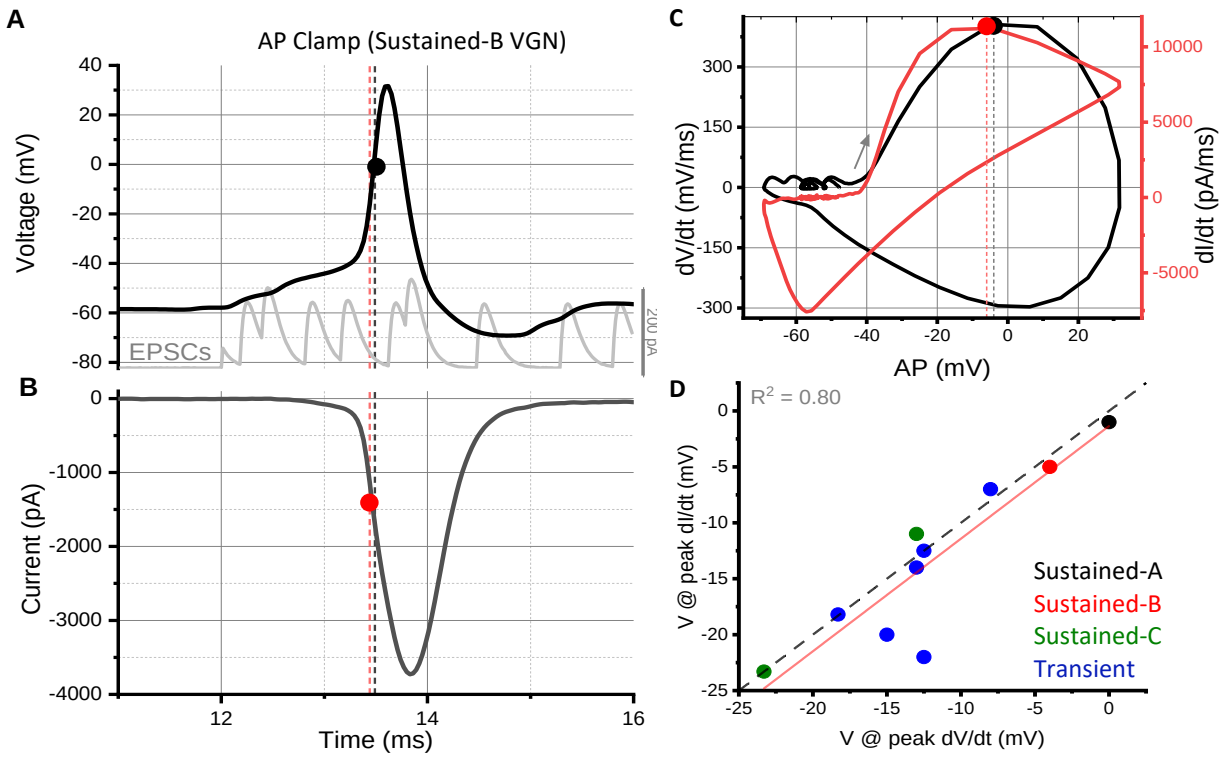


*Figure 4.1 AP clamp shows sodium entry driving depolarization phase of AP.*

**A:** Action potentials were evoked using trains of pseudo-EPSCs and immediately used as a voltage stimulus to evoke $Na_V$ currents, which were isolated using TTX (**B**). Circles correspond to peak dV/dt (black) and peak dI/dt (red). **C:** Phase plane plots were calculated for each action potential and current trace. Grey arrow indicates direction of depolarization. Red dotted line in A, B, and C indicates peak dI/dt. Black dotted line corresponds to peak dV/dt. **D**: Plotting voltage corresponding to the peak dV/dt against the voltage corresponding to the peak dI/dt shows a positive linear correlation (red line). Dashed line shows line through the origin.

that contribute to currents activating at more negative voltages (before the peak depolarization rate) and greater amounts of $Na_V1.6$ currents during the AP.

***Results***

$Na_V$ currents were measured during firing by using the AP clamp technique, where the cell's own AP is recorded and converted into a voltage command used to evoke currents, causing them to experience the same voltage trajectory as during a natural AP (Fig 4.1A and B) (Bean 2007). VGNs were driven to fire APs by injecting pseudo-EPSCs (Kalluri et al., 2010). $Na_V$ currents were isolated by subtracting currents blocked by 1 µM TTX (blocks all TTX-sensitive $Na_V$ channels) or 100 nM 4,9-ah-TTX ($Na_V1.6$ selective).

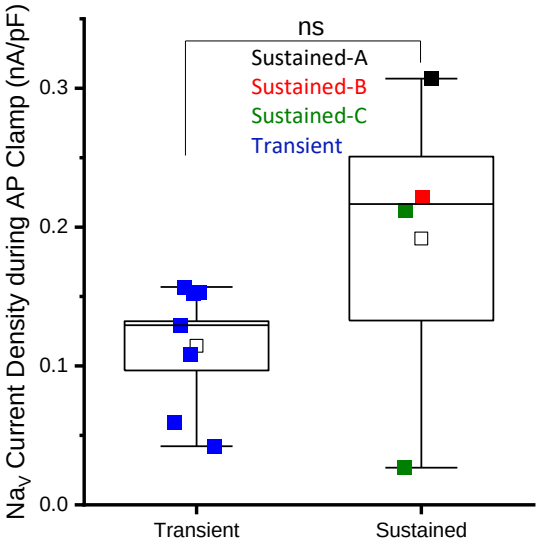


*Figure 4.2 $Na_V$ current density during AP Clamp shows no differences between transient and sustained VGNs.*

$Na_V$ current isolation during AP clamp using TTX showed no difference between transient (n = 7) and sustained (n = 4; sus-A = 1, sus-B = 1, sus-C = 2). Box indicates SEM and median, open squares indicate the mean, and whiskers mark 5-95 confidence intervals.

*Sodium current flow drives depolarization phase of action potential*

Using 1 µM TTX to isolate the current, $Na_V$ current densities during APs were not different between transient (0.11 ± 0.02 nA/pF, n = 7) and sustained VGNs (0.19 ± 0.06 nA/pF, n = 4) (Welch's t-test, p = 0.29, power = 0.29) (Fig 4.2). However, in calculating derivatives for both kinds of spiking, we observed that the voltage corresponding to the peak dV/dt of action potentials (Fig 4.2A and C, black circle) lagged the voltage corresponding to peak current change (dI/dt) (Fig 4.1B and C, red

circle) (Figure 4.1D, R-squared = 0.80). The dashed black line in Figure 4.1D corresponds to the line through the origin. These data indicate that the upstroke of the AP is being driven in great part by the sodium current, as voltage of peak depolarization follows the voltage of the peak current flow (Bean, 2007).

Taking the integral of $Na_V$ current, we then calculated the cumulative current entry at peak dV/dt (Fig 4.3A and B). In transient VGNs, 17 ± 3% of the $Na_V$ current had flowed (Fig 4.3C). In

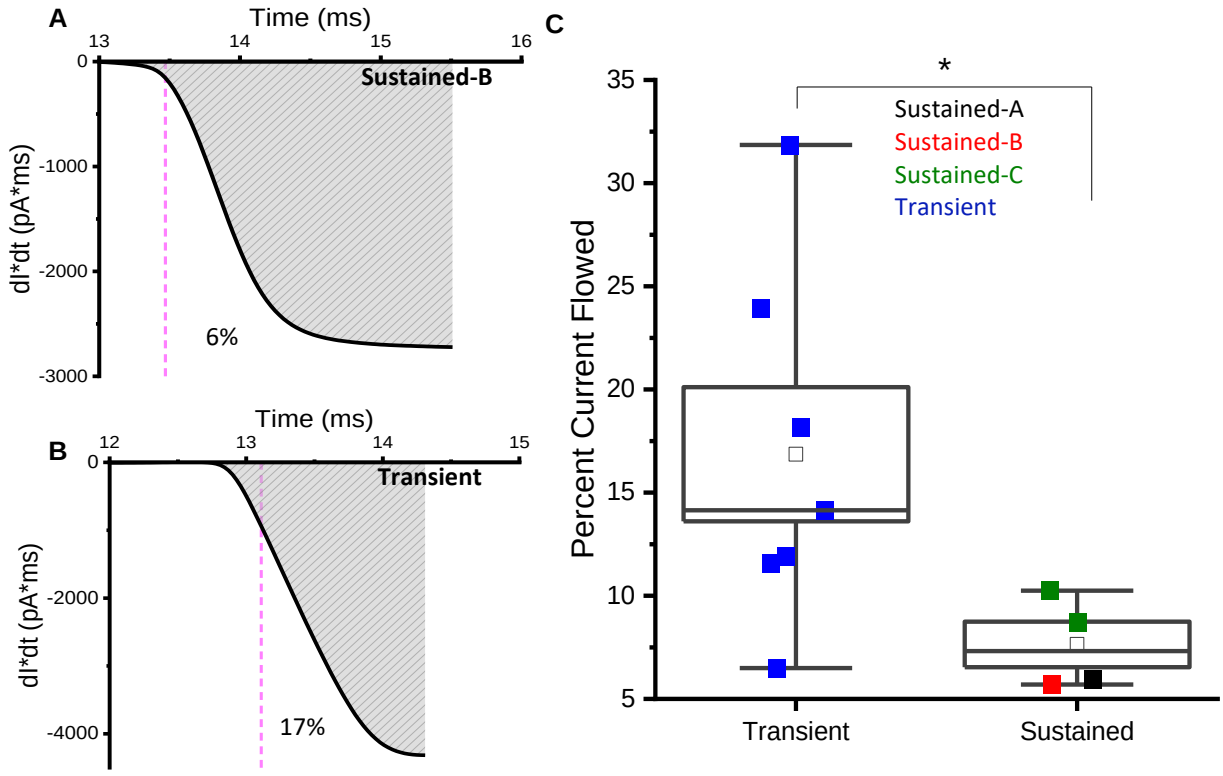


*Figure 4.3 More $Na_V$ current has flowed by the time of peak dV/dt in transient neurons relative to sustained.*

**A** and **B**: In taking the integral of the current over time, we calculated the total current that flowed (shaded area under the curve) in an exemplar sustained-b and transient VGN, respectively. The pink dashed line corresponds to the time point where peak rate of depolarization (dV/dt) was reached. **C**: On average, more $Na_V$ current flowed by the peak dV/dt in transient VGN relative to sustained VGN, suggesting that sustained VGNs may different $Na_V$ channel kinetics (i.e., greater proportion of non-inactivating channels).

sustained VGNs, only 8 ± 1% flowed before peak dV/dt (Welch's t-test, p = 0.03, Hedges' g = 0.61) (Fig 4.3C). In addition to intrinsic differences in excitability, we suspect that $Na_V$ currents are different between sustained and transient VGNs. Given that we observed minimal differences in AP waveform, no differences in maximum sodium conductance or sodium current densities, we hypothesize that the underlying differences in current entry may be attributed to I-$Na_V$ kinetics (Bean and Carter, 2009). For example, this suggests that sustained VGNs have a greater proportion of $Na_V$ channels that do not inactivate.

*Sustained VGNs have more $Na_V$1.6 current flow during APs*

In a different set of VGNs, while there was no difference in the $Na_V$T block between transient (n = 8) and sustained (n = 5) VGNs (see page 36), we observed a difference in $Na_V$1.6 current flow during APs. 4,9-ah-TTX block during AP clamp showed that $Na_V$1.6 currents are a

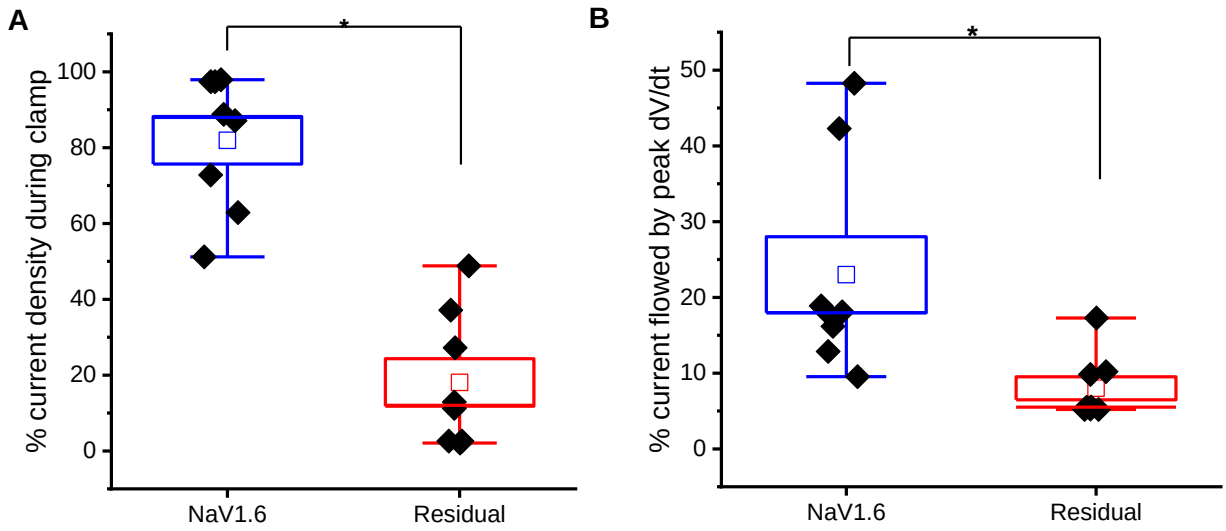


*Figure 4.4 $Na_V$1.6 currents make up the majority of current evoked during AP Clamp.*

**A:** $Na_V$1.6 currents also made up the majority of the current before peak dV/dt (p = 0.03), shown here in representative sustained-b and transient VGNs, indicating a more negative voltage dependence relative to the residual non -$Na_V$1.6 current (see Chapter 1). **B:** $Na_V$1.6 currents make up most of the current flow during AP Clamp in sustained VGNs (p = 0.01)

significant fraction of current flow during AP clamp (Fig 4.5A). On average, in the 8 VGNs, $Na_V1.6$ current makes up approximately 80% of the total sodium current density (0.20 ± 0.04 nA/pF) (Fig 4.4A and Appendix Table 27). This is relative to non-$Na_V1.6$ (residual) currents (0.05 ± 0.02 nA/pF) (One-way ANOVA, Tukey's HSD, p = 0.01, Hedges' g = 0.05). Additionally, more $Na_V1.6$ current (22.99 ± 5.01%) flowed by the peak dV/dt relative to residual current (7.99 ± 1.52%) (p = 0.03, Hedges' g = 0.88) (Fig 4.4B and Appendix Table 28). These data show that $Na_V1.6$ currents contribute significantly to the initial phases of the depolarization.

In our limited sample, total sustained and transient VGNs had different amounts of 4,9-ah-TTX sensitive ($Na_V1.6$) current densities during AP clamp: sustained VGNs (n = 3) had 0.29 ±

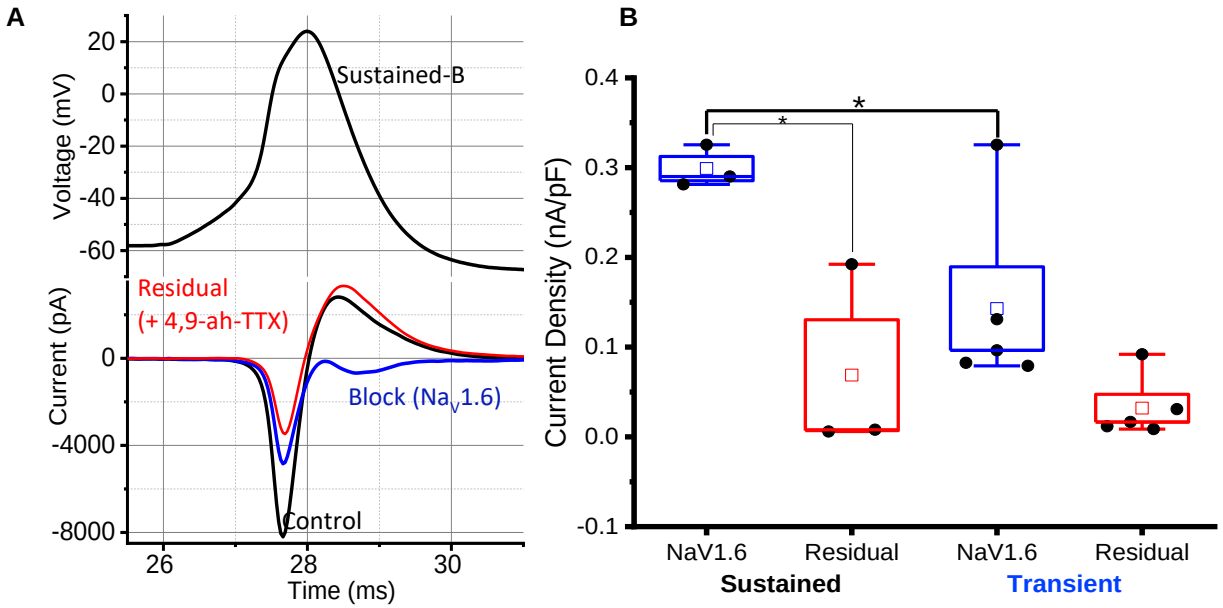


*Figure 4.5 AP Clamp shows $Na_V1.6$ currents contribute significantly to spiking in sustained VGN.*

**A:** Currents evoked by action potential clamp in a sustained-b VGN before and after application of 100 nM 4,9-ah-TTX and the digital subtraction ("blocked"). The second inward "hump" revealed by the block is non-inactivated Na current. **B:** Sustained firing VGNs had significantly more NaV1.6 current flow during APs relative to transient VGNs (p = 0.01).

0.01 nA/pF while transient VGNs (n = 5) had 0.14 ± 0.05 na/pF (p = 0.03, Hedges' g = 0.06) (Fig 4.5B). Sustained VGNs also had a significant difference between $Na_V1.6$ and residual current (0.06 ± 0.06 nA/pF, p = 0.01, Hedges' g = 0.11) (Fig 4.5B). A two-way ANOVA suggests there was no interaction between firing pattern (sustained vs. transient) and current block ($Na_V1.6$ and residual) (p = 0.15), meaning firing patterns did not influence differences between $Na_V1.6$ and residual currents (Appendix Table 29). Lacking specific blockers, we could not selectively probe the impact of persistent and resurgent components on firing patterns in current clamp. But the $Na_V1.6$ blocker shows how $Na_V1.6$ currents contribute to excitability, and that $Na_V1.6$ channels are a significant contributor to spikes.

***Discussion***

In summary, even though there was no difference the overall $Na_V$ current density between transient and sustained firing VGNs (Fig 4.1), we observed a difference in the amount of current flow by the time of peak dV/dt, suggesting differences in either AP waveform and/or underlying $Na_V$ channel kinetics (Fig 4.2). In Chapter 3 we demonstrated that sustained firing VGNs had greater AP amplitudes and deeper AHPs, both of which were correlated with maximum $Na_V$ conductance (Fig 3.1). We are unsure of whether these differences drive or are driven by $Na_V$ currents, but they are undoubtedly related. We also demonstrated the tight relationship between the inward flow of $Na_V$ current and the initial depolarization of the AP; the voltage corresponding to peak rate of $Na_V$ current flow equaled or preceded the voltage corresponding to the peak rate of depolarization in 8 out of 10 VGN (Fig 4.2). This is a beautiful demonstration of the $Na_V$ current being the primary depolarizing force in spiking.

We observed that $Na_V1.6$ currents made up approximately 80% of the current during the AP – unsurprisingly, since $Na_V1.6$ currents make up 70% of the total $Na_V$ current (Chapter 2). If the $Na_V1.6$ currents and residual currents had similar voltage dependence and kinetics, we would expect an equal contribution to the AP. However, we were interested to see that the $Na_V1.6$ current made up the greater proportion the current during the depolarization phase of the AP (Fig 4.4B).

Keeping in mind we did not detect an overall difference in $Na_V1.6$ currents between transient and sustained VGN (Chapter 3), we were surprised to see that sustained VGNs had greater $Na_V1.6$ current density during AP clamp. Although we were not able to examine other voltage-gated currents in VGNs using AP clamp, we were interested to find differences in $Na_V$ current densities between transient and sustained VGNs. Sustained VGNs had larger 4,9-ah-TTX-sensitive currents during AP clamp, which make up most the current flowing during the depolarization phase of the AP.

The AP clamp technique has been previously utilized to reveal the impact of $Na_V$ currents on firing. For example, Raman and Bean (1997) showed that resurgent current increased current flow during conglomerate AP waveforms in Purkinje neurons. CA3 neurons, which do not have resurgent current, did not show any $Na_VR$ current flow during multiple APs (Raman and Bean, 1997). Gittis et al. (2010), in studying GABAergic and non-GABAergic medial vestibular nuclei (MVN) neurons showed that although $Na_V$ current densities were the same in both cell types, $Na_V$ currents decayed faster and inactivation accumulated faster in GABAergic MVN neurons. Interestingly, both types of MVN neurons have similar transient, persistent and resurgent current kinetics. Results from their AP clamp indicated that the difference in $Na_V$ current inactivation

could be attributed to Kv3 (i.e., high voltage-activated potassium) currents, which protect $Na_V$ channels at high firing rates by driving fast repolarization (Gittis et al., 2010).

However, even though evidence suggests that $Na_V1.6$ currents play an important role during APs, we are unable to determine the precise impact of different $Na_V$ current component on VGN spiking due to the nonspecific nature of these pharmacological agents. To assess the roles of $Na_V$ currents, we therefore turn to computational techniques in the next section.

***Methods***

***Cell preparation, whole cell recording, and recording solutions:*** Cells were prepared and were recorded from as described in Chapters 2 and 3 Methods.

***Pharmacology:*** In AP clamp experiments, APs were collected in standard external solution and currents were then blocked by local perfusion of a modified standard solution (where $K^+$ was replaced with $Cs^+$) and supplemented by blockers in sequence: potassium currents were blocked 10nM linopirdine, 1 M 4-aminopyridine, and 25 mM α dendrotoxin, followed by 1 μM TTX to block $Na_V$ currents, and then 100 nM $CdCl_2$ to block $Ca_V$ currents. In other AP clamp experiments, 100 nM 4-9-anhydro-tetrodotoxin was added to normal standard external solution and applied to block $Na_V1.6$ currents before TTX was applied. These solutions were kept in frozen stock solutions and thawed on the day of experiments. The toxin-containing solutions were applied via the same set-up described in Chapter 2: local perfusion (Perfusion Fast-Step, Warner Instruments, Holliston, MA) delivered with a Bee Hive Controller (BASI, West Lafayette, IN).

***Analysis***: Analyses were completed as described in Chapters 2 and 3.

## Chapter 5 – Conductance-based modeling of VGNs indicates resurgent and persistent $Na_V$ currents influence excitability but not regularity, while transient $Na_V$ current impacts both.

### *Abstract*

While recordings from VGNs show effects of $Na_V$ currents on excitability and spike regularity, the lack of specific blockers prevents experimental delineation of the roles of each $Na_V$ current mode. Here we address these questions with a single-compartment model of VGN firing. In simulated VGNs, I-$Na_V$R reduces interspike intervals (ISIs) and first-spike latency in response to current steps and pseudo-EPSC injections. I-$Na_V$P slightly and slowly increases $Na_V$ current during a train of APs. Increases in $Na_V$T current, and not $Na_V$R and $Na_V$P currents, increased regularity independently of increases in rate. Thus, while I-$Na_V$T enhances both excitability and regularity, the model showed effects of I-$Na_V$R and I-$Na_V$P only on excitability.

### *Introduction*

The role of multiple sodium currents in firing patterns and their impact on spike timing regularity is difficult to study. We showed transient currents (I-$Na_V$T) to be primarily responsible for the depolarization phase of the AP using AP clamp. Persistent (I-$Na_V$P) and resurgent (I-$Na_V$R) currents are smaller in amplitude but exhibit relatively slower kinetics and more negative voltage range. We showed, using ATX-II, increased noninactivating currents increased excitability and regularity. This, coupled with their non-inactivating or blocked from inactivation properties, led us to hypothesize that persistent and resurgent currents enhance spiking excitability and increase regularity (Lewis and Raman, 2014).

We are unable to test this hypothesis in vitro. The relatively small size of the currents makes them difficult to record in physiological conditions where spiking behaviors can be assessed. Large

$K_V$ currents, among others, increase voltage errors and make recordings difficult to isolate persistent and resurgent currents. Furthermore, our experiments also indicate that significant components of I-$Na_V$T, I-$Na_V$P, and I-$Na_V$R are carried by $Na_V$1.6 channels and are pharmacologically indistinguishable (Fig 2.7). We therefore opted for the computational approach initiated by Hight and Kalluri (2016).

Using this method, $K_{LV}$ conductances have been shown to be key in driving irregularity: increasing $K_{LV}$ conductances, regardless of the amount of Na conductance, universally increased irregularity (Ventura and Kalluri 2019, Hight and Kalluri 2016). These simulations used Na conductance parameters that originated from the ventral cochlear nucleus neuron model in Rothman and Manis (2003c), who gathered $Na_V$ current data from various studies of other types of neurons, such as rat hippocampal CA1 neurons (Costa 1996). For our study, we adjusted the expression for I-$Na_V$T using parameters gathered in our experiments. Additionally, we added expressions for I-$Na_V$P and I-$Na_V$R based on the formulation developed by Wu et al. (2005) and Venugopal et al. (2019), updated with parameters from our data to simulate the role of I-$Na_V$R and I-$Na_V$P in VGN firing.

Using injected current steps and pseudo-EPSCS to evoke firing patterns and spike trains, respectively, from simulated VGNs, we found that I-$Na_V$R and I-$Na_V$P increased excitability, but not necessarily regularity, in sustained model VGNs. Increasing the conductance of $Na_V$T increased regularity in both transient and sustained model VGNs.

## *Results*

### *Modeling of $Na_V$ current components in VGN firing*

We used a single-compartment conductance-based VGN spiking model in which we control the amount of I-$Na_V$T and the addition of I-$Na_V$P and I-$Na_V$R (Venupogal et al., 2019). The equations describing $g_{KLV}$, $g_{KH}$, $g_H$, and $g_{leak}$ were those used by Ventura and Kalluri (2019) to describe spiking in rat VGNs. Sodium channel density for the transient current was set to 20 mS/cm$^2$ for sustained-A model neurons, 16 mS/cm$^2$ for sustained-B model neurons, 13 mS/cm$^2$ for sustained-C neurons, and 11 mS/cm$^2$ for transient neurons (see Chapter 5 Methods).

We repeated simulations with four $Na_V$ conditions: I-$Na_V$T alone, or with I-$Na_V$P ("I-$Na_V$T + P"), or I-$Na_V$R ("I-$Na_V$T + R"), or both I-$Na_V$P and I-$Na_V$R ("I-$Na_V$T + P + R"). I-$Na_V$P and I-$Na_V$R are simulated with either "low" or "high" conductance density values based on currents

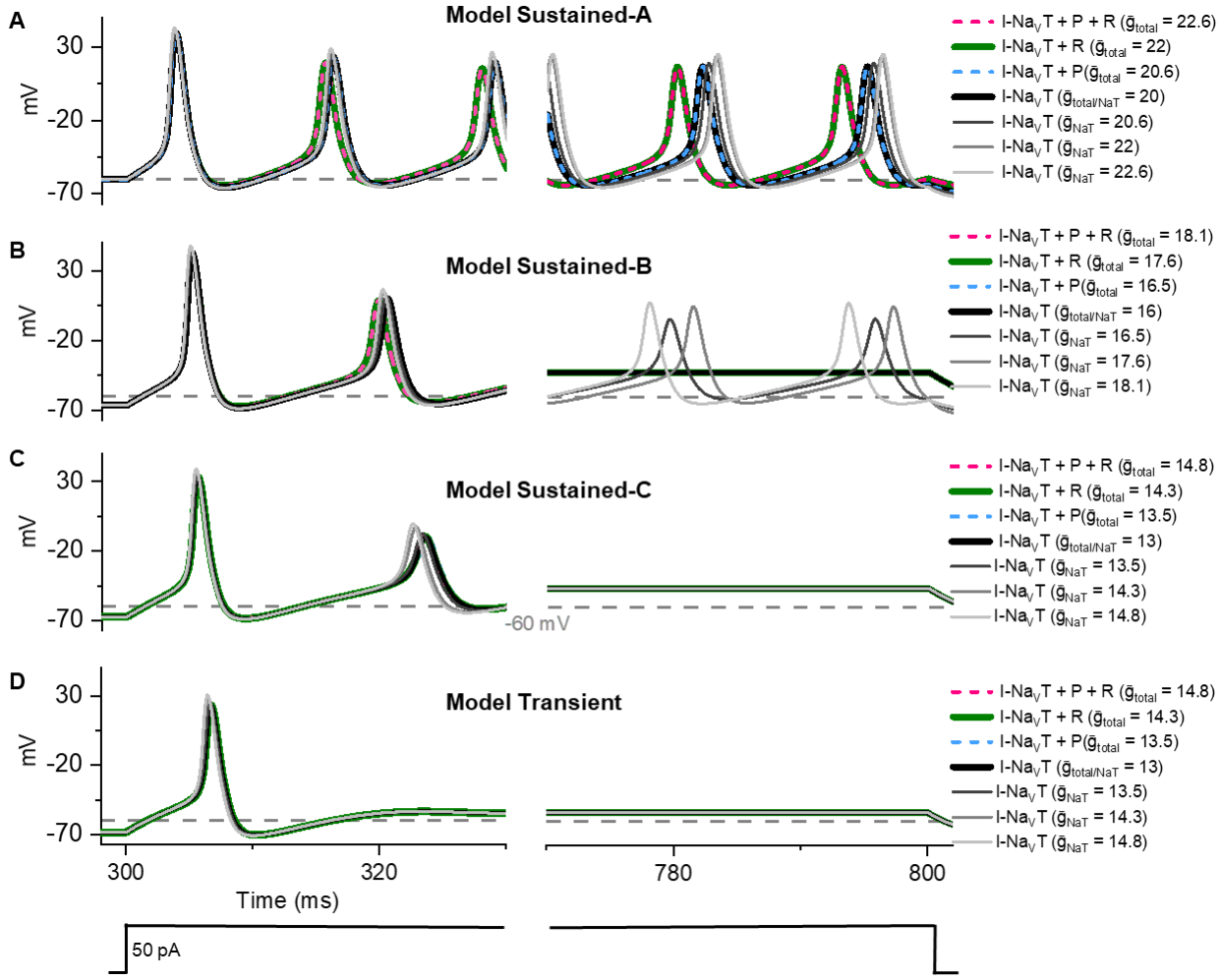


*Figure 5.1 Increasing I-$Na_V$T had different excitatory effect than I-$Na_V$R or I-$Na_V$P currents in model VGNs.*

All model VGNs were stimulated with 50 pA current step. Conductance ($\bar{g}$) is in units of mS/cm$^2$. **A**: Step-evoked firing pattern of a sustained-A model VGN. B: Increasing I-$Na_V$T in sustained-B model induced full spike train, like sustained-A. I-$Na_V$R reduces refractory period at the start of spiking. **B**: Increasing I-$Na_V$T in sustained-B model induced full spike train, like sustained-A. I-$Na_V$R reduces refractory period at the start of spiking. **C**: In sustained-C model, no obvious effect of I-$Na_V$P and/or I-$Na_V$R and increasing I-$Na_V$T increased spike rate. **D**: Transient model showed no effect of I-$Na_V$R and/or I-$Na_V$P currents and increasing I-$Na_V$T only increased spike height. Base $\bar{g}_{NaT}$ was set to 13 mS/cm$^2$ to elicit spike at this current step.

recorded in voltage clamp experiments from cell bodies in this study (1% and 5% of I-Na$_V$T, respectively; see Table ) and afferent endings in Meredith and Rennie (2020) (3% and 10%). These current components are represented by Eq 6 and Eq 7. We also describe control simulations that increase $g_{NaT}$ to match the increase in total conductance density caused by adding I-Na$_V$P and I-Na$_V$R conductances in the other simulations, and to explore the range of Na$_V$T conductance recorded. The current-voltage relations of the simulated currents reproduce key voltage-dependence and kinetic properties of the data (Fig 2.5).

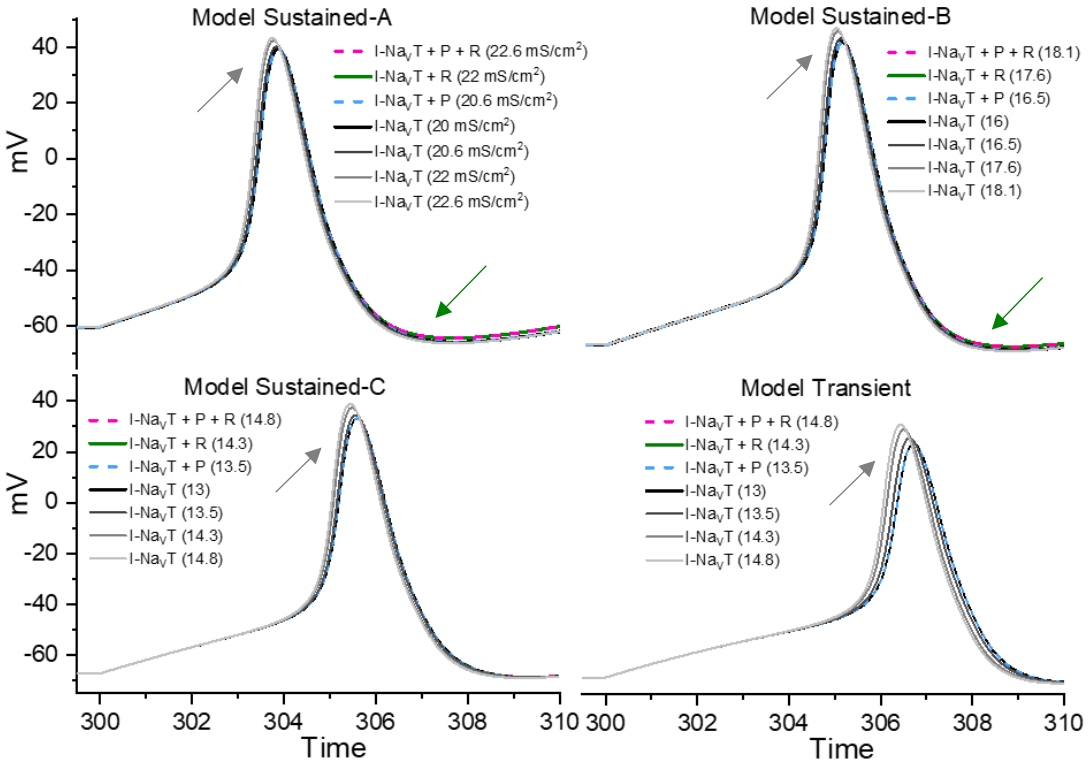


*Figure 5.2 I-Na$_V$T increases spike height and I-Na$_V$R reduces refractory period in APs.*

APs from the first 10 ms of spike trains in Figure 5.1. I-NaVR becomes apparent during repolarization phase in model sustained-A and sustained-b APs (green arrows). Increased I-Na$_V$T increases spike height and rates of depolarization in all model APs (grey arrows). I-Na$_V$P is indistinguishable from control conditions.

*Resurgent current reduces ISI in response to current steps*

We examined the response of model VGNs to long current injections to examine the role of these currents in the context of multiple spikes. In Figure 5.1, we show the first and last 30 ms response of modeled VGNs to a 500-ms current step (i.e, Fig. 3.1

). Each panel shows a firing pattern under seven different $Na_V$ current conditions: I-$Na_V$T, I-$Na_V$T + P, I-$Na_V$T + R, and I-$Na_V$T + P + R, and three I-$Na_V$T control conditions. In this figure we only show the "high" (3% and 10%) levels of I-$Na_V$P and I-$Na_V$R which show a clearer effect relative to control conditions.

Sustained-A and sustained-B (Fig 5.1A and B) show the most noticeable effect of I-$Na_V$T + P + R; they are also the VGNs with the smallest $K_{LV}$ conductance density (0 and 0.42 mS/cm2, respectively). The sustained-A and sustained-B models showed a reduced refractory period after the first spike in the I-$Na_V$R conditions (Fig 5.2). Sustained-C model VGN showed a slight dampening of voltage oscillations and thus reduced number of spikes when I-$Na_V$R is added. There was no effect on model transient VGNs, which have the largest $K_{LV}$ conductance density (1.1 mS/cm2). Thus, added I-$Na_V$R increased spiking excitability of specifically model sustained VGNs in response to current steps. This is reminiscent of the impact of 4,9-ah-TTX on sustained VGNs *in vitro*, where excitable VGNs showed a greater effect of $Na_V$1.6 block on spiking. In this simulation, we saw no effect of added I-$Na_V$P on spiking in any model VGNs, possibly due to the small conductance density of this current.

*Increasing transient current increases spike rate in response to current steps*

To probe whether effects of adding I-Na$_V$R simply reflected the increase in Na$_V$ conductance density, we then increased I-Na$_V$T (by increasing $g_{NaT}$) by the same amounts (Fig 5.1).

For a single AP, increasing I-Na$_V$T increased spike amplitude and rate of depolarization in all model VGNs, as is shown by the first APs in the spike trains in Figure 5.2. These simulations also show that increasing I-Na$_V$T in the sustained-B and -C models increased spike rate, making

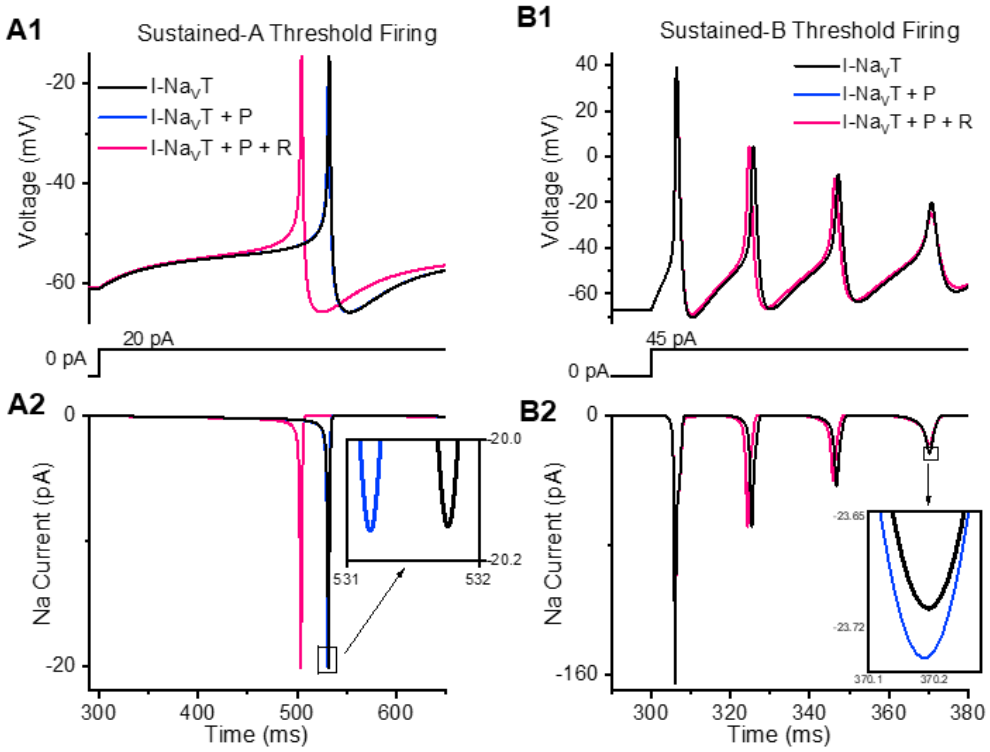


*Figure 5.3 I-Na$_V$P and I-Na$_V$R did not alter current step threshold but decreased spike latency in model VGNs.*

**A:** Model sustained-A firing at 20 pA 500 ms step current injection. **B:** Model sustained-B firing in response to 45 pA 500 ms step current injection. **A1 and B1**: APs in three simulations. I-Na$_V$T+P+R shows decreased spike latency. **A2 and B2:** Na$_V$ currents corresponding to APs in A1 and B1. **Insets** show I-Na$_V$T+P in slight offset to I-Na$_V$T.

sustained-B model VGN more sustained-A-like, and sustained-C model VGN more sustained-B-like (Fig 5.1B and C). As I-Na$_V$T increases more, more spikes are elicited (not shown), similar to the effect of ATX-II application on VGN spiking *in vitro.* All the spikes in the evoked firing patterns became taller and faster as I-Na$_V$T was increased (Fig 5.2). In the sustained-A and -B model VGNs, increasing I-Na$_V$T slightly decreased the ISI after the first spikes relative to control I-Na$_V$T (Fig 5.1A and B). However, by the end of the spike train in the model Sustained-A, the increased I-Na$_V$T conditions showed an increase in the ISI relative to the control conditions, likely due to more accumulated inactivation.

In summary, I-Na$_V$R decreased refractory period (increased rate) in sustained-A and -B model VGN but not in sustained-C or transient model VGNs. Increasing I-Na$_V$T did not decrease refractory periods but increased spike rate in sustained-B and -C step-evoked firing and increased spike height in all VGNs. In these simulations of firing evoked by current steps, we did not observe an effect of I-Na$_V$P, possibly due to the small conductance density of this current.

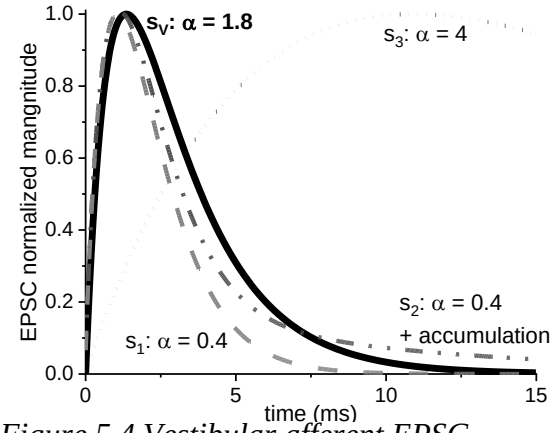


*Figure 5.4 Vestibular afferent EPSC compared to modeled cochlear afferent EPSCs.*

Simulated EPSCs used in the model ($s_V$) were modeled after spontaneous vestibular synaptic potentials recorded in mouse calyces. EPSCs previously used (s1, s2, and s3) in Hight and Kalluri (2016) were based on cochlear EPSCs and altered to match spatiotemporal averaging of synaptic input theorized in some peripheral vestibular afferent endings.

*Persistent and resurgent currents do not alter current threshold but reduce spike latency*

We then asked whether the addition of sodium currents reduced current threshold for spiking. Figure 5.3 shows firing of sustained-A and

sustained-B models and the corresponding $Na_V$ current influx at threshold. In either model, current threshold for firing was not altered by adding I-$Na_V$P or I-$Na_V$R. However, in the sustained-A type model at spiking threshold, spike latency relative to current injection is reduced with I-$Na_V$T + P (0.8 ms) and further reduced with I-$Na_V$T +P + R (30 ms) (Fig 5.3A). The underlying sodium

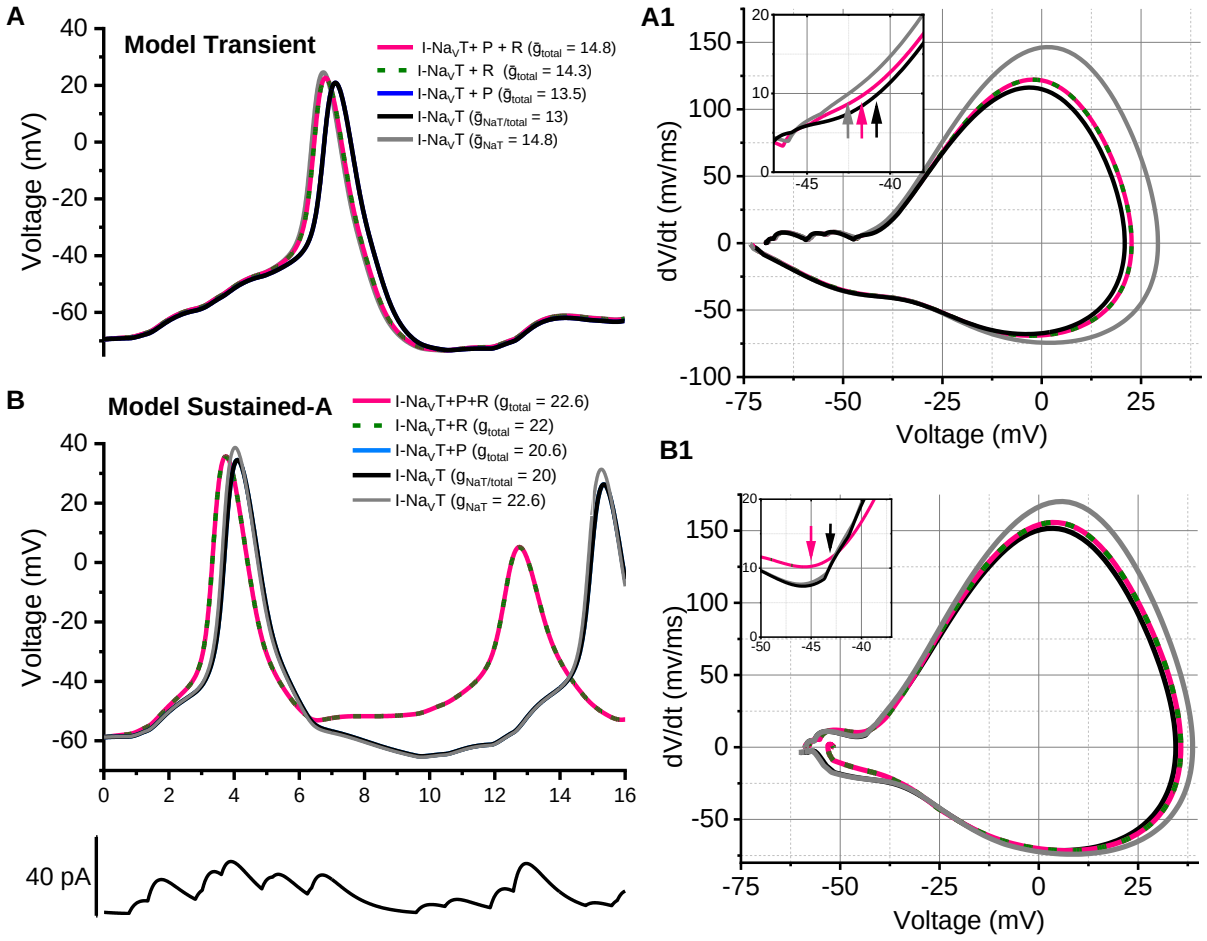


*Figure 5.5 I-$Na_V$R decreased spike onset time in response to pseudosynaptic input in model VGNs.*

Right columns shows **A1**: a sustained-a and **B2**: a transient VGN model stimulated by train of vestibular pseudo-EPSCs below. In addition to I-$Na_V$T+P+R, I-$Na_V$T+R, and I-$Na_V$T+P conditions, we've shown a control I-$Na_V$T conditions that account for changes in $g_{Na}$. Left column (**A2** and **B2**) shows corresponding phase plane plots for initial APs; **Insets** show voltage thresholds in PPP: arrows that indicate 10 mV/ms.

current flow illustrates how the three-component current precedes both the I-$Na_V$T + P and I-$Na_V$T conditions (Fig 5.3A2). I-$Na_V$T + P also has a slight (0.8 ms) lead on the I-$Na_V$T current.

In the sustained-B model, initial spike latency is not reduced by persistent or resurgent current components (Fig 5.3B1). As in Figures 5.1 and 5.2, I-$Na_V$T+ R decreases the ISI after the first spike, but damps voltage oscillations at the end of the train. Figure 5.3B shows how the current amplitudes decrease as the spikes taper off. During the last spike, the I-$Na_V$T + P condition is the largest amount of current flowing, relative to the other conditions (Fig 5.3B2). These simulations show that I-$Na_V$P current and its effect is very small (0.1 pA in size and <1 ms), which is why there is no noticeable effect on spiking at the timescales in previous figures.

*Resurgent current reduces first spike latency in response to pseudo-synaptic stimuli*

We next focused on the impact of different modes of $Na_V$ current on responses to simulated trains of pseudosynaptic stimuli (pseudo-EPSCs) that were modeled after EPSCs recorded from a vestibular afferent calyceal terminal on a type I hair cell (Fig 5.4). We observed the influence of I-$Na_V$R, I-$Na_V$P, and increased I-$Na_V$T on first spike latency in response to a train of vestibular pseudo-EPSCs (Fig 5.5). The average inter-EPSC interval was fixed at 1 ms and the average amplitude was set to 40 pA or 60 pA in order to reliably generate spikes. Figure 5.5 shows the beginning of the spike train responses for four different I-$Na_V$ conditions for each firing pattern.

In the transient model, the addition of I-$Na_V$R decreased first spike latency (Fig 5.5 A1) and slightly depolarized spike voltage threshold (taken to be dV/dt = 10mV; see the phase-plane plot (PPP)) (Fig 5.5 A2). The increase in I-$Na_V$T in the same direction as I-$Na_V$T+R: spike amplitude increased, peak rate of depolarization increased, and voltage threshold hyperpolarized.

In the sustained-A model, the addition of I-Na$_V$R also reduced first spike latency (Fig 5.5 B1). The PPP (Fig 5.5 B2) shows that I-Na$_V$R hyperpolarizes voltage threshold. The second spike latency was also shorter in I-Na$_V$R conditions, but at the cost of spike amplitude. Increasing I-Na$_V$T only slightly reduces spike onset time and increased spike height, especially the second spike in the train.

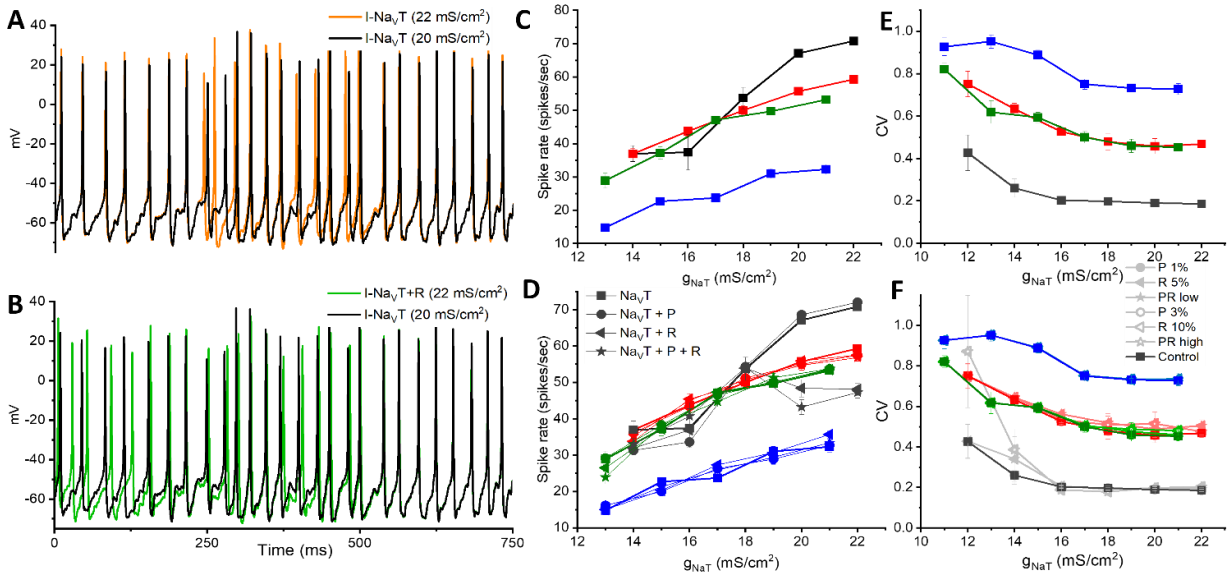


*Figure 5.6 Increased Na$_V$T current increases spike rate and decreases CV but adding Na$_V$P and/or Na$_V$R does not.*

**A**: Example of effect of increasing I-NaVT on CV in model sustained-A shows impact on interspike intervals, decreasing CV from 0.20 to 0.19. **B**: Example of effect of adding I-NaVR on CV in model sustained-A; reduction of refractory period that the beginning of train and addition of a spike indicates increase in excitability but no resulting effect on CV (0.20 to 0.20). **C**: Increasing gNaT , which increases I-NaVT, shows an increase in spike count in response to pseudo-EPSC injections of a constant amplitude (average 30 pA) in all four model VGNs. **D**: Adding in NaVR and/or NaVP current does not further increase spike rate in three model VGNS. In sustained-A model, adding in resurgent current at high level of gNaT induced burst firing, and thus decreased spike rate. **E**: Increasing gNaT decreases in CV when controlling for average spike rate (38.5 spikes/sec) in all four model VGNs. **F**: Addition of NaVR and/or NaVP, in either high or low amount, does not further increase regularity. Note the increase in CV caused by depolarization block behavior at low levels of Na$_V$ conductance. and/or Na$_V$P does not further increase regularity.

In summary, I-$Na_V$R decreases AP response time and threshold to injected EPSCS, reduces ISI, but minimally affects AP waveform; increasing I-$Na_V$T changes AP waveform by increasing spike height and rate of depolarization (peak dV/dt).

*Increased transient, but not added resurgent and persistent currents, increase regularity*

We next examined the role of $Na_V$ currents in spike rate and regularity in model VGN firing. First, we assessed changes in spike rate. The average EPSC arrival time and amplitude was fixed at 1 ms and 30 pA. We observed that increasing I-$Na_V$T steadily increased spike rate (Fig 5.6A) in response to fixed input in all model VGNs. This increase in excitability is due to an increase in amount of depolarizing current. This is reminiscent of the effect of ATX-II had on spiking *in vitro*, where the increase in $Na_V$T (and $Na_V$P) currents increased spike rate to a fixed synaptic input.

We then assessed the impact of I-$Na_V$T on spiking regularity. Since regularity tends to increase as spike rate increases, we sought to assess regularity independently of spike rate by keeping spike rate constant (38.5 spikes/sec) between model VGNs at different levels of I-$Na_V$T by titrating amplitude of synaptic input (arrival time remained fixed at 1ms). Figure 5.6B shows how increasing I-$Na_V$T decreases CV, thereby increasing regularity even when spike rate is kept constant. Model sustained-A VGN have a low CV at this spike rate to begin and show little decrease with increased I-$Na_V$T (0.19 to 0.13). Model sustained-B and -C VGNs show the greatest effects of increased I-$Na_V$T, which go from an average of 0.78 and 0.86 to 0.33 and 0.41 respectively. Again, this is similar to the effect of ATX-II on VGN spiking regularity *in vitro*: increased $Na_V$ currents increases regularity independent of spike rate.

We next examined whether the addition of I-$Na_V$P and/or I-$Na_V$R, at either "low" or "high" conductance levels, also influenced either spike rate or spiking regularity of model VGNs. We observed that neither I-$Na_V$P nor I-$Na_V$R had any discernable effect on spike rate (Fig 11D) or CV in model sustained-B, -C, or transient VGNs (Fig 11F). The model sustained-A had two notable exceptions: Figure 11D shows how adding 10% I-$Na_V$R to increased I-$Na_V$T reduced spike rate at the highest amounts of $g_{NaT}$. This was due to burst firing behavior cause by the addition of I-$Na_V$R to the model. The model sustained-A in Figure 11F shows a different effect: in this case, where the spike rate was forced to 38 spikes/sec at low $g_{NaT}$ by increasing the amplitude of injected current, the addition of I-$Na_V$R caused a depolarization block effect, thereby increasing CV. I-$Na_V$P, again, had no noticeable effect on either spike rate or regularity in any model VGN. In all, these effects were not the anticipated increase in excitability or regularity.

***Discussion***

Here we tested the influences of different sodium current components on firing patterns and spike timing regularity in modeled VGNs. Previous work done by Hight and Kalluri (2019) showed that increased $g_{NaT}$ increased regularity in the absence of or with low levels of $g_{KLV}$ (0 – 0.55 mS/cm$^2$). Increasing $g_{NaT}$ (7, 10, 13, 16, 25, 50 mS/cm2) with no $K_{LV}$ conductance produced sustained-C to sustained-A firing patterns. With slightly increased $g_{KLV}$, the sustained-A pattern was reduced to a sustained-B and sustained-C to transient. We saw that increasing I-$Na_V$T had an impact on regularity at $g_{KLV}$ levels specified for each firing pattern: universally increasing $g_{NaT}$ increased regularity for all modeled VGN. The transient model VGN was still irregular relative to the sustained models (CV = 0.9 – 0.8). The sustained-C and sustained-B VGN, on the other hand, went from irregular (~0.8) to regular (0.3). In response to current injections, we observed that increasing $g_{NaT}$ increased spike height in all model VGNs, and spike rate in sustained-B and -C.

We note that sustained-A model was susceptible to producing burst firing patterns – never seen in VGN recordings – at very low or high levels of $g_{NaT}$. Hight and Kalluri (2019) also observed that at 13 mS/cm$^2$ ($g_{KVL}$ = 0 mS/cm$^2$), the model VGN entered depolarization block in response to 60 pA current steps, and again at 140 pA when $g_{NaT}$ = 50 mS/cm$^2$ In response to pseudo-EPSCs, we observed the sustained-A model enter a burst firing pattern reminiscent of Purkinje neuron firing (Raman and Bean, 1997) at low (13 mS/cm2) $g_{NaT}$, and with the addition of I-$Na_V$R.

In simulations, $Na_V$R and $Na_V$P currents had different effects than $Na_V$T current. While I-$Na_V$P and I-$Na_V$R did not increase regularity, they did enhance spiking excitability. We observed that the addition of I-$Na_V$R reduced the ISI between the first and second spike by reducing the refractory period during current steps in sustained-A and -B model VGN, true to the traditional

effect of resurgent currents in cortical neurons (Raman and Bean, 1997; Lewis and Raman, 2014). In sustained-A model VGNs, I-Na$_V$R also decreased voltage threshold of the AP. I-Na$_V$P had a slower effect, and was often not seen at the time windows we examined. When we examined long spike trains, we noted that I-Na$_V$P reduced spike latency towards the end of the train in sustained-A model VGN, where inactivating sodium channels have increased accumulation.

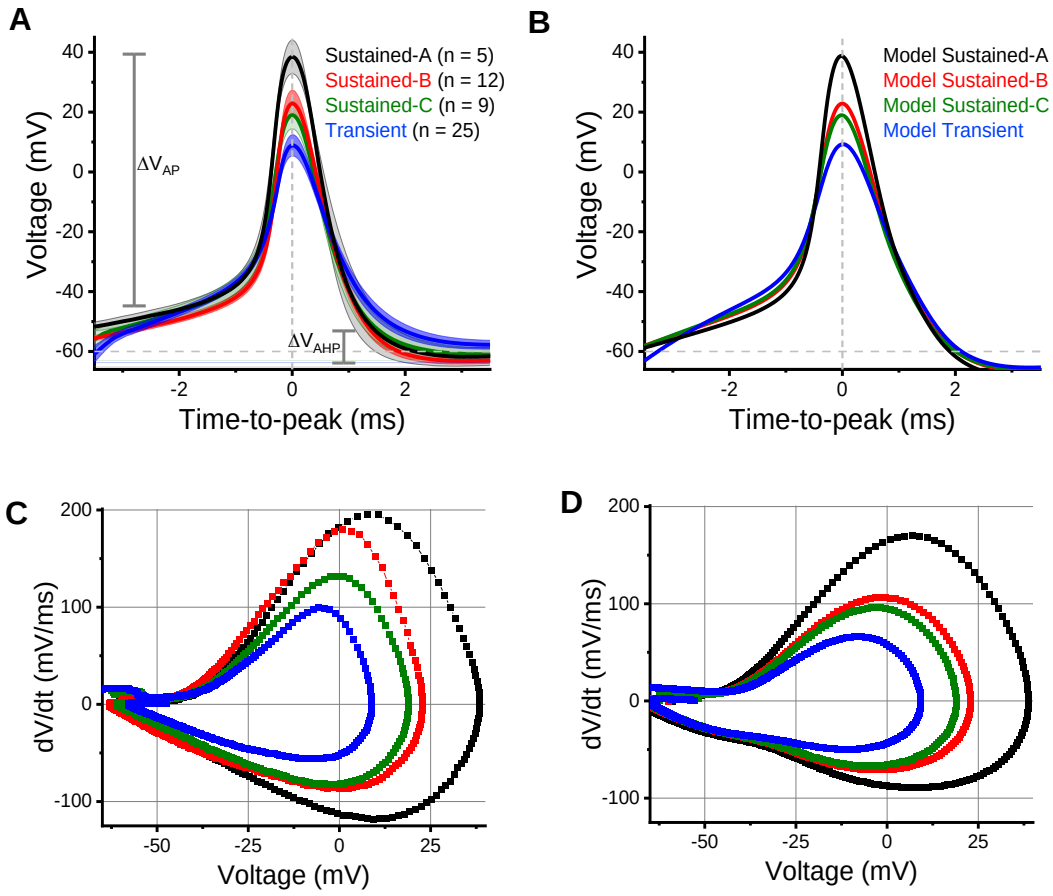


*Figure 5.7 Recorded APs served as templates for model APs.*

**A**: Population averaged recorded APs from Figure 3.1. **B:** Model generated APs based on APs from A. Comparison of phase plane plots in **C:** of APs in A and **D:** of APs in B show discrepancies in APs, particularly the peak rates of depolarization.

Although I-$Na_V$P is thought to be highly significant around resting potential (Crill 1996; Khaliq and Bean, 2010), we found no discernible effect of I-$Na_V$P on resting potential or voltage threshold. We set the amplitude of I-$Na_V$P and I-$Na_V$R using the conductance density values found in our cultured VGN recordings: these values may be an underestimation of the true size of I-$Na_V$P and I-$Na_V$R. For example, Meredith and Rennie (2020) reported peak I-$Na_V$P is 2.5% and peak I-$Na_V$R is 8% of peak I-$Na_V$T in semi-intact adult vestibular afferent endings.

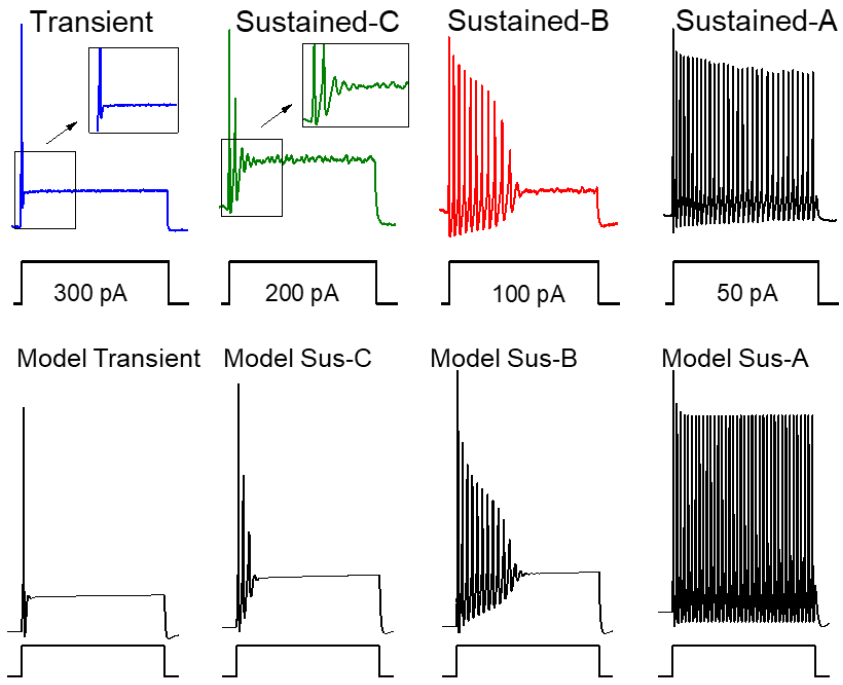


*Figure 5.8 Comparison of recorded firing patterns and generated patterns.*

**A**: Population averaged recorded APs from Figure 3.1. **B:** Model generated APs based on APs from A. Comparison of phase plane plots in **C:** of APs in A and **D:** of APs in B show discrepancies in APs, particularly the peak rates of depolarization.

***Methods***

A single compartment conductance-model was used to test the impact of I-$Na_V$T, I-$Na_V$R and I-$Na_V$P on firing patterns and spike timing regularity. The model was implemented in

*Table 5 – VGN model parameters for different firing patterns.*

Data taken from second postnatal week and older when available. Sources: [a]Hight and Kalluri (2016), [b]Kalluri et al. (2010), [c]Iwasaki et al. (2008), [d]Ventura and Kalluri (2019)

| **Firing Pattern** | $\bar{g}_{NaT,}$ (mS/cm$^2$) | $\bar{g}_{KLV}^{a,b,d}$ | $\bar{g}_{KH}^{a,c,d}$ | $\bar{g}_{H}^{d}$ | $\bar{g}_{leak}^{a,d}$ | $V_{rest}$ (mV) | $I_{inj}$ (pA) |
|---|---|---|---|---|---|---|---|
| Sustained-A | 20 | 0 | 2.8 | 0.13 | 0.03 | -60.0 | 50 |
| Sustained-B | 16 | 0.42 | 2.8 | 0.13 | 0.03 | -64.1 | 75 |
| Sustained-C | 13 | 0.55 | 2.8 | 0.13 | 0.03 | -63.5 | 80 |
| Transient | 11 | 1.1 | 2.8 | 0.13 | 0.03 | -65.7 | 120 |

MATLAB 2018b and 2021b as a differential equation in which the net current across the neuronal membrane was taken as the sum of currents flowing through individual and parallel circuit elements (Hodgkin and Huxley, 1952d):

$$I_{inj} = C_m\, S \frac{dV}{dt} + I_{Na} + I_{KLV} + I_{KH} + I_H + I_{leak} + I_{EPSC} \qquad Eq\ 6$$

This model is an extension of the single-compartment VGN model previously described by Hight and Kalluri (2016) and Ventura and Kalluri (2019). Membrane voltage *V(t)* was solved numerically using a backwards difference method. The specific membrane capacitance ($C_m$) was fixed at 0.9 μF/cm$^2$ (Gentet et al., 2000). Cell surface area (S) was fixed to yield a net capacitance of 10 pF, which a smaller value than our estimated average of 15 pF in our recorded mouse VGNs but consistent with previously published VGN models (Hight and Kalluri, 2016; Ventura and Kalluri, 2019). The 5 ionic currents represent key current types in vestibular ganglion neurons: voltage-gated sodium ($I_{Na}$), low-voltage-activated potassium ($I_{KLV}$), high-voltage-activated potassium ($I_{KH}$), hyperpolarization-activated cyclic nucleotide-gated ($I_H$), and leak ($I_{leak}$). The model VGN was stimulated by injected current steps ($I_{inj}$) while $I_{EPSC}$ was set to 0, or with trains

*Table 6 – Model parameters for $Na_V$ currents modes.*

| Model parameters for Na+ currents | | | | | |
|---|---|---|---|---|---|
| | | **Activation** | | **Inactivation** | |
| | $\bar{g}$, mS/cm$^2$ | $V_{1/2}$, mV | S, mV | $V_{1/2}$, mV | S, mV |
| $\mathbf{I_{NaT}}$ | 11 – 26 | -38 | 6 | -68 | 9 |
| $\mathbf{I_{NaP}}$ | 0.11 – 0.78 | -27 | 10 | -52 | 14 |
| $\mathbf{I_{NaR}}$ | 0.55 – 2.6 | -40 | 22 | -40 | 28 |

of simulated vestibular excitatory postsynaptic currents (pseudo-EPSCs) ($I_{EPSC}$) while $I_{inj}$ was set to 0.

To ensure that the combinations of parameters for currents reproduced APs and firing patterns of different VGNs observed *in vitro* (e.g., sustained-A vs transient firing), we fit model output using a local search optimization algorithm. This algorithm compared model APs produced by different combinations of $\bar{g}_{NaT}$, $\bar{g}_{KLV}$, and $I_{inj}$ against an averaged AP (Figs 5.7 and 5.8). For each firing pattern, the combination of parameters that produced an AP with the lowest mean squared error relative to the average AP was accepted. Other parameters were kept the constant.

In the model of Hight and Kalluri (2016), $I_{Na}$ was entirely transient (I-$Na_V$T), based on the formulation used by Rothman and Manis (2003c). We adapted $I_{Na}$ to include persistent and resurgent $Na_V$ currents by incorporating equations from Venugopal et al. (2019) for persistent and resurgent sodium current subcomponents. We modified the I-$Na_V$T equations from Hight and Kalluri (2016) and the I-$Na_V$R and I-$Na_V$P equations from Venugopal et al. (2019). Voltage-dependence and conductance density parameters for $Na_V$ currents were based on values from our mouse VGN data (Table 6).

The equation for the total sodium current was based on the computational model by Venugopal et al. (2019) and can be written as:

$$I_{Na} = I_{NaT} + I_{NaP} + I_{NaR} \quad \textit{Eq 7}$$

where $I_{NaT}$ , $I_{NaP}$, and $I_{NaR}$ are modeled as (Venugopal et al., 2019):

$$I_{NaT} = \bar{g}_{NaT}({m_T}^3 h_T)(V - E_{Na}) \quad \textit{Eq 8}$$

$$I_{NaP} = \bar{g}_{NaP}(m_{P\infty} h_P)(V - E_{Na}) \quad \textit{Eq 9}$$

$$I_{NaR} = \bar{g}_{NaR}((1 - b_R)^3 {h_R}^5)(V - E_{Na}) \quad \textit{Eq 10}$$

Conductance density ($\bar{g}$) was based on experimentally derived values from this study. The maximal persistent conductance ($\bar{g}_{NaP}$) was set to 1% of the transient conductance ($\bar{g}_{NaT}$) and the maximum resurgent conductance ($\bar{g}_{NaR}$) was set to 3% of $\bar{g}_{NaT}$, as is estimated from the cell body recordings in this study (see Table 2)

***Transient sodium current:***

The steady-state voltage-dependent activation ($m_T$) and inactivation ($h_T$) of transient sodium currents are modeled as follows, with voltage of half-activation ($V_{1/2}$) and slope factor ($k$) taken from mean values from this study (see Table 2)

$$m'_T = \frac{m_{T_\infty} - m_T}{\tau_{m_T}} \quad \textit{Eq 11}$$

$$h'_T = \frac{h_{T_\infty} - h_T}{\tau_{h_T}} \qquad \textit{Eq 12}$$

$$m_{T_\infty} = \left[1 + exp\left(\frac{-(V - V_{1/2})}{k}\right)\right]^{-1} \qquad \textit{Eq 13}$$

$$h_{T_\infty} = \left[1 + exp\left(\frac{V - V_{1/2}}{k}\right)\right]^{-1} \qquad \textit{Eq 14}$$

Steady state voltage-dependent time constants of activation and inactivation functions for transient sodium currents were taken from Rothman and Manis (2003c), following Hight and Kalluri (2016):

$$\tau_{m_T} = 10\left\{5\ exp\left[\frac{V + 60}{18}\right] + 36\ exp\left[-\frac{V + 60}{25}\right]\right\}^{-1} + 0.04 \qquad \textit{Eq 15}$$

$$\tau_{h_T} = 100\left\{7\ exp\left[\frac{V + 60}{11}\right] + 10\ exp\left[-\frac{V + 60}{25}\right]\right\}^{-1} + 0.6 \qquad \textit{Eq 16}$$

***Persistent and resurgent sodium currents***:

Equations for steady-state activation ($h_P$), inactivation ($m_P$), and steady-state voltage-dependent time constant of inactivation ($\tau_{hP}$) for persistent sodium current are based on Wu et al. (2005) and Venugopal et al. (2019) and are parameterized with our data:

$$h'_P = \frac{h_{P_\infty} - h_P}{\tau_{h_P}} \quad \textit{Eq 17}$$

$$m_{P_\infty} = \left[1 + exp\left(\frac{-(V - V_{1/2})}{k}\right)\right]^{-10} \quad \textit{Eq 18}$$

$$h_{P_\infty} = \left[1 + exp\left(\frac{V - V_{1/2}}{k}\right)\right]^{-1} \quad \textit{Eq 19}$$

$$\tau_{h_P} = 100 + \frac{10000}{1 + exp\left(\frac{V + 60}{10}\right)} \quad \textit{Eq 20}$$

The formulation for I-Na$_V$R is from Venugopal et al. (2019). It alters the Hodgkin-Huxley conductance-based formulation to incorporate state-dependent sodium resurgence (i.e., the unblocking of a channel that was blocked following a transient opening). The equations that govern voltage-dependent blocking/unblocking kinetics are as follows:

$$b'_R = \alpha_b(1 - b_R)b_{R_\infty} - k_b\beta_{b_R}b_R \quad \textit{Eq 21}$$

$$b_{R_\infty} = \left(1 + exp\left(\frac{V - V_{1/2}}{k}\right)\right)^{-1} \quad \textit{Eq 22}$$

$$\beta_{b_R} = \left(1 + exp\left(\frac{-(V-40)}{8}\right)\right)^{-2} \quad \textit{Eq 23}$$

where constants $\alpha_b$ (0.08) and $k_b$ (0.9) control the rate of unblocking. The voltage-dependent inactivation ($h_R$) functions for I-Na$_V$R include:

$$h'_R = \alpha_{h_R} h_{R_\infty} - 0.8\beta_{h_R} h_R \quad \textit{Eq 24}$$

$$h_{R_\infty} = \left(1 + exp\left(\frac{V - V_{1/2}}{k}\right)\right)^{-1} \quad \textit{Eq 25}$$

$$\alpha_{h_R} = \frac{1}{1 + exp\left(\frac{-(V+45)}{8}\right)} \quad \textit{Eq 26}$$

$$\beta_{h_R} = \frac{0.5}{1 + exp\left(\frac{-(V+45)}{15}\right)} \quad \textit{Eq 27}$$

***Synaptic conductance and EPSC shape:***

Synaptic input was generated and modeled using a formulation similar to that described in Hight and Kalluri (2016). Here we modeled EPSCs with a shape derived from EPSCs of lateral extrastriola vestibular afferent calyx in the excised P8 CD1 mouse utricular epithelium (Omar López-Ramírez, unpublished). These have longer onset and decay times relative to cochlear

EPSCs (S1) used in Hight and Kalluri (2016). An exponential function is fitted to an averaged synaptic event:

$$s(t) = 3.112 * \exp(-0.4545t) - 3.112 * \exp(-1.121t) \quad \textit{Eq 28}$$

For additional information about the model, see Hight and Kalluri (2016), Ventura and Kalluri (2019), and Venugopal et al. (2019).

## Chapter 6 – Discussion

### *$Na_V$ currents differently impact spiking excitability and spike rate timing*

Here we considered the impact of diverse sodium current modes on excitability and spike timing regularity in VGNs. We showed that VGN cell bodies can express a combination of transient ($Na_VT$), resurgent ($Na_VR$), and persistent ($Na_VP$) current components. Using computational modeling, we found that the addition of $Na_VR$ and $Na_VP$ currents increases excitability in model sustained VGNs while increasing $Na_VT$ current increases spike rate and regularity in all model VGNs.

Using isolated VGN cell bodies, we characterized different sodium currents using different voltage clamp protocols designed to evoke each component. This preparation has the advantage of accessibility to the soma due to removal of glia and myelin and control of recording conditions that cannot be manipulated in vivo. Pharmacological experiments suggest that $Na_V1.6$ channels carry a significant proportion of each current, and their block influence spiking excitability. Enhancement of $Na_V$ currents via application of ATX-II showed that increased noninactivating current increased both excitability and regularity. However, in physiological conditions needed to record spiking activity, we were unable to segregate the $Na_VT$, $Na_VP$, and $Na_VR$ current components but observed the relationship of maximum conductance to firing pattern.

With these constraints in mind, we used a conductance-based VGN model to investigate the impact of $Na_VP$ and $Na_VR$ currents on spiking excitability, spike rate, and regularity. Simulations suggest that $Na_VR$ current reduces first spike latency and ISI by increasing post-spike channel availability. $Na_VP$ current typical of our data had a minute influence, reducing spike latency to a current step by ~1 ms and increasing $Na_V$ current during APs by >0.1 pA. However,

simulations found no effect of $Na_VR$ and $Na_VP$ currents on spike regularity. $Na_VT$ currents enhanced both excitability (increasing spike rate), spike height, and regularity.

***Sodium current component diversity in vestibular ganglion neurons includes different current modes***

We recorded large $Na_VT$ currents in all VGNs. As previously shown, $Na_VT$ currents in *cultured* VGNs were entirely TTX-sensitive (Chabbert et al., 1997; Risner and Holt, 2006; Liu et al., 2016). We report that a subset of VGNs also expressed $Na_VP$ current and another subset had additional $Na_VR$ current. VGNs that expressed $Na_VR$ current components showed a more negative activation voltage range and overall greater $Na_V$ conductance density relative to VGNs with none, indicating expression of more $Na_V$ channels in a subthreshold voltage range. Applications of $Na_V1.6$ blocker 4,9-ah-TTX showed that much of the $Na_VT$ current and most of $Na_VP$ and $Na_VR$ currents are carried through $Na_V1.6$ channels. AP clamp experiments showed that during an AP, sustained VGNs had more $Na_V1.6$ current than did transient VGNs, and the $Na_V1.6$ current flowed mostly during the initial phase of depolarization.

In cultured VGNs, we found I-$Na_VR$ only after the first postnatal week (P10+). This result corroborates data from Rennie and Meredith (2020), who saw developmental upregulation of I-$Na_VR$ in vestibular afferent endings. To record from mature neurons, we used an overnight cultured preparation to reduce myelin and satellite cell coverage increases with age. However, out of approximately 150 cultured VGNs tested (P3 – 25), we found only 6 examples of I-$Na_VR$, 5 of which were older than P17. This incidence is low compared to what Meredith and Rennie (2020) observed: 67% of afferent endings expressed I-$Na_VR$ in the third postnatal week. Possible factors include species differences (mouse vs gerbil), preparation (dissociated and cultured vs semi-

intact), localization (afferent terminal vs. cell body), etc. Additionally, the overnight culturing may itself influence $Na_V$ channel expression and the resulting firing characteristics (Liu et al., 2016; Cai et al., 2017). For example, we were surprised to note there was no observable increase of $Na_V$ conductance density with age in our cultured neurons. This may be revisited in an acute preparation, like that of Liu et al., 2016. Additionally, many voltage-gated calcium currents (L-, N-, P/Q-, R-, and T-type) (Desmadryl et al. 1997; Chambard et al. 1999) have been described in immature mouse VGNs, but their contribution to AP waveform and spiking has also not been investigated.

We were unable to demonstrate the direct impact of I-$Na_V$R and I-$Na_V$P currents on firing patterns and spike regularity *in vitro*. In the physiological recording conditions needed to produce spiking in VGNs, I-$Na_V$P and I-$Na_V$R proved difficult to identify. These small amplitude currents were obscured by the large $Na_V$T, K, HCN, and leak currents present in VGN in these experiments. Additionally, the fast nature of $Na_V$ currents makes them difficult to clamp, even at room temperature.

While the molecular underpinnings of $Na_V$P currents are unknown, I-$Na_V$R is theorized to arise from the internal block of $Na_V$1.6 channels by a positively charged molecule, e.g., $Na_V$ auxiliary subunit β4 (Raman and Lewis, 2014; White et al., 2019). Previous reports of vestibular ganglia RNA indicate expression of most $Na_V$ pore-forming (α) subunits and all auxiliary (β) subunits. RT-PCR on P1 rat vestibular ganglia, comprising myelinating supporting cells as well as VGNs, revealed expression of all α subunits ($Na_V$1.1-1.9) and β subunits ($Na_V$β1-4); with only expression of the skeletal sodium channel $Na_V$1.4 dropping out by P21 (Liu et al., 2016). Different $Na_V$ alpha subunits carry currents of different voltage dependencies and tetrodotoxin (TTX)

sensitivities. With whole-cell recordings from rat VGN cell bodies acutely dissociated in the first postnatal week, we previously identified four different transient $Na_V$ currents: two TTX-sensitive currents (composed of an unknown number of possible subunits), one TTX-insensitive current ($Na_V1.5$), and one TTX-resistant current ($Na_V1.8$) (Liu et al., 2016). In the cultured mouse VGNs of this study, we found evidence of TTX-sensitive, non-$Na_V1.6$ currents. Application of 4,9-ah-TTX revealed a smaller $Na_V$ current that was significantly more negative in inactivation. The rat RT-PCR data indicate $Na_V1.1$, 1.2, 1.3, and 1.7 are all potential channel candidates.

In other neurons, persistent and resurgent currents contribute significantly to rapid spontaneous, continuous regular and/or burst firing. I-$Na_V$P typically activates at subthreshold membrane potentials when few other channels are activated and membrane resistance is high, effectively amplifying small depolarizing inputs (Llinás and Sugimori, 1980; Crill, 1996). I-$Na_V$R was originally discovered in Purkinje neurons (Raman and Bean, 1997), and is attributed to $Na_V1.6$ (Raman et al., 1997; Grieco et al., 2005). I-$Na_V$R has been described in more than 20 types of neurons that show spontaneous, repetitive, or bursting behaviors (reviewed in Lewis and Raman, 2014).

With respect to inner ear systems, persistent and resurgent sodium currents have been described in auditory (spiral) ganglion (Browne et al, 2017), avian nucleus magnocellularis neurons (Hong et al., 2018), calyx of Held (Leao et al., 2005) and its postsynaptic target, the medial nucleus of trapezoid body (Kim et al., 2010), as well as vestibular afferent calyx terminals (Meredith and Rennie, 2020) and medial vestibular nuclei neurons (Gittis and du Lac, 2008). All these examples show high spiking spontaneity and fast firing rates. Earlier VGN studies noted an association between excitability and regularity, with both thought to reflect the impact of $K_{LV}$

channel expression (lower in regular afferents). It was therefore interesting to see predicted effects of adding I-$Na_V$P and I-$Na_V$R on excitability, without concomitant effects on spike regularity.

***Differences in $Na_V$ current expression may contribute to differences in neuronal excitability***

The vestibular epithelia, where VGNs receive their synaptic input, are divided into two zones (central and peripheral) that influence spiking. Regular afferents form large dendritic arbors in peripheral zones of the sensory epithelia, where inputs from many synaptic terminals travel significant distances along thin fibers to converge and summate at the spike initiation zone. In contrast, irregular afferents make a smaller number of synaptic endings in a compact dendritic arbor in the central zone of the sensory epithelium. I-$Na_V$R and I-$Na_V$P have been recorded in vestibular calyceal afferent endings in gerbil cristae, where they appear in both central (putative transient/irregular) afferents and peripheral (sustained/regular) afferents (Meredith and Rennie, 2020).

Peripheral calyx afferent endings express more types of $Na_V$ currents relative to central afferent endings in acutely dissected gerbil cristae (Meredith and Rennie, 2018). Using TTX, multiple TTX-sensitive and insensitive currents have been observed in immature cells: TTX-insensitive $Na_V$1.5 currents were only expressed in calyces in the first postnatal week, consistent with results in immature VNGs (Liu et al. 2016). There was no observed difference between zones (Meredith and Rennie, 2018). By maturity (P30), only TTX-sensitive persistent with age. No TTX-resistant ($Na_V$1.8 or $Na_V$1.9) current was detected in either immature or mature calyces. Additionally, more 4,9-ah-TTX sensitive ($Na_V$1.6) currents were observed in mature peripheral zones calyces. $Na_V$1.6 expression increased with age in all calyces tested, as indicated by an increase in blocked current between ages P5-7 and P11-14. By maturity, $Na_V$1.6 currents make up

37% of the total sodium current in the afferents synapsing in the peripheral zone (likely regular), but less than 15% of the current in calyces from the central zone (irregular).

We saw no difference in $Na_V1.6$ currents (as measured by 4,9-ah-TTX sensitive) between sustained and transient VGNs in our cultured cell bodies. Our data suggests that cells with I-$Na_V$P and I-$Na_V$R have greater sodium conductance density, indicating a greater concentration of channels per cell. Given the peripheral localization of expression of I-$Na_V$P and I-$Na_V$R in the sensory epithelia (Meredith and Rennie 2020), and that sustained-firing VGN have larger $Na_V$ conductance, we hypothesized that regularly firing VGN are most likely to express resurgent currents but have no way to assess this.

The $Na_V1.6$ currents in calyceal afferent endings have also been determined to be composed of transient, persistent, and resurgent components (Meredith and Rennie, 2020). Both TTX- and 4,9-ah-TTX-sensitive $Na_V$P current was found in immature and mature calyces, from both the central and peripheral zones. It increased in amplitude with age, going from 0.6% to 2.5% of the peak $Na_V$T current. Time-dependent decay of $Na_V$P slowed with age, reflecting possible changes to the underlying channel subunits (Meredith and Rennie, 2020). Resurgent current also increased in frequency and amplitude with age. I-$Na_V$R was detected more frequently and with greater amplitudes in the second/third postnatal weeks, and with greater frequency in peripheral calyces, coinciding with increased expression of $Na_V1.6$ currents in the peripheral zones.

***$Na_V$ currents impact spike waveform and excitability***

Using the AP clamp method, we showed that $Na_V$ current flow is related to the initial depolarization phase of the AP in VGNs. In transient VGNs, more sodium current flowed by the time of the peak rate of depolarization relative to sustained VGN. This may reflect differences in

the underlying $Na_V$ current kinetics, where sustained VGNs may have greater slowly or non-inactivating current or differences in AP waveform. We show in Chapter 3 (Figure 3.1) that sustained VGNs have, on average, taller APs with faster rates of depolarization. A combination of factors is likely since the depolarization of the AP and the kinetics of $Na_V$ currents interdependent.

Previous work suggests that, with age, step-evoked firing patterns of isolated VGNs from rats and mice become more homogeneous, such that there are fewer fully sustained-A VGNs as $K_{LV}$ currents grow with developmental upregulation of $K_V7$ channels (Iwasaki et al., 2008; Kalluri et al., 2010; Meredith and Rennie, 2015; Ventura and Kalluri, 2019), while regularity differences become crisper. In vestibular calyx terminals in peripheral zones, there is little low-voltage-activated potassium current in the first postnatal week (Songer and Eatock, 2013) but these currents increase through the third week (Meredith and Rennie, 2015; Ramirez et al., 2018). By the third postnatal week, cultured rat VGNs are likely to exhibit sustained-B or transient firing patterns, with only a tiny percentage still showing a full sustained-A spike train (Ventura and Kalluri, 2019).

Experiments have shown that the increasing $K_{LV}$ current with development makes VGNs less excitable, with firing in response to current steps showing increased threshold current for spiking and fewer spikes upon reaching threshold. In the computational model of VGNs presented here, the amount of $K_{LV}$ current was key in determining the effect of $Na_V$ currents on firing patterns and regularity. Step-evoked firing patterns showed that transient (irregular) model VGNs, which have the highest $K_{LV}$ conductance, were unaffected by resurgent and persistent NaV currents. Larger and larger decrements in $K_{LV}$ conductance progressively changed the firing pattern from transient to sustained-C to sustained-B to sustained-A. With these changes, there was also a graded increase in the effect of $Na_VR$ and $Na_VP$ currents on firing patterns, with the greatest effect on

sustained-A model VGNs for which $Na_VR$ and $Na_VP$ currents reduced refractory periods, increased spike rate, and reduced spiking threshold during step current injections.

All model VGNs were influenced by increased I-$Na_VT$. When stimulated with current step injections, excitability increased: spike height increased, current threshold decreased, and number of spikes per current step increased. Sustained model VGNs became ever more sustained, but transient model VGNs remained transient. In response to EPSC injections, increasing I-$Na_VT$ increased spike rate in all model VGNs. Spike train regularity also increased independent of changes in firing rate, showing that, at a set $K_{LV}$ conductance, increasing $Na_V$ conductance drives changes in spike timing regularity. Even transient model VGNs increased in regularity but were less sensitive to the effects of increasing $Na_V$ conductance density, and remained irregular relative to sustained-A, -B, and -C model VGNs. This makes sense given that, in whole-cell recordings, $K_{LV}$ remains the driving factor in regularity in transient VGNs, regardless of the amount of $Na_V$ current present (Hight and Kalluri, 2016).

***Role of sodium currents in spike timing regularity***

Many factors may contribute to spike timing regularity, but ion channel mechanisms are likely to have significant influence (Eatock et al., 2008). We found great variance in the maximum $Na_V$ conductance density in VGNs. Sustained-A firing VGNs had consistently high $Na_V$ conductance density. Transient VGNs had the highest and the lowest amount of $Na_V$ conductance density. We originally expected sustained VGNs to have the highest $Na_V$ conductance densities given their large APs and fast firing rates *in vivo*. Indeed, sustained-A VGNs had the tallest APs which had the fastest rates of depolarization (peak dV/dt) on average. These two AP waveform parameters positively correlated with larger $Na_V$ conductance densities, suggesting that larger $Na_V$

currents are related to taller and quickly depolarizing APs. Transient VGNs with large $Na_V$ conductances densities also had taller APs and moderately high rates of depolarization compared to those with smaller $Na_V$ conductance densities.

In summary, we have found that $Na_V$ currents directly impact AP waveform: AP height, rate of depolarization, and afterhyperpolarization are reduced by $Na_V$ channel blockers. Spiking was likewise influenced as blocking or enhanced $Na_V$ currents altered current threshold and spike rate. Our VGN simulations produced a dissociation of $Na_V$ current effects on excitability and regularity: where large inactivating currents impact both excitability and spike timing regularity, small non-inactivating $Na_V$ currents only influenced spike excitability, as reflected in refractory periods and spike latencies. This suggests that once spiking is initiated, regularity requires the interplay of $K_{LV}$ and HCN conductances with robust $Na_V$ currents (Ventura and Kalluri, 2019), but the dominant factor producing the two regularity populations of VGNs is variation in the expression of $K_{LV}$ and HCN conductances.

## References


**Bean BP**. The action potential in mammalian central neurons. *Nature Reviews Neuroscience* 8: 451–465, 2007.

**Browne L**, **Smith KE**, **Jagger DJ**. Identification of Persistent and Resurgent Sodium Currents in Spiral Ganglion Neurons Cultured from the Mouse Cochlea. *eNeuro* ENEURO.0303-17.2017, 2017.

**Cai HQ**, **Gillespie LN**, **Wright T**, **Brown WGA**, **Minter R**, **Nayagam BA**, **O'Leary SJ**, **Needham K**. Time-dependent activity of primary auditory neurons in the presence of neurotrophins and antibiotics. *Hearing Research* 350: 122–132, 2017.

**Carter BC**, **Bean BP**. Sodium Entry during Action Potentials of Mammalian Neurons: Incomplete Inactivation and Reduced Metabolic Efficiency in Fast-Spiking Neurons. *Neuron* 64: 898–909, 2009.

**Chabbert C**, **Chambard JM**, **Sans A**, **Desmadryl G**. Three Types of Depolarization-Activated Potassium Currents in Acutely Isolated Mouse Vestibular Neurons. *Journal of Neurophysiology* 85: 1017–1026, 2001a.

**Chabbert C**, **Chambard J-M**, **Valmier J**, **Sans A**, **Desmadryl G**. Voltage-activated sodium currents in acutely isolated mouse vestibular ganglion neurones. *NeuroReport* 8: 1253, 1997.

**Chabbert C**, **Chambard J-M**, **Valmier J**, **Sans A**, **Desmadryl G**. Hyperpolarization-activated (Ih) current in mouse vestibular primary neurons. *NeuroReport* 12: 2701, 2001b.

**Chambard JM**, **Chabbert C**, **Sans A**, **Desmadryl G**. Developmental changes in low and high voltage-activated calcium currents in acutely isolated mouse vestibular neurons. *The Journal of Physiology* 518: 141–149, 1999.

**Costa PF**. The kinetic parameters of sodium currents in maturing acutely isolated rat hippocampal CA1 neurones. *Developmental Brain Research* 91: 29–40, 1996.

**Crill WE**. Persistent Sodium Current in Mammalian Central Neurons. *Annual Review of Physiology* 58: 349–362, 1996.

**Desmadryl G**, **Chambard J-M**, **Valmier J**, **Sans A**. Multiple voltage-dependent calcium currents in acutely isolated mouse vestibular neurons. *Neuroscience* 78: 511–522, 1997.

**Eatock RA**, **Songer JE**. Vestibular Hair Cells and Afferents: Two Channels for Head Motion Signals. *Annual Review of Neuroscience* 34: 501–534, 2011.

**Eatock RA**, **Xue J**, **Kalluri R**. Ion channels in mammalian vestibular afferents may set regularity of firing. *Journal of Experimental Biology* 211: 1764–1774, 2008.

**Fernandez C**, **Goldberg JM**, **Baird RA**. The vestibular nerve of the chinchilla. III. Peripheral innervation patterns in the utricular macula. *Journal of Neurophysiology* 1990.

**Gentet LJ**, **Stuart GJ**, **Clements JD**. Direct Measurement of Specific Membrane Capacitance in Neurons. *Biophysical Journal* 79: 314–320, 2000.

**Gittis AH**, **du Lac S**. Similar Properties of Transient, Persistent, and Resurgent Na Currents in GABAergic and Non-GABAergic Vestibular Nucleus Neurons. *Journal of Neurophysiology* 99: 2060–2065, 2008.

**Gittis AH**, **Moghadam SH**, **du Lac S**. Mechanisms of Sustained High Firing Rates in Two Classes of Vestibular Nucleus Neurons: Differential Contributions of Resurgent Na, Kv3, and BK Currents. *Journal of Neurophysiology* 104: 1625–1634, 2010.

**Goldberg JM**. Afferent diversity and the organization of central vestibular pathways. *Exp Brain Res* 130: 277–297, 2000.

**Goldberg JM**, **Fernandez C**. Physiology of peripheral neurons innervating semicircular canals of the squirrel monkey. I. Resting discharge and response to constant angular accelerations. *Journal of Neurophysiology* 34: 635–660, 1971.

**Grieco TM**, **Raman IM**. Production of Resurgent Current in NaV1.6-Null Purkinje Neurons by Slowing Sodium Channel Inactivation with β-Pompilidotoxin. *J Neurosci* 24: 35–42, 2004.

**Hight AE**, **Kalluri R**. A biophysical model examining the role of low-voltage-activated potassium currents in shaping the responses of vestibular ganglion neurons. *Journal of Neurophysiology* 116: 503–521, 2016.

**Hodgkin AL**, **Huxley AF**. A quantitative description of membrane current and its application to conduction and excitation in nerve. *The Journal of Physiology* 117: 500–544, 1952.

**Holmes WR**, **Huwe JA**, **Rowe MH**, **Peterson EH**. Afferent-hair cell connectivity as a possible source of spike train irregularity in turtle vestibular bouton afferents. *BMC Neuroscience* 15: P69, 2014.

**Holmes WR**, **Huwe JA**, **Williams B**, **Rowe MH**, **Peterson EH**. Models of utricular bouton afferents: role of afferent-hair cell connectivity in determining spike train regularity. *Journal of Neurophysiology* 117: 1969–1986, 2017.

**Hong H**, **Lu T**, **Wang X**, **Wang Y**, **Sanchez JT**. Resurgent sodium current promotes action potential firing in the avian auditory brainstem. *The Journal of Physiology* 596: 423–443, 2018.

**Iwasaki S**, **Chihara Y**, **Komuta Y**, **Ito K**, **Sahara Y**. Low-Voltage-Activated Potassium Channels Underlie the Regulation of Intrinsic Firing Properties of Rat Vestibular Ganglion Cells. *Journal of Neurophysiology* 100: 2192–2204, 2008.

**Jamali M**, **Chacron MJ**, **Cullen KE**. Self-motion evokes precise spike timing in the primate vestibular system. *Nature Communications* 7: 13229, 2016.

**Kalluri R**, **Xue J**, **Eatock RA**. Ion Channels Set Spike Timing Regularity of Mammalian Vestibular Afferent Neurons. *Journal of Neurophysiology* 104: 2034–2051, 2010.

**Khaliq ZM**, **Gouwens NW**, **Raman IM**. The Contribution of Resurgent Sodium Current to High-Frequency Firing in Purkinje Neurons: An Experimental and Modeling Study. *J Neurosci* 23: 4899–4912, 2003.

**Kim JH**, **Kushmerick C**, **Gersdorff H von**. Presynaptic Resurgent Na+ Currents Sculpt the Action Potential Waveform and Increase Firing Reliability at a CNS Nerve Terminal. *J Neurosci* 30: 15479–15490, 2010.

**Klinger AB, Eberhardt M, Link AS, Namer B, Kutsche LK, Schuy ET, Sittl R, Hoffmann T, Alzheimer C, Huth T, Carr RW, Lampert A.** Sea-Anemone Toxin ATX-II Elicits A-Fiber-Dependent Pain and Enhances Resurgent and Persistent Sodium Currents in Large Sensory Neurons. Mol Pain 8: 1744-8069-8–69, 2012.

**Lasker DM**, **Han GC**, **Park HJ**, **Minor LB**. Rotational Responses of Vestibular–Nerve Afferents Innervating the Semicircular Canals in the C57BL/6 Mouse. *JARO* 9: 334–348, 2008.

**Lewis AH**, **Raman IM**. Resurgent current of voltage-gated Na+ channels. *The Journal of Physiology* 592: 4825–4838, 2014.

**Li A**, **Xue J**, **Peterson EH**. Architecture of the Mouse Utricle: Macular Organization and Hair Bundle Heights. *Journal of Neurophysiology* 99: 718–733, 2008.

**Limón A**, **Pérez C**, **Vega R**, **Soto E**. Ca2+-Activated K+-Current Density Is Correlated With Soma Size in Rat Vestibular-Afferent Neurons in Culture. *Journal of Neurophysiology* 94: 3751–3761, 2005.

**Liu X-P**, **Wooltorton JRA**, **Gaboyard-Niay S**, **Yang F-C**, **Lysakowski A**, **Eatock RA**. Sodium channel diversity in the vestibular ganglion: NaV1.5, NaV1.8, and tetrodotoxin-sensitive currents. *Journal of Neurophysiology* 115: 2536–2555, 2016.

**Lysakowski A**, **Gaboyard-Niay S**, **Calin-Jageman I**, **Chatlani S**, **Price SD**, **Eatock RA**. Molecular Microdomains in a Sensory Terminal, the Vestibular Calyx Ending. *J Neurosci* 31: 10101–10114, 2011.

**Meredith FL**, **Kirk ME**, **Rennie KJ**. Kv1 channels and neural processing in vestibular calyx afferents. *Front Syst Neurosci* 9, 2015.

**Meredith FL**, **Rennie KJ**. Regional and Developmental Differences in Na+ Currents in Vestibular Primary Afferent Neurons. *Front Cell Neurosci* 12, 2018.

**Meredith FL**, **Rennie KJ**. Persistent and resurgent Na+ currents in vestibular calyx afferents. *Journal of Neurophysiology* 124: 510–524, 2020.

**Rajdl K**, **Lansky P**. Fano factor estimation. *Mathematical Biosciences & Engineering* 11: 105, 2014.

**Raman IM**, **Bean BP**. Resurgent Sodium Current and Action Potential Formation in Dissociated Cerebellar Purkinje Neurons. *J Neurosci* 17: 4517–4526, 1997.

**Risner JR**, **Holt JR**. Heterogeneous Potassium Conductances Contribute to the Diverse Firing Properties of Postnatal Mouse Vestibular Ganglion Neurons. *J Neurophysiol* 96: 2364–2376, 2006.

**Rosker C, Lohberger B, Hofer D, Steinecker B, Quasthoff S, Schreibmayer W.** The TTX metabolite 4,9-anhydro-TTX is a highly specific blocker of the Nav1.6 voltage-dependent sodium channel. American Journal of Physiology-Cell Physiology 293: C783–C789, 2007.

**Rothman JS**, **Manis PB**. The Roles Potassium Currents Play in Regulating the Electrical Activity of Ventral Cochlear Nucleus Neurons. *Journal of Neurophysiology* 89: 3097–3113, 2003.

**Sadeghi SG**, **Chacron MJ**, **Taylor MC**, **Cullen KE**. Neural Variability, Detection Thresholds, and Information Transmission in the Vestibular System. *J Neurosci* 27: 771–781, 2007.

**Songer JE**, **Eatock RA**. Tuning and Timing in Mammalian Type I Hair Cells and Calyceal Synapses. *J Neurosci* 33: 3706–3724, 2013.

**Ventura CM**, **Kalluri R**. Enhanced Activation of HCN Channels Reduces Excitability and Spike-Timing Regularity in Maturing Vestibular Afferent Neurons. *J Neurosci* 39: 2860–2876, 2019.

**Venugopal S**, **Seki S**, **Terman DH**, **Pantazis A**, **Olcese R**, **Wiedau-Pazos M**, **Chandler SH**. Resurgent Na+ Current Offers Noise Modulation in Bursting Neurons. *PLOS Computational Biology* 15: e1007154, 2019.

**White HV**, **Brown ST**, **Bozza TC**, **Raman IM**. Effects of FGF14 and NaVβ4 deletion on transient and resurgent Na current in cerebellar Purkinje neurons. *Journal of General Physiology* 151: 1300–1318, 2019

**Wu N**, **Enomoto A**, **Tanaka S**, **Hsiao C-F**, **Nykamp DQ**, **Izhikevich E**, **Chandler SH**. Persistent Sodium Currents in Mesencephalic V Neurons Participate in Burst Generation and Control of Membrane Excitability. *Journal of Neurophysiology* 93: 2710–2722, 2005.

.

## Appendix

Table 7 – Figure 2.6B statistical analysis: Voltage dependence of activation between I-$Na_V$ with different components

| One-way ANOVA | |
|---|---|
| DoF | 2, 27 |
| F | 5.95 |
| p | 0.008 |
| Statistical Significance | ** |
| Power | 0.83 |

| Tukey's HSD | Mean Diff | Prob | Summary |
|---|---|---|---|
| I-NaVT vs. I-NaVT+P | 1.93 | 0.82 | ns |
| I-NaVT vs. I-NaVT+P+R | 12.76 | 0.007 | ** |
| I-NaVT+P vs. I-NaVT+P+R | -10.82 | 0.02 | * |

Table 8 – Figure 2.6B statistical analysis: Voltage dependence of inactivation between I-$Na_V$ with different components

| One-way ANOVA | |
|---|---|
| DoF | 2, 26 |
| F | 0.38 |
| p | 0.68 |
| Statistical Significance | ns |
| Power | 0.10 |

| Tukey's HSD | Mean Diff | Prob | Summary |
|---|---|---|---|
| I-NaVT vs. I-NaVT+P | -3.69 | 0.66 | ns |
| I-NaVT vs. I-NaVT+P+R | -2.62 | 0.86 | ns |
| I-NaVT+P vs. I-NaVT+P+R | -1.06 | 0.97 | ns |

Table 9 – Figure 2.6C statistical analysis: $Na_V$ $G_{Max}$ between I-$Na_V$ with different components

| One-way ANOVA | |
|---|---|
| DoF | 2, 70 |
| F | 6.65 |
| p | 0.002 |
| Statistical Significance | ** |
| Power | 0.90 |

| Tukey's HSD | Mean Diff | Prob | Summary |
|---|---|---|---|
| I-NaVT vs. I-NaVT+P | -0.75 | 0.25 | ns |
| I-NaVT vs. I-NaVT+P+R | -3.03 | 0.002 | ** |
| I-NaVT+P vs. I-NaVT+P+R | 2.27 | 0.02 | * |

Table 10 – Figure 2.7B statistical analysis: Voltage dependence of activation between 4,9-ah-TTX sensitive and non-sensitive current

| One-way ANOVA | |
|---|---|
| DoF | 2, 14 |
| F | 1.95 |
| p | 0.176 |
| Statistical Significance | ns |
| Power | 0.34 |

| Tukey's HSD | Mean Diff | Prob | Summary |
|---|---|---|---|
| Control vs. Residual | 5.87 | 0.25 | ns |
| Control vs. Blocked | 0.35 | 0.99 | ns |
| Residual vs. Blocked | -6.21 | 0.21 | ns |

Table 11 – Figure 2.7B statistical analysis: Voltage dependence of inactivation between 4,9-ah-TTX

| One-way ANOVA | |
|---|---|
| DoF | 2, 16 |
| F | 4.4 |
| p | 0.03 |
| Statistical Significance | * |
| Power | 0.66 |

| Tukey's HSD | Mean Diff | Prob | Summary |
|---|---|---|---|
| Control vs. Residual | 13.90 | 0.06 | ns |
| Control vs. Blocked | -0.73 | 0.93 | ns |
| Residual vs. Blocked | 14.63 | 0.04 | * |

Table 12 – Figure 2.9 statistical analysis: ATX-II effects on voltage dependence of $Na_VT$ or $Na_VP$ currents

| N = 7 | Act $V_{1/2}$ (mV) | Act S | Inact $V_{1/2}$ | Inact S | G density (nS/pF) | $Na_VT$ amplitude (pA) | $Na_VP$ amplitude (pA) | $Na_VP$ peak voltage (mV) |
|---|---|---|---|---|---|---|---|---|
| Control | -37.7 ± 1.2 | 5.3 ± 0.5 | -60.0 ± 21.3 | 11.2 ± 0.8 | 2.1 ± 0.7 | 3053.3 ± 610.5 | 27.4 ± 14.4 | -38.8 ± 4.2 |
| Drug | -38.7 ± 1.3 | 5.8 ± 0.1 | -80 ± 2.9 | 16.3 ± 1.6 | 1.9 ± 0.4 | 2599.4 ± 458.9 | 163.5 ± 45.9 | -30.6 ± 2.9 |
| Significance (paired t-test) | 0.37 | 0.42 | 0.29 | 0.009 | 0.55 | 0.25 | 0.01 | 0.11 |
| Effect size (Hedges' g) | 0.17 | 0.15 | 0.36 | 0.85 | 0.05 | 0.19 | 0.93 | 0.42 |
| Power | 0.13 | 0.11 | 0.16 | 0.88 | 0.08 | 0.19 | 0.81 | 0.33 |

Table 13 – Figure 3.1A: Summary of firing pattern properties

| | $V_{rest}$ (mV) (n = ) | Current threshold (pA) | $R_{in}$ (MΩ) |
|---|---|---|---|
| Sustained-A | -60.0 ± 2.2 (6) | 133.3 ± 16.7 (3) | 1020.0 ± 247.8 (5) |
| Sustained-B | -64.1 ± 1.8 (13) | 295.5 ± 34.7 (11) | 852.2 ± 280.6 (9) |
| Sustained-C | -63.5 ± 1.3 (10) | 261.1 ± 26.1 (9) | 475.3 ± 128.8 (7) |
| Transient | -65.7 ± 0.9 (33) | 426.8 ± 33.9 (28) | 464.9 ± 73.8 (20) |

Table 14 - Figure 3.1A statistical analysis (Current threshold)

Current threshold is significantly different between firing patterns.

| One-way ANOVA | |
|---|---|
| DoF | 3, 50 |
| F | 6.11 |
| p | 0.001 |
| Statistical Significance | ** |
| Power | 0.94 |

| Tukey's HSD | Mean Diff | Prob | Summary |
|---|---|---|---|
| Sustained-B vs Sustained-A | 162.12 | 0.35 | ns |
| Sustained-C vs Sustained-A | 127.78 | 0.58 | ns |
| Sustained-C vs Sustained-B | -34.34 | 0.95 | ns |
| Transient vs Sustained-A | 29345 | 0.01 | * |
| Transient vs Sustained-B | 131.22 | 0.08 | ns |
| Transient vs Sustained-C | 165.67 | 0.02 | * |

Table 15 – Figure 3.1A statistical analysis ($V_{rest}$)

$V_{rest}$ is not significantly different between firing patterns.

| | |
|---|---|
| DoF | 3, 61 |
| F | 2.11 |
| p | 0.11 |
| Statistical Significance | ns |
| Power | 0.51 |

| | | | |
|---|---|---|---|
| Sustained-B vs Sustained-A | -4.15 | 0.40 | ns |
| Sustained-C vs Sustained-A | -3.50 | 0.58 | ns |
| Sustained-C vs Sustained-B | 0.65 | 0.99 | ns |
| Transient vs Sustained-A | -5.70 | 0.09 | ns |
| Transient vs Sustained-B | -1.54 | 0.81 | ns |
| Transient vs Sustained-C | -2.20 | 0.67 | ns |

Table 16 – Figure 3.1A statistical analysis ($R_{in}$)

$R_{in}$ is not significantly different between firing patterns.

| | |
|---|---|
| DoF | 3, 40 |
| F | 2.44 |
| p | 0.08 |
| Statistical Significance | ns |
| Power | 0.56 |

| | | | |
|---|---|---|---|
| Sustained-B vs Sustained-A | -167.8 | 0.93 | ns |
| Sustained-C vs Sustained-A | -544.7 | 0.28 | ns |
| Sustained-C vs Sustained-B | -376.9 | 0.47 | ns |
| Transient vs Sustained-A | -555.2 | 0.15 | ns |
| Transient vs Sustained-B | -387.4 | 0.25 | ns |
| Transient vs Sustained-C | -10.4 | 1.00 | ns |

Table 17 – Figure 3.1C: AP waveform of different firing patterns

| | Time-to-peak (ms) | AHP (mV) | $V_{AP}$ (mV) | Current threshold (pA) | Voltage threshold (mV) | Peak dV/dt (mV/ms) | $Na_V G_{max}$ Den (nS/pF) |
|---|---|---|---|---|---|---|---|
| Sustained-A | 4.5 ± 0.4 | 11.0 ± 2.0 | 110.0 ± 6.2 | 133.3 ± 16.7 | -41.0 ± 3.3 | 208.3 ± 52.2 | 9.6 ± 0.7 |
| Sustained-B | 4.7 ± 0.3 | 6.0 ± 0.8 | 83.5 ± 6.4 | 295.5 ± 34.7 | -44.3 ± 1.1 | 166.3 ± 34.2 | 8.0 ± 1.4 |
| Sustained-C | 4.5 ± 0.3 | 4.1 ± 0.9 | 80.0 ± 7.7 | 261.1 ± 26.1 | -44.0 ± 1.3 | 123.7 ± 28.3 | 7.0 ± 1.2 |
| Transient | 4.2 ± 0.2 | 2.9 ± 0.6 | 75.1 ± 4.0 | 426.8 ± 33.9 | -42.9 ± 1.3 | 78.6 ± 12.5 | 7.5 ± 0.9 |

Table 18 – Figure 3.1C statistical analysis ($V_{AP}$)

| **One-way ANOVA** | |
|---|---|
| DoF | 3, 58 |
| F | 4.25 |
| p | 0.009 |
| Statistical Significance | ** |
| Power | 0.83 |

| **Tukey's HSD** | **Mean Diff** | **Prob** | **Summary** |
|---|---|---|---|
| Sustained-B vs Sustained-A | -26.54 | 0.08 | ns |
| Sustained-C vs Sustained-A | -30.00 | 0.05 | ns |
| Sustained-C vs Sustained-B | -3.46 | 0.98 | ns |
| Transient vs Sustained-A | -34.93 | 0.004 | ** |
| Transient vs Sustained-B | -8.39 | 0.66 | ns |
| Transient vs Sustained-C | -4.93 | 0.92 | ns |

Table 19 – Figure 3.2C statistical analysis (peak rate of depolarization)

| **One-way ANOVA** | |
|---|---|
| DoF | 3, 55 |
| F | 4.83 |
| p | 0.005 |
| Statistical Significance | ** |
| Power | 0.88 |

| **Tukey's HSD** | **Mean Diff** | **Prob** | **Summary** |
|---|---|---|---|
| Sustained-B vs Sustained-A | -42.02 | 0.79 | ns |
| Sustained-C vs Sustained-A | -84.67 | 0.31 | ns |
| Sustained-C vs Sustained-B | -42.64 | 0.71 | ns |
| Transient vs Sustained-A | -129.69 | 0.01 | * |
| Transient vs Sustained-B | -87.66 | 0.03 | * |
| Transient vs Sustained-C | -45.02 | 0.58 | ns |

Table 20 – Figure 3.1C statistical analysis (time-to-peak)

| One-way ANOVA | |
|---|---|
| DoF | 3, 49 |
| F | 0.89 |
| p | 0.45 |
| Statistical Significance | ns |
| Power | 0.23 |

| Tukey's HSD | Mean Diff | Prob | Summary |
|---|---|---|---|
| Sustained-B vs Sustained-A | 0.22 | 0.97 | ns |
| Sustained-C vs Sustained-A | 0.05 | 0.99 | ns |
| Sustained-C vs Sustained-B | -0.17 | 0.98 | ns |
| Transient vs Sustained-A | -0.31 | 0.91 | ns |
| Transient vs Sustained-B | -0.53 | 0.42 | ns |
| Transient vs Sustained-C | -0.36 | 0.78 | ns |

Table 21 – Figure 3.1C statistical analysis (voltage threshold)

| One-way ANOVA | |
|---|---|
| DoF | 3, 49 |
| F | 0.60 |
| p | 0.61 |
| Statistical Significance | ns |
| Power | 0.16 |

| Tukey's HSD | Mean Diff | Prob | Summary |
|---|---|---|---|
| Sustained-B vs Sustained-A | -3.33 | 0.60 | ns |
| Sustained-C vs Sustained-A | -3.00 | 0.71 | ns |
| Sustained-C vs Sustained-B | 0.33 | 0.99 | ns |
| Transient vs Sustained-A | -1.91 | 0.86 | ns |
| Transient vs Sustained-B | 1.42 | 0.89 | ns |
| Transient vs Sustained-C | 1.09 | 0.96 | ns |

Table 22 – Figure 3.1C statistical analysis (AHP)

| One-way ANOVA | |
|---|---|
| DoF | 3, 43 |
| F | 11.55 |
| p | 0.00001 |
| Statistical Significance | **** |
| Power | 0.99 |

| Tukey's HSD | Mean Diff | Prob | Summary |
|---|---|---|---|
| Sustained-B vs Sustained-A | -4.98 | 0.009 | *** |
| Sustained-C vs Sustained-A | -6.88 | 0.0005 | **** |
| Sustained-C vs Sustained-B | -1.90 | 0.46 | ns |
| Transient vs Sustained-A | -8.05 | 0.000006 | ***** |
| Transient vs Sustained-B | -3.08 | 0.04 | * |
| Transient vs Sustained-C | -1.17 | 0.77 | ns |

Table 23 – Figure 3.1B statistical analysis ($Na_V$ $G_{Max}$)

| One-way ANOVA | |
|---|---|
| DoF | 3, 46 |
| F | 0.50 |
| p | 0.68 |
| Statistical Significance | ns |
| Power | 0.14 |

| Tukey's HSD | Mean Diff | Prob | Summary |
|---|---|---|---|
| Sustained-B vs Sustained-A | -1.59 | 0.89 | ns |
| Sustained-C vs Sustained-A | -2.57 | 0.69 | ns |
| Sustained-C vs Sustained-B | -0.97 | 0.96 | ns |
| Transient vs Sustained-A | -2.10 | 0.69 | ns |
| Transient vs Sustained-B | -0.50 | 0.99 | ns |
| Transient vs Sustained-C | 0.47 | 0.99 | ns |

Table 24 – Figure 3.4 statistical analysis (4,9-ah-TTX effects on $V_{rest}$)

| | [illegible] (n = 5) | [illegible] (n = 11) |
|---|---|---|
| Control | -57.6 ± 3.1 | -59.5 ± 1.4 |
| Drug | -66.8 ± 3.0 | -63.8 ± 2.7 |
| Significance (paired t-test) | 0.03 | 0.16 |
| Effect size (Hedges' g) | 0.67 | 0.39 |
| Power | 0.68 | 0.27 |

Table 25 – Figure 3.5: Summary of 4,9-ah-TTX effects on AP waveform

| | | peak (ms) | (ms) | (mV) | (mV) | threshold (mV) | (mV/ms) |
|---|---|---|---|---|---|---|---|
| Control | -58.7 ± 1.6 | 4.09 ± 0.3 | 2.9 ± 0.5 | 5.4 ± 1.0 | 73.0 ± 5.9 | -42.3 ± 2.3 | 102.0 ± 23.8 |
| Drug | -64.9 ± 2.2 | 4.8 ± 0.4 | 3.9 ± 0.6 | 6.8 ± 1.2 | 55.1 ± 6.8 | -43.3 ± 3.2 | 64.4 ± 21.1 |
| Significance (paired t-test) | p = 0.01 | p = 0.05 | p = 0.13 | p = 0.40 | p = 0.01 | p = 0.90 | p = 0.03 |
| Effect size (Hedges' g) | 0.56 | 0.42 | 0.19 | 0.10 | 0.49 | 0.05 | 0.41 |
| Power | 0.79 | 0.53 | 0.31 | 0.12 | 0.76 | 0.05 | 0.62 |

Table 26 – Figure 3.5: Summary of ATX-II effects on AP waveform

| N = 7 | $V_{rest}$ (mV) | Time-to-peak (ms) | Spike Width (ms) | AHP (mV) | $V_{AP}$ (mV) | Voltage threshold (mV) | Peak dV/dt (mV/ms) |
|---|---|---|---|---|---|---|---|
| Control | -59.2 ± 0.9 | 3.8 ± 0.3 | 1.2 ± 0.1 | 4.8 ± 0.8 | 92.7 ± 5.9 | -49.7 ± 2.1 | 228.5 ± 31.7 |
| Drug | -64.0 ± 2.2 | 5.5 ± 0.8 | 2.4 ± 0.6 | 4.1 ± 1.5 | 92.8 ± 6.3 | -52.2 ± 3.5 | 208.6 ± 55.0 |
| Significance (paired t-test) | p = 0.07 | p = 0.07 | p = 0.09 | p = 0.58 | p = 0.97 | p = 0.60 | p = 0.41 |
| Effect size (Hedges' g) | 0.83 | 0.45 | 0.35 | 0.10 | 0.01 | 0.23 | 0.14 |
| Power | 0.45 | 0.45 | 0.41 | 0.07 | 0.05 | 0.07 | 0.11 |

Table 27 – Figure 4.4A statistical analysis: $Na_V1.6$ and non-$Na_V1.6$ current densities during AP Clamp

| **One-way ANOVA** | |
|---|---|
| DoF | 2, 23 |
| F | 6.32 |
| p | 0.007 |
| Statistical Significance | ** |
| Power | 0.85 |

| **Tukey's HSD** | **Mean Diff** | **Prob** | **Summary** |
|---|---|---|---|
| Control vs. Residual | 0.14 | 0.02 | * |
| Control vs. Blocked | -0.02 | 0.94 | ns |
| Residual vs. Blocked | -0.16 | 0.01 | * |

Table 28 – Figure 4.4B statistical analysis: $Na_V1.6$ and non-$Na_V1.6$ current percent flow before peak during AP Clamp

| DoF | 2, 23 |
|---|---|
| F | 3.90 |
| p | 0.04 |
| Statistical Significance | * |
| Power | 0.64 |

| | | | |
|---|---|---|---|
| Control vs. Residual | 9.65 | 0.20 | ns |
| Control vs. Blocked | -5.34 | 0.59 | ns |
| Residual vs. Blocked | -14.99 | 0.03 | * |

Table 29 – Figure 4.5: Interaction between $Na_V1.6$ and non-$Na_V1.6$ currents and firing patterns

| **Two-way ANOVA** | **Current** | **Firing Pattern** | **Interaction** |
|---|---|---|---|
| DoF | 1 | 1 | 1 |
| F | 26.9 | 0.00003 | 0.41 |
| p | 0.0002 | 0.99 | 0.53 |
| Statistical Significance | *** | ns | ns |
| Power | 0.99 | 0.05 | 0.14 |

| **Tukey's HSD** Current | Firing Pattern | Current | Firing Pattern | **Mean Diff** | **Prob** | **Summary** |
|---|---|---|---|---|---|---|
| NaV.16 | Transient | NaV.16 | Sustained | --0.08 | 0.96 | ns |
| Resident | Sustained | NaV.16 | Sustained | -0.76 | 0.01 | * |
| Resident | Sustained | NaV.16 | Transient | -0.68 | 0.01 | * |
| Resident | Transient | NaV.16 | Sustained | -0.68 | 0.01 | * |
| Resident | Transient | NaV.16 | Transient | -0.59 | 0.01 | * |
| Resident | Transient | Resident | Sustained | 0.08 | 0.97 | ns |